Visualization of Oscillatory Electron Dynamics on the Surface of Liquid Helium

Hala Siddiq

Thesis submitted for the degree of

Doctor of Philosophy

Department of Physics
Lancaster University
Lancaster, UK

February 2023

Acknowledgements

First and foremost I would like to offer my sincerest gratitude to my supervisor, Prof. Aneta Stefanovska, who introduced me to work in such an interesting field, and with a pioneer in that field, and second for her support and guidance during the last five years, which has allowed me to grow not only as a researcher, but also as a person. I am very grateful for her unreserved support throughout my thesis, guiding me with her knowledge, experience and enthusiasm. Thanks to Prof. Kimitoshi Kono for his help and the interesting discussion about some results in this work. In addition, thanks go to Kostyantyn Nasyedkin who provided me with the data, and discussed with me part of the analysed results.

I wish to sincerely thank Prof. Peter V. E. McClintock for his support, guidance and will to share his great experience and wisdom and being willing to help throughout. I appreciate greatly the valuable discussion with Prof. Yuri A. Pashkin and Dr. Dmitry Zmeev regarding the study of electron on the surface of liquid helium systems and also many thanks for their help and unwavering support throughout my PhD.

I would like to thank Dr Lawrence Sheppard who provided me with Matlab code of harmonics finder and discussed with me the results obtained from my study. Thanks go to Dr. Gemma Lancaster, Dr. Julian Newman, Dr. Phil Clempson, Dr. Tomislav Stankovski and Dr. Yevhen Suprunenko for answering programming and analysis questions, mostly in the early days of my studies. Thanks also to Dr. Paul Wileman and Sasha Proctor, for their initial work on analysing the data and support in comprehending the experimental conditions.

A special gratitude for the scientific assistance and kind friendship goes to Dr. Saleh Altarifi for his encouragement, unconditional support and discussions during my PhD journey.

Last, but by no means least, I wish also to express my gratitude for scientific assistance Dr. Abdualziz Salm for his unreserved and unconditional support, understanding and encouragement that helped me to get through over the difficult time.

I would also like to thank everybody that has made the department a serene atmosphere throughout the years, especially my co-researchers in the office: Dr. Joe Adams, Juliane Bjerkan, Mansour Alanazi, Dr. Mahmoud Eissa, Sultan Alatawi, Samuel Barnes and Dr. Yunus Abdulhameed.

I would like to extend my thanks to my family, who have been supportive and encouraging throughout my journey, with a special appreciation to my father, brothers, and sisters. I am also grateful to my sister Hind, who provided invaluable assistance when I needed it the most. Lastly, I would like to express my gratitude to Jazan University for funding my doctoral research.

To my beloved mother, who passed away but will always remain in my heart. Thank you for your unconditional love, unwavering support, and endless encouragement. You were my rock, my inspiration, and my best friend. Your wisdom, kindness, and humor will never be forgotten and will continue to guide me on my journey. I miss you every day, but I take comfort in knowing that your love and spirit live on in me. This thesis is dedicated to you with love and gratitude, forever.

Declaration

This thesis is my original work and has not been submitted, in whole or in part,for a degree at this or any other university. Nor does it contain, to the best of my knowledge and belief, any material published or written by another person, except as acknowledged in the text.

Ethics Declaration

The data recorded and analysed within this work were collected in accordance with the appropriate permissions from their respective institutions or committees, as detailed below.

- The experimental data were obtained by the Quantum Condensed Phases Research Team, RIKEN CEMS, Japan.

List of publications

Parts of the work presented in this thesis have been accepted in the following paper:

- Hala Siddiq, Kostyantyn Nasyedkin, Kimitoshi Kono, Dmitry E. Zmeev, Peter McClintock, Yuri A. Pashkin & A. Stefanovska. Visualization of Oscillatory Electron Dynamics on the Surface of Liquid Helium, accepted in *Phys Rev B* (work from chapter 5).

Parts of the work have also been presented at the following scientific meetings or workshops:

- Hala Siddiq & A. Stefanovska. Theory of the photo-excited 2-D electron gas on superfluid helium: an experimental model of chronotaxic dynamics. *Physics of Biological Oscillators, Workshop. 27–30 November 2018. Chicheley Hall, Buckinghamshire, UK.* Poster presentation.

- Hala Siddiq, Kostyantyn Nasyedkin, Paul Wileman, Kimitoshi Kono, Yuri Pashkin, Peter McClintock, Dmitry Zmeev,& A. Stefanovska. Visualization of the electric current oscillations on the surface of liquid helium. *Electrons and Ions in/on Helium (EIH-2020), which was organized by the Centre for Nano Science and Engineering (CeNSE), Indian Institute of Science (IISc) Bangalore on 23–25 January, 2020.* Poster presentation.

- Hala Siddiq, Kostyantyn Nasyedkin, Kimitoshi Kono, Yuri Pashkin, Peter McClintock, Dmitry Zmeev,& A. Stefanovska. Reconstruction of the electron oscillations on the surface of liquid helium. *QFS conference 2021, which was organized by the Centre for Nano Science and Engineering (CeNSE), Indian Institute of Science (IISc) Bangalore on 10–19 August, 2021.* Oral presentation.

- Hala Siddiq, Kostyantyn Nasyedkin, Kimitoshi Kono, Yuri Pashkin, Peter McClintock, Dmitry Zmeev,& A. Stefanovska. Reconstruction of the electron

oscillations on the surface of liquid helium. *Frontiers of Quantum and Mesoscopic Thermodynamics 2021 (FQMT'21) on 18–23 July, 2021.* Poster presentation.

Glossary and abbreviations

AAFT Amplitude-adjusted Fourier transform. A method used for building surrogates of a time series.

BDW Boundary displacement waves.

CPP Cyclic phase permutation. A method used for generating surrogates of a signal when using dynamical Bayesian inference.

DBI Dynamical Bayesian Inference. A method used to determine whether a pair of oscillators within a system are coupled, and if so, how they are coupled.

DFA Detrended fluctuation analysis. A method to determine the statistical self-similarity of a signal at different timescales.

DFT Discrete Fourier transform.

EMP Edge magnetoplasmons. It is a collective charge oscillation which occurs in 2DES subjected to a perpendicular magnetic field.

FFT Fast Fourier transform. A fast algorithm for the computation of the Fourier transform, which transforms a signal from the time domain to the frequency domain.

IAAFT Iterative amplitude - adjusted Fourier transform. A method used for generating surrogates of a signal.

IEMP Inter-edge magnetoplasmons.

MICO MW-induced conductivity oscillations induced by inter-subband MW excitation.

MIRO MW-induced resistance oscillations.

MW Microwave.

NMD Nonlinear mode decomposition. A method for the extraction of oscillatory modes from time series using time-frequency representations and surrogate methods.

PFA Phase fluctuation analysis. Method of identifying chronotaxicity from a single time series.

PSD Power spectral density. A method used to describe the distribution of power into frequency components composing that signal.

SD Standard deviation.

SE Surface electron.

SSEs Surface state electrons.

TAWP Time-averaged wavelet power.

2DEG A two-dimensional electron gas.

TFR Time-frequency representation. It is a view of a signal (taken to be a function of time) represented over both time and frequency.

WFT Windowed Fourier transform. Time-frequency representation.

WT Wavelet transform. Time-frequency representation.

ZRS Zero - resistance-states.

Notation

B magnetic field in Tesla, T
C electrical capacitance in Farad, F
E electric field in Volts per Centimeter V/cm
I electrical current in Ampere, A
n_e electron density, cm^{-2}
Q electric charge in Coulomb, C
T temperature in Kelvin, K
V pressing voltage in Volts, V

Abstract

We investigate time traces of the currents generated by the motion of electrons on the surface of liquid helium that are placed in a perpendicular magnetic field and exposed to microwave radiation. Nonlinear dynamics methods are utilized to explore the characteristic features of the current oscillations from five electrodes at different electron densities and pressing voltages. The wavelet phase coherence and phase shift are calculated to obtain the coherence relationships between the currents in the five electrodes, and the direction of motion of electrons inside the cell, as functions of the pressing voltage. These classical methods reveal that the electron motion is oscillatory with varying frequency and with a constant frequency modulation. Higher harmonics due to nonlinearity arise at higher frequencies where the the resonance condition for inter-subband transition is satisfied at a pressing voltage of 4.20 V for low electron density. Our approach provides a platform for investigating these phenomena analytically. We show that slow helium gravity waves modulate the electronic oscillatory behaviour and illustrate that the model in fact produces 3D dynamics. Motion of electrons on the surface of liquid helium is shown to be a paradigmatic example of a chronotaxic system, i.e. a system that undergoes continuous perturbation and is nonetheless capable of maintaining its stability.

Contents

List of Figures

List of Tables

1. Introduction and motivation

At low temperatures, superfluid ^{4}He provides an extraordinarily clean and pristine surface that is devoid of the defects and imperfections that are universal in other material systems. Electrons above the liquid surface provide a unique example of a two-dimensional electron gas (2DEG), trapped at the interface between the superfluid and vacuum [3, 12]. An electron naturally levitates several nanometers above the liquid surface on account of a competition between the attractive force between the electron and its induced image charge, and a repulsive barrier caused by the helium surface.

Electrons traveling along the surface collide occasionally with residual ^{4}He gas atoms and surface wave quanta (ripplons). The ^{4}He gas atom density decreases rapidly with decreasing temperature, until the electrons are scattered only by ripplons on the surface. Due to the weak coupling between the electrons and ripplons, the electron mobility becomes very high at low temperatures ($T < 1\,\mathrm{K}$) [13]. The system facilitates the exploration of 2D non-equilibrium phenomena [3], complementary to e.g. the 2DEGs in GaAs heterostructures [14].

Following the prediction [15] and observation [16] of electrons on helium, research highlights have included magnetoplasmons in classical [17, 18] and quantum regimes [19] the ripplonic Lamb shift [20], coupling of Rydberg states to Landau levels [21], quantum information processing [22, 23, 24], incompressible electronic behaviour[8, 25, 26], zero-resistance states [27, 28], and a plethora of important results on many-electron phenomena and non-equilibrium physics [26, 27, 29, 30, 31]. Electrons on liquid helium have properties that make them good candidates for qubits, with high

mobility and long decoherence time [32, 33]. While challenging, using the ground and first excited energy levels of these electrons as the basis states for qubits was proposed [22].

In addition to this, the positions of the electrons can be finely controlled by applied electric and magnetic fields. Studies of the oscillatory behavior of the currents induced by this 2D gas in the regime of strong quantizing magnetic field and vanishing diagonal conductivity [8, 25], have revealed a non-equilibrium displacement of charge density and the existence of current oscillations due to resonant microwave irradiation. In earlier experiments conducted with a circular pool of surface electrons, currents induced at the center of a Corbino electrode geometry above the liquid exhibited nonlinear oscillations in the audiofrequency range. These were attributed to edge magnetoplasmons [12, 26, 34, 35], but there was also evidence [9, 7] of an even lower-frequency modulation.

Recently, a new method for the control and read-out of electronic states, has been proposed which can detect the transitions between different Rydberg states of the electrons, called image-charge detection [36]. For example, a nearby capacitor can be used to detect small changes in the induced charge. Thus this framework is again opening a new pathway to a promising field of research for an electrons-on-helium quantum computer. In addition to this, the system of electron on helium is low-dimensional, meaning the electrons move in 2D to a good approximation, confined to a small area, with a high density of states, making it ideal for implementing quantum algorithms.

The strong interaction between electrons leads to the formation of correlated states, which is crucial for quantum computing [37]. As the electrons maintain their quantum states for long periods due to their high coherence, and their electronic properties can be easily tuned by variation of the applied voltage and microwave radiation, the system allows for the selective control and manipulation of the electrons [20, 38, 39]. These unique characteristics make the electrons-on-helium system between two parallel electrodes a promising platform for quantum computing.

Under certain conditions, the surface electrons exhibit *s*pontaneous oscillations. We investigate the time traces of currents induced in 5 segmented electrodes by the motion of electrons on the surface of liquid ^{4}He at $\sim$0.3 K, that are placed in a perpendicular magnetic field and exposed to microwave radiation.

As we demonstrate below, analysis using multi-scale, time-resolved, methods yields results consistent with magnetoplasmons modulated by slow surface gravity waves, with the latter requiring consideration of the 3rd dimension. Calculation of phase differences and phase coherence between signals from differently-positioned pairs of electrodes enables reconstruction of the electron dynamics on the helium surface.

So far, chronotaxic dynamics has been observed mainly in living systems that exhibit oscillatory dynamics on many time scales and size scales – from the cellular level [10, 40, 41], up to system, diurnal, and population levels – allowing only very limited possibilities for studying experimentally the effect of changing relevant parameter values. In contrast to these biological observational studies, the superfluid helium experiments offer us an opportunity to gain an understanding of chronotaxic behavior based on well-controlled laboratory investigations that promise to reveal fully the relationship between the physical world and the fundamental nature of chronotaxic dynamics. Such studies would be among the first to establish the characteristics of an experimentally-designed, open, non-autonomous system enabling the links between the microscopic behavior of its elements and their collective, macroscopic, behavior to be established directly. It is possible to use chronotaxicity observed for an electron-on-helium system as an experimental model to study similar phenomena observed in biological systems. The relative simplicity of the former system, in comparison to the latter, allows for greater control over the conditions and the ability to study specific aspects of the system in isolation.

For example, the ability to measure the response of the electrons to changes in the microwave and magnetic fields, as well as the pressing voltage, as a function of time can be used as a model for studying the response of biological systems to

external stimuli. Similarly, the ability to measure the distribution of electrons on the helium surface as a function of time can be used as a model for studying the temporal dynamics of biological systems.

The stability of the electron-on-helium system has a significant impact on the field of quantum computing, as it offers a well-controlled and predictable environment for quantum information processing. Despite fluctuations in microwave, pressing voltage, and electron density, the system remains stable, making it an ideal platform for quantum computing applications [39, 42].

In this thesis, we present a new study with longer recordings than in the earlier work [6, 7, 27, 34] of the electric currents induced in five Corbino electrodes above the liquid by the motion of electrons on the surface, under a strong magnetic field and microwave irradiation. Measurements were made with different electron densities and pressing voltages. Time-resolved multi-scale analysis methods were applied for the first time in this field to reconstruct the electrons' underlying oscillatory dynamics from the recorded signals. In particular, we investigate their nonlinear, non-autonomous dynamics [9, 43, 44], and study *interactions* including phase coherence [45] and couplings [46].

1.1 Aims and objectives of the work

Our study is the first to use segmented electrodes to pick up signals generated by electrons moving below them on the helium surface. Our overarching objective is to visualize this motion of electrons inside the experimental cell and to identify the type of motion. The aims are –

1. Visualize electron motion inside the experimental cell and to identify the type of motion.

2. Explain the relationship between the microscopic and collective macroscopic dynamics.

3. investigate whether the currents exhibit the properties of chronotaxic systems, and if so, under which conditions.

To achieve these aims–

1. By using multi-scale, time-resolved, methods, to analyse the currents recorded at different electron densities and pressing voltages at a fixed helium depth, in order to provide a coherent picture of how these parameters influence the nonlinear dynamics captured in the measured currents.

2. By using two distinct inverse approach methods, namely phase fluctuation analysis (PFA) and dynamical Bayesian inference, to detect chronotaxicity in the system.

These aims and objectives are addressed by tackling the following main questions–

1. What is the nature of the electron motion?

2. Do the electrons interact with the surface of the liquid helium?

3. How do the electron density and pressing voltage affect the electron motion?

4. What are the characteristic frequencies in the measured currents, and which are the relevant modes?

5. Is there coherence between the currents measured in different parts of the cylindrical cell and, if so, how do the pressing voltage and electron density influence it?

6. Is there coupling (a dynamical causal relationship) between oscillations present in the currents recorded in different parts of the cell?

7. Is the system chronotaxic?

1.2 Outline of thesis

As discussed above, the main goal of this thesis is visualizing/reconstructing the oscillatory dynamics of electrons on the surface of liquid helium for different electron densities and pressing voltages.

Chapter 2 presents background information about the system of electrons above the surface of liquid helium. Then, we present experimental investigations of MW-induced conductivity oscillations (MICO) induced by inter-subband MW excitation revealing a number of new phenomena. This chapter also describes investigation of how the edge influences transport properties in the two dimensional electron system. It also offers an explanation of the novel observations based on the Coulombic effect on the stability range of the photoexcited electron gas, which favors the formation of domains of different densities.

Chapter 3 provides details of the experimental setup. We show a schematic of the experimental arrangement used for investigating the electron gas on the surface of superfluid helium. Then, we show some of the test measurements carried out before measuring the data.

Chapter 4 introduces the inverse approach techniques used to extract the results presented in this thesis, and provides a brief review of the inverse approach as applied to the newly-defined class of chronotaxic systems.

Chapter 5 presents an analysis of the data and the results obtained.

Chapter 6 discusses the results presented in chapter 5.

Chapter 7 summarises the work presented in the thesis and outlines possible directions for future research.

Detailed information about the results of systematic analysis is provided in the supplementary material, which is available in PURE, together with the measured data used in the analysis.

2. Background

2.1 Electrons on superfluid helium

The electrons are held on the surface of liquid helium ^{4}He by a comparatively weak mirror potential which is created by the weak polarization of helium atoms in the liquid phase as presented in Fig. 2.1. The attractive force potential when z $>$ 0 is given by [3]

$$V_{\rm im}(z) = -\frac{\Lambda e^2}{z + z_0} \approx -\frac{\Lambda e^2}{z} \tag{2.1}$$

where z is the direction normal to the surface, and z_0 defines as an substitute parameter to avoid the singularity at the interface of the helium with a typical value of $z_0 \simeq 1$Å. The image potential is very weak because $\Lambda = (\epsilon_{He} - 1)/4(\epsilon_{He} + 1) \approx 0.01$, where the dielectric constant of liquid helium ^{4}He $\epsilon_{He} \approx 1.057$, and e is the elementary charge. The electrons' z-motion is quantized due to a very high repulsive barrier of $V_b = 1\,$eV appearing at the interface for ^{4}He [47, 48]. The surface of helium has this potential barrier that prevents the electron from penetrating into the liquid helium. Where z_0 is quite smaller than average distance $\langle z \rangle$ of the electrons from the surface of the liquid helium and the barrier energy mainly can exceed the attractive binding energy ($<$1 meV), the total potential energy $V_{\rm e}$ can be given as follows

$$V_{\rm e}(z) = -\frac{\Lambda e^2}{z} \quad (z > 0) \quad \text{or} \quad +\infty \quad (z \leq 0). \tag{2.2}$$

At low temperature, the electrons are confined in a potential well created by V_e

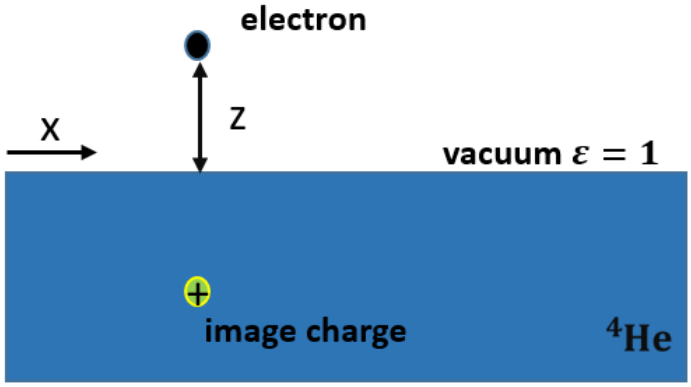

Figure 2.1: Electron on the surface of the liquid helium ^{4}He along with an image charge below the surface of helium. The helium surface can support thermally excited quantized capillary waves (ripplons) that weakly interact with the electron.

with quantized motion normal to the surface of liquid helium as shown in Fig. 2.2. The electrons can be considered as free particles with parallel motion to the surface.

2.1.1 Rydberg surface state

The three-dimensional Schrödinger equation for an electron on the surface of liquid helium is given by

$$\left[\frac{-\hbar^2}{2m}\left(\frac{\partial^2}{\partial x^2}+\frac{\partial^2}{\partial y^2}+\frac{\partial^2}{\partial z^2}\right)-\frac{\Lambda e^2}{4\pi\varepsilon_0 z}\right]\Psi(\vec{r},z)=E\Psi(\vec{r},z) \tag{2.3}$$

Eq. 2.3 can be separated into a plane wave describing in-plane motion and one-dimensional wave function χ_{n} for the vertical motion:

$$\Psi_{\mathrm{n}}(\vec{r},z)=\frac{1}{\sqrt{S_{\mathrm{A}}}}e^{i\vec{k}\cdot\vec{r}}\chi_{\mathrm{n}}(z) \tag{2.4}$$

here $\vec{k}$ defines the two-dimensional in-plane wave vector, $\vec{r}$ presents the position vector in the plane, n is the quantum number representing vertical motion of the electron, and S_{A} is s is the surface area under consideration.

With assuming flat liquid helium surface, then the motion of electron on the

surface perpendicular to the liquid helium likes a one-dimensional (1D) hydrogen atom with a reduced nuclear charge Λe. The energy $E_{\rm n}$ of the vertical motional eigenstate is presented by [49]

$$E_{\rm n} = -\frac{\Lambda^2 m_{\rm e} e^4}{2\hbar^2 n^2} = -\frac{R_y^*}{n^2}, \quad n = 1, 2, \ldots \tag{2.5}$$

where R_y^* is the effective Rydberg energy and $m_{\rm e}$ is electron mass. For liquid ^{4}He, R_y^* is roughly calculated to be $\sim 0.658\,\text{meV}$ from $\epsilon_{He} = 1.05723$ and $\Lambda \simeq 6.95 \times 10^{-3}$. The vertical wave function $\chi_{\rm n}(z) = \langle z \mid n \rangle$ in position basis is described by the solving a one-dimensional (1D) Schrödinger equation:

$$\left[-\frac{\hbar^2}{2m_{\rm e}}\frac{\partial^2}{\partial z^2} - \frac{\Lambda e^2}{z}\right]\chi_{\rm n} = E_{\rm n}\chi_{\rm n} \tag{2.6}$$

The wave functions of two lowest states $\chi_1(z)$ and $\chi_2(z)$ are

$$\begin{aligned} \chi_1(z) &= \frac{2}{a^{3/2}} z e^{-z/a} \\ \chi_2(z) &= \frac{1}{\sqrt{2}a^{3/2}} z(1 - z/2a) e^{-z/2a}, \end{aligned} \tag{2.7}$$

where a is an effective Bohr radius of the electron state given by

$$a = \frac{1}{\Lambda}\frac{\hbar^2}{m_{\rm e} e^2} = \frac{a_0}{\Lambda} \tag{2.8}$$

with $a_0 = \hbar^2/m_{\rm e}e^2 \simeq 0.53\,\text{Å}$. The effective Bohr radius is about $76\,\text{Å}$ for liquid ^{4}He. Fig. 2.2 shows the lowest energy levels $E_{\rm n}$ and the probability, of vertical motional wave function $|\chi_{\rm n}|^2$ alongside the potential energy $V_{\rm e}$. The average distance of the electron from the surface of helium $\langle z \rangle \sim a_0 \simeq 76\,\text{Å}$, is much larger than typical atomic scales $r_0 \sim 2a_0 \simeq 1\,\text{Å}$, that results to insignificant scattering from the corrugation of the surface because of individual atoms. Consequently, electrons can be stayed relatively far away from the surface of helium, and they can move like free particles. The average distances from the surface for the ground, first excited state are defined by [50],

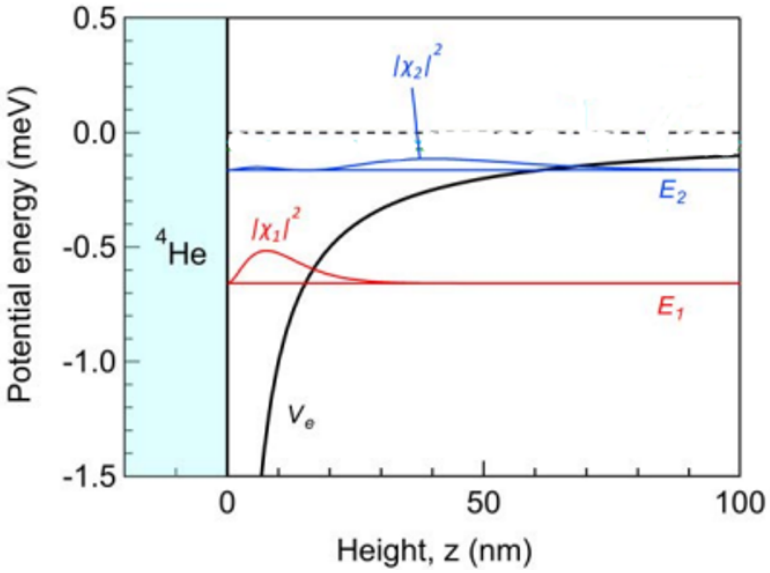

Figure 2.2: Energy spectrum and the probability for wave functions of an electron hold on the helium surface, Figure taken from Ref. [1].

$$\langle 1|z|1\rangle \simeq 114\,\text{Å}, \quad \langle 2|z|2\rangle \simeq 456\,\text{Å}. \tag{2.9}$$

The energy of the ground state is $E_1 = $ - 0.66 meV (-7.63 K) and for the energy of the first excited are $E_2 = $ - 0.16 meV (-1.91 K), which significantly exceeds atomic length scales. Therefore, the energy wanted for a transition of the electron from the ground state to the first excited state is $E_2 - E_1 = 5.72\,\text{K}$. This temperature is larger than the working T of our experiments $T \sim 0.3\,\text{K}$. This means that the electrons are effectively frozen into the lowest Rydberg energy level E_1. The transition frequencies are defined by a Balmer series these states

$$\omega_{nn'}/2\pi = \frac{E_\text{n} - E_\text{n'}}{h} = \frac{R_y^x}{h}\left|\frac{1}{n^2} - \frac{1}{n'^2}\right|. \tag{2.10}$$

This gives $\omega_{12}/2\pi \simeq 119.16\,\text{GHz}$, that is in good agreement with spectroscopic measurement data $\omega_{12}/2\pi \simeq 125.9 \pm 0.2\,\text{GHz}$ [2]. This estimation was taken based on the infinite potential barrier approximation at $z = 0$ as presented in Eq. 2.2. Indeed, a finite amount of energy exists at the surface of the potential barrier $V_\text{b} \sim 1\text{eV}$ and a non-flat helium layer can cause a small disturbance in its position. This causes a deviation between the energy levels of the experiment and

the theory [51].

2.1.2 Stark shift and external fields

An external electric field $E_\perp$ in most experiments, is applied to the electron layer to modify the potential V_e asymptotic form:

$$V_e = V_{im} + V_b + eE_\perp z. \tag{2.11}$$

All the parameters described in the previous section. Fig. 2.3, with electric field $E_\perp > 0$, can generate a linearly increasing potential V_e for large z resulting to stable bound state of electrons via pushing the electrons into the surface. With a negative pressing electric field $E_\perp < 0$, the potential approaches a triangular shape with with increasing z, leading excited surface state electrons to escape the surface by tunneling through the ionization barrier.

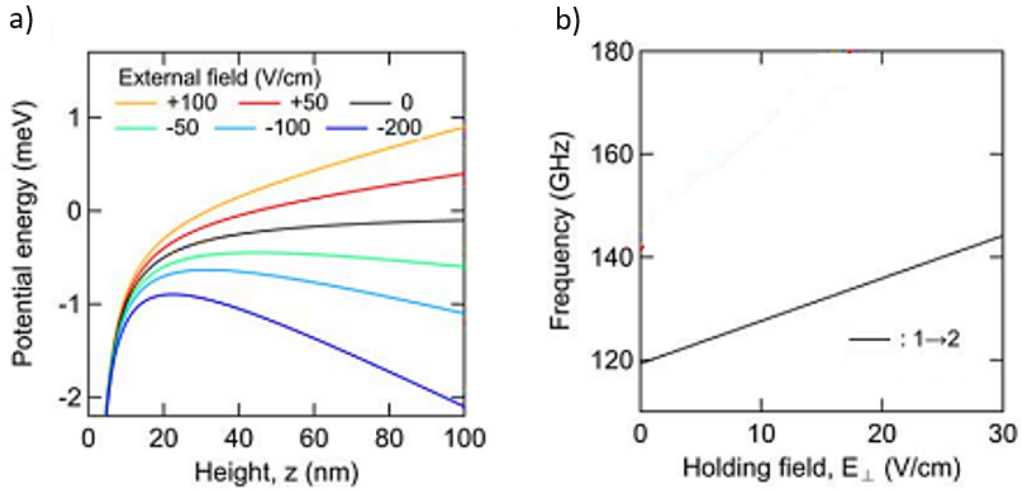

Figure 2.3: (a) Potential energy V_e alters with varying external fields. (b) Linearly Starkshifted transition frequency for $1 \rightarrow 2$ Rydberg transitions, Figures taken from Ref. [1].

The ground level wave function can be determined through a variational approach utilizing wave:

$$\chi_1(z) = \frac{2}{b^{3/2}} z e^{-z/b}. \tag{2.12}$$

The wave can have the same form as the wave function of the ground state with

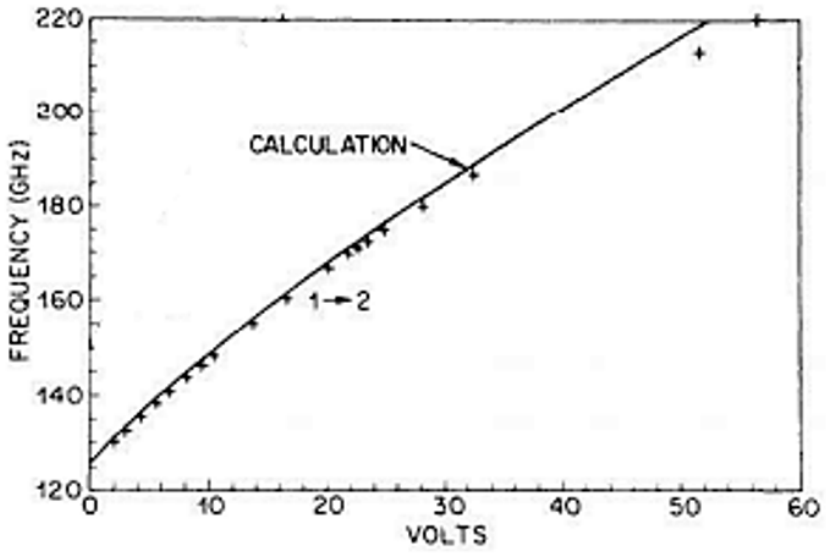

Figure 2.4: The Stark-shifted transition frequencies for vertical motional states versus voltage across the experimental cell, as first measured is obtained by Grimes et al [2]. The pressing voltage between the top and bottom electrodes inside the cell is changed by a triangular wave form applied in a way that keeps the helium surface at the same positive potential. This process allows for varying the pressing field acting on the electrons without changing the number of electrons. The crosses are spectroscopically measured data points and solid curves are the result of variational calculations, Figure taken from Ref. [3].

zero electric field. The relationship between $b\,(E_\perp)$ and the effective Bohr radius$a$ is defined by [52].

$$\frac{b}{a} = \frac{4}{3\lambda}\sinh\left(\frac{1}{3}\operatorname{arcsinh}\left(\frac{9\lambda}{4}\right)\right) \tag{2.13}$$

where $\lambda = \sqrt{E_\perp/E_\mathrm{c}}$ and the characteristic field presents as $E_\mathrm{c} = \hbar^2/2m_\mathrm{e}ea^3$. A parameter λ that provides the strength of the pressing field compared to $E_\mathrm{c} \simeq 0.9\,\mathrm{kV/cm}$. For weak value of the pressing fields, the energy state can be determined by using perturbation theory. This can give a correction which leads to equivalent results to the linear Stark shift:

$$\Delta E_\mathrm{n}^(1) = eE_\perp\langle n|z|n\rangle. \tag{2.14}$$

Indeed, the linear Stark shift has been noted in the measurement of spectroscopic for the transitions bound electron states on the surface of liquid helium [53]. In limit weak electric fields, the Stark shifted transition computed from Eq. 2.14, revealing

appreciable linear Stark tuning rates $0.83\,\mathrm{GHz/Vcm^{-1}}$ for $1 \rightarrow 2$ transitions as shown in Fig. 2.3 (b). In case of large external fields which is not fulfilling the circumstance $\Delta E^1_{\mathrm{n}} \ll E_{\mathrm{n+1}} - E_{\mathrm{n}}$, then perturbation method is not significant and the correction term ΔE_{n} results nonlinear to $E_{\perp}$. In this case, the variational calculation of the Stark shift is in good agreement with the experiment [2] as shown in Fig. 2.4. In large external field, the image potential term V_{im} which is presented in Eq. 2.11 can be ignored and then the wave function $\chi_{\mathrm{n}}(z)$ is reduced.

2.2 Gravity waves and capillary waves

Gravity waves are disturbances that travel across the surface of a fluid, such as water, that are caused by the force of gravity. We focus on gravity waves on fluids, specifically their mathematical description and the physical phenomena associated with them. The simplest form of a gravity wave is a harmonic wave, which can be described by the equation:

$$y(x,t) \;=\; A\,cos\,(qx - \omega t) \tag{2.15}$$

where y is the displacement of the fluid from its equilibrium position, x is the position along the wave, t is the time, A is the amplitude of the wave, q is the wave number, and ω is the angular frequency of the wave. The gravity wave is a transverse wave, which means that the displacement of the fluid is perpendicular to the direction of wave propagation. In contrast, a longitudinal wave, such as a sound wave, has displacement parallel to the direction of wave propagation.

The dispersion relation for a gravity wave [54] is given by the equation [49]:

$$\omega^2 \;=\; gq\,\tanh\,(qd) \tag{2.16}$$

where g is the acceleration due to gravity, q is the wave number, d is the depth of the fluid, and $\tanh(kh)$ is the hyperbolic tangent function. This equation shows

that the angular frequency of the wave is dependent on the wave number and the depth of the fluid.

Capillary waves are waves that are caused by the surface tension of a fluid. They have much smaller wavelengths and higher frequencies than gravity waves. The dispersion relation for capillary waves on deep fluid [54] is given by:

$$\omega^2 = \frac{\sigma q^3}{\rho} \tag{2.17}$$

where σ is the surface tension of the fluid, ρ is the density of the fluid, and q is the wavenumber. Capillary waves are characterized by their small amplitude and short wavelength. They can caused by wind blowing over the surface of the fluid. The wavelength of these waves is usually less than 1 mm and the amplitude is usually less than a few micrometers. These waves are often observed on liquids with low viscosity and high surface tension, such as water and mercury [55, 56, 57].

The various excitations present in liquid helium, such as first, second, and third sound, rotons, and ripplons, which have an effect on the behavior of electrons in the substance. Phonons, are bulk density waves, and ripplons, which are surface waves, have the most significant impact on electrons in helium. These excitations limit the mobility of surface electrons and have an effect on the coherence properties of vertical Rydberg states [22, 39] as well as the states of electron motion [23].

Classically, ripplons are defined as capillary waves on the surface of liquid helium, which liquid helium is an excellent electron substrate. At low temperature T below 0.7 K, the only important electron coupling to the outside world is to thermally excited height variances $\delta(\boldsymbol{r}, t)$ of the liquid helium surface, where $\boldsymbol{r}$ is the coordinate plane of the electron. These variances are characterized as propagating capillary waves, or ripplons, given by the following dispersion relation

$$\omega = 2\pi f = \sqrt{gq + \frac{\sigma q^3}{\rho} \tanh(qd)}, \tag{2.18}$$

where: $q = 2\pi/\lambda$ is the wavenumber and λ is the wavelength for surface waves;

$\rho = 0.145$ g/cm^3 and $\sigma = 0.37$ erg/cm^2 are the mass density and surface tension of the superfluid He^4, respectively; $g \approx 980$ cm/s^2 is the acceleration due to gravity; and d is is the depth of the liquid helium. The first term of Eq.(2.18), describes a gravity wave whereas the second part is associated with a capillary wave. The minimum in the phase velocity corresponds to the transition between the gravity and capillary regimes and it occurs at $q_{\rm c} = \sqrt{g\rho/\sigma}$. For case $q \gg q_{\rm c} = \sqrt{g\rho/\sigma}$, the capillary wave term gives the frequency spectrum of the ripplon when gravity waves are neglected. For liquid ^{4}He, the value of $q_{\rm c}$ is ~ 20 cm^{-1}. This means that the capillary waves influence the dispersion relation when the wave number $q \gg 20$ cm^{-1}. Indeed, the range of the ripplon wave number q depends on the distance between two plates and level of helium. For a free electron, the wave number is of the order of the thermal de Broglie wave vector $q \sim 2k_{\rm T}$, where $k_{\rm T} = \sqrt{2m_{\rm e}k_{\rm B}T}/\hbar$. Therefore, for the T region 0.1 K $\leq T <$ 1 K, the range of relevant ripplon wave numbers q is approximately between $\sim 10^5$ and $\sim 10^6$ cm^{-1}, which is great than $q_{\rm c} = 20$ cm^{-1}. Therefore, for depth helium ($d > 100$ nm $\rightarrow \tanh(qd) \sim 1$), the gravity term is not important in the ripplon dispersion law. The dispersion relation Eq. (2.18) reduces to Eq. 2.17.

The energy of ripplons, which can play a part in electron scattering , is given [1] by

$$\hbar\omega = \sqrt{\frac{\sigma}{\rho\hbar}}\left(8m_{\rm e}k_{\rm B}{\rm T}\right)^{3/4},$$

which is lower than the thermal energy $k_{\rm B}$T. For instance, $\hbar\,\omega_q$ is $\sim 1\times10^{-2}$ K at $T = 1$ K and $\sim 4\times10^{-4}$ K at $T = 0.01$ K. This implies that only long wavelength ripplons with an energy smaller than the thermal energy can scatter with electrons. Under a strong magnetic field, the wave numbers of ripplons involved in scattering are restricted by another condition, $q \sim \sqrt{2}/l_B$, where $l_B \propto 1/\sqrt{B}$ gives the electron magnetic length. The occupation number N for ripplons is given by

$$N_{\rm q} = \left\{\exp\left(\frac{\hbar\Omega_{\rm q}}{k_{\rm B}{\rm T}}\right) - 1\right\}^{-1}, \tag{2.19}$$

Saitoh computed the relaxation time $\tau_{\mathrm{R}}(\varepsilon_{\mathrm{k}})$ for electron-ripplon scattering [52]:

$$\frac{1}{\tau_{\mathrm{R}}(\varepsilon_{\mathrm{k}})} = \frac{k_{\mathrm{B}}\mathrm{T}}{4\hbar\sigma a^2}\left[\frac{(eE_{\perp}a)^2}{\varepsilon_{\mathrm{k}}} + 2(eE_{\perp}a)\left(\ln\frac{16E_{\mathrm{b}}}{\varepsilon_{\mathrm{k}}} - 3\right) + \frac{3\varepsilon_{\mathrm{k}}}{2}\left\{\left(\ln\frac{16E_{\mathrm{b}}}{\varepsilon_{\mathrm{k}}} - \frac{19}{6}\right)^2 + \left(\frac{\pi^2}{3} - \frac{115}{36}\right)\right.\right., \tag{2.20}$$

where $a = a_0/\Lambda$ presents the effective Bohr radius when there is no electric field and E_{b} is obtained as

$$E_{\mathrm{b}} = \frac{\hbar^2}{2m_{\mathrm{e}}b^2}. \tag{2.21}$$

The relaxation time approximation produces a non-equilibrium electron distribution function when the drift field $\vec{E}_{\parallel}$ is parallel to the electron plane, which is defined by

$$f(\varepsilon_{\mathrm{k}}) \simeq f_0(\varepsilon_{\mathrm{k}}) - e\tau_{\mathrm{R}}(\varepsilon_{\mathrm{k}})\,\vec{v}_{\mathrm{k}} \cdot \vec{E}_{\parallel}\frac{\partial f_0}{\partial \varepsilon_{\mathrm{k}}}, \tag{2.22}$$

where $\vec{v}_{\mathrm{k}}$ gives the electron velocity, and the equilibrium electron distribution function $f_0(\varepsilon_{\mathrm{k}})$ which, for the non-degenerate system, is

$$f_0(\varepsilon_{\mathrm{k}}) = \frac{\pi\hbar^2 n_{\mathrm{e}}}{m_{\mathrm{e}}k_{\mathrm{B}}\mathrm{T}}\exp\left(-\frac{\varepsilon_{\mathrm{k}}}{k_{\mathrm{B}}\mathrm{T}}\right). \tag{2.23}$$

The drift current density is given by

$$\vec{j} = e\int_0^{\infty} d\varepsilon_{\mathrm{k}}\vec{v}_{\mathrm{k}}D(\varepsilon_{\mathrm{k}})\,f(\varepsilon_{\mathrm{k}}), \tag{2.24}$$

and the conductivity is calculated from Ohm's law:

$$\sigma_0 = \frac{e^2}{m_{\mathrm{e}}}\int_0^{\infty} d\varepsilon D(\varepsilon)\left[-\tau_{\mathrm{R}}(\varepsilon)\varepsilon\frac{\partial f_0}{\partial \varepsilon}\right]. \tag{2.25}$$

Here $D(\varepsilon) = m_{\mathrm{e}}/\pi\hbar^2$ defines the electron density of states in 2D. The DC electron

mobility $\mu = \sigma_0/n_e e$ is obtained by

$$\mu = \frac{e}{m_e} \langle \tau_R(\varepsilon) \rangle \tag{2.26}$$

where the average of $\tau_R(\varepsilon)$ presents from

$$\langle \tau_R(\varepsilon) \rangle = \frac{1}{n_e} \int_0^\infty d\varepsilon D(\varepsilon) \left[-\tau_R(\varepsilon) \varepsilon \frac{\partial f_0}{\partial \varepsilon} \right] = \int_0^\infty d\varepsilon \frac{\varepsilon \tau_R(\varepsilon)}{k_B^2 \, T^2} e^{-\varepsilon/k_B T}. \tag{2.27}$$

Using the approximation $\langle \tau_R(\varepsilon) \rangle = \tau_R \, (\varepsilon = k_B T)$ in Eq. (2.20), the average collision time in electron-ripplon scattering at $\vec{E}_\perp = 0$ can be approximated by

$$\tau_R(T) \equiv \langle \tau_R(\varepsilon) \rangle \simeq \frac{8\hbar\sigma a^2}{3k_B^2 \, T^2} \left(\ln 0.67 \frac{E_0}{T} \right)^{-2}. \tag{2.28}$$

On applying the pressing field, the ripplon-limited collision time at low temperature $T < 0.8$ K is affected (suppressed) by increase of $\vec{E}_\perp$. This is because, increased $\vec{E}_\perp$will leads to the electrons being pressed more strongly against the helium surface, leading to an enhancement of the electron-ripplon interaction.

In the limit of the strong field, therefore, Eq. 2.20 is simply obtained by

$$\frac{1}{\tau_R(\varepsilon)} \simeq \frac{k_B T}{4\hbar\sigma a^2} \frac{(eE_\perp a)^2}{\varepsilon}, \tag{2.29}$$

and Eq. (2.27) yields $\langle \tau_R(\varepsilon) \rangle = 8\hbar\alpha / (eE_\perp)^2$ which depends only on the holding field.

In our case for electrons on superfluid He^4, the frequency of gravity waves is $\omega \approx 3.83\sqrt{gd}\, q$, where the number 3.83 is a geometry factor of the experimental cell and q is the wave number of a standing wave ($q \propto 1/R$), R is radius of the circular liquid pool [34]. Then, for $d = 1.3$ mm and $R = 10$ mm, the lowest resonant frequency is $f \approx 0.609\sqrt{gd}/R \approx 5.28$ Hz.

2.3 Edge-magnetoplasmons in two-dimensional electron systems

To illustrate the concepts and set the scene, we first consider the classic cases of plasmons and magnetoplasmons in 2D layers of electrons on solid (e.g. semiconductor) substrates. Then, in Sec 2.3.3, we will return to see how similar ideas can be developed to describe wave modes in our system of interest i.e. 2D electron layers on the surface of liquid helium."

2.3.1 Plasmons and magnetoplasmons

Plasmons are collective excitations formed in the electron gas or liquid, which propagate as longitudinal charge density oscillation through the bulk on the surface. The Coulomb force between charged particles is responsible for creating plasma oscillations. When a group of electrons in width L slightly shifts with a small distance δx, in relation to the positive background, a fluctuation in charge density occurs, represented by:

$$\rho_0 = en\delta x, \tag{2.30}$$

here n_e is the electron density. The shifted 2D electron in an infinite - size system is provided in Fig. 2.5. Moreover, this fluctuation creates an internal electric field $\boldsymbol{E}$, causing the electrons to move and correct the electrical deviation. If there is minimal scattering of electrons, the electrons will continue to move beyond their equilibrium positions and the charge density fluctuation will change in sign, repeating the cycle in the opposite direction resulting in the formation of plasma oscillations.

In the plasma oscillation, the motion of electrons is governed by the equation of motion:

$$m\delta\ddot{x} = -e\boldsymbol{E}. \tag{2.31}$$

In the case of two narrow charged stripes, $\boldsymbol{E}$ represents the internal electric field

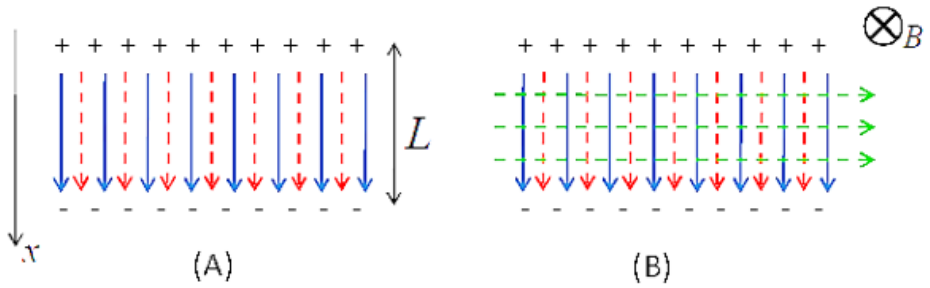

Figure 2.5: (A) Electric charge (+ and −), electric field (blue solid arrows) and electric current (red dashed arrows) in the 2D plasmon mode at $B = 0$. (B) The same at finite magnetic field B perpendicular to the plane of the 2DES (the dashed-dotted arrows show the Hall current), Figure taken from Ref. [4].

and its strength should be

$$E \simeq \frac{\rho_0}{4\pi\epsilon_0\kappa L} \tag{2.32}$$

κ can be presented the relative dielectric constant of the surrounding medium. From Eq. 2.31 is

$$\delta\ddot{x} + \omega_{\mathrm{p}}^2\delta x = 0, \quad \omega_{\mathrm{p}}^2 \simeq \frac{ne^2q}{4\pi\epsilon_0\kappa m}. \tag{2.33}$$

$q \simeq 1/L$ defines the wavenumber of the plasma oscillation. ω_{2Dp} is an estimation of the 2D plasma frequency.

When the charge is $\rho(\boldsymbol{r}, t)$, an electric field $\boldsymbol{E} = -\nabla\varphi(\boldsymbol{r}, t)$; φ is the potential of the electric field, and current density $j(r, t)$ are presented, the fluctuations in the regime are governed by the continuity equation,

$$\frac{\partial\rho}{\partial t} + \nabla\boldsymbol{j} = 0 \tag{2.34}$$

then Poisson's equation is,

$$\nabla[\kappa(z)\nabla\varphi] = -\frac{\rho}{\epsilon_0}\delta(z), \tag{2.35}$$

and Ohm's law,

$$j_\alpha = \sigma_{\alpha\beta}E_\beta = -\sigma_{\alpha\beta}\nabla_\beta\varphi, \quad \{\alpha, \beta\} = \{x, y\}. \tag{2.36}$$

Here $\sigma_{\alpha\beta}$ describes the conductivity tensor. In general, conductivity encompasses both temporal and spatial dispersion; it is represented as $\sigma_{\alpha\beta} = \sigma_{\alpha\beta}(\boldsymbol{q}, \omega)$. When solutions in the equations are given as $\{\rho, \varphi, j\} \propto \exp(iqx - i\omega t)$ and the relative dielectric permittivity κ does not vary with z, the Fourier components of the potential are represented as $\varphi = \varphi_{q\omega}(z)$,

$$\frac{\partial^2 \varphi}{\partial z^2} - q^2 \varphi = \frac{4\pi i}{\omega \kappa} \left(q_\alpha \sigma_{\alpha\beta} q_\beta \right) \varphi \delta(z). \tag{2.37}$$

Due to the δ-function on the right side, the potential can be provided, $\varphi(z) = \varphi(0) \exp(-|qz|)$ and the dispersion equation for the plasma wave is

$$\left(1 + \frac{2\pi i}{\omega \kappa |q|} q_\alpha \sigma_{\alpha\beta} q_\beta \right) \varphi(0) = 0. \tag{2.38}$$

The plasma waves can be found ($\varphi(0) \neq 0$) when the expression in the round brackets should vanish.

When $B = 0$, the conductivity tensor is diagonal; $\sigma_{\alpha\beta} = \sigma_{xx} \delta_{\alpha\beta}$ and, in the Drude model, it can be written as,

$$\sigma_{xx}(\omega) = \frac{ne^2}{4\pi \epsilon_0 m} \frac{i}{\omega + i/\tau}. \tag{2.39}$$

τ is a relaxation time. From Eqs. (2.38) and (2.39), the frequency of 2D plasmas can be

$$\omega_{\mathrm{p}}^2(q) = \frac{ne^2}{2\epsilon_0 \kappa m} |q|, \quad \omega\tau \gg 1. \tag{2.40}$$

This result aligns with the simple calculation given in Eq. 2.33), with the exception of a numerical factor of 2π. The 2D plasma oscillation has a gapless frequency $\omega_{\mathrm{p}} \propto q^{1/2}$. The 2D plasmons have been observed in a GaAs/AlGaAs heterojunction [58] and in a SSE system on liquid helium [59]. In the first instance, the plasma frequency is of the order of 1THz, while in the latter, it is of the order of 100MHz. When a magnetic field B is present, the dispersion equation for a bulk

magnetoplasma should be.

$$\omega_{\rm mp}^2 = \omega_{\rm p}^2 + \omega_{\rm c}^2. \tag{2.41}$$

In the case of a 2D bulk magnetoplasmaon, there is a gap in the frequency; the frequency $\omega_{\rm mp}$ must be greater than the cyclotron frequency $\omega_{\rm c} = eB/m$. The Drude formula is used to calculate the diagonal and Hall conductivities and can be presented as:

$$\sigma_{xx}(\omega, B) = \frac{ne^2}{4\pi\epsilon_0 m}\frac{i\omega}{\omega^2 - \omega_{\rm c}^2} \tag{2.42}$$

$$\sigma_{xy}(\omega, B) = \frac{ne^2}{4\pi\epsilon_0 m}\frac{\omega_{\rm c}}{\omega^2 - \omega_{\rm c}^2} = \frac{\omega_{\rm c}}{i\omega}\sigma_{xx}. \tag{2.43}$$

In a high magnetic field and at a low frequency, the Hall conductivity σ_{xy} can be greater than the diagonal conductivity σ_{xx}. However, the Hall conductivity does not affect the frequency of bulk magnetoplasma oscillations. In a uniform and isotropic 2D electron system that is infinite, the Hall current flows perpendicular to the internal electric field and does not affect the charge density fluctuation. But, in a finite 2D electron system, a large Hall current can cause changes in the density fluctuation.

2.3.2 Edge magnetoplasmon (EMP)

When a magnetic field is applied perpendicular to a 2D electron system, collective modes can emerge near the edge of the system. One of the most noteworthy of these is the edge magnetoplasmon (EMP); where the fluctuation of electron density travels along the edge of the 2D system.

To study EMPs, a finite 2D electron system is examined. In a high magnetic field (B), a 2D electron sheet of finite size is shown in Fig. 2.6. The negative charge of electrons is balanced by a fixed positive background. When the electron layer is displaced from the background, a fluctuation in charge density is created. The linear charge densities of the two positive and negative stripes are $\pm\rho_1$. As a result of this density fluctuation, an internal electric field E_y is generated. In a high

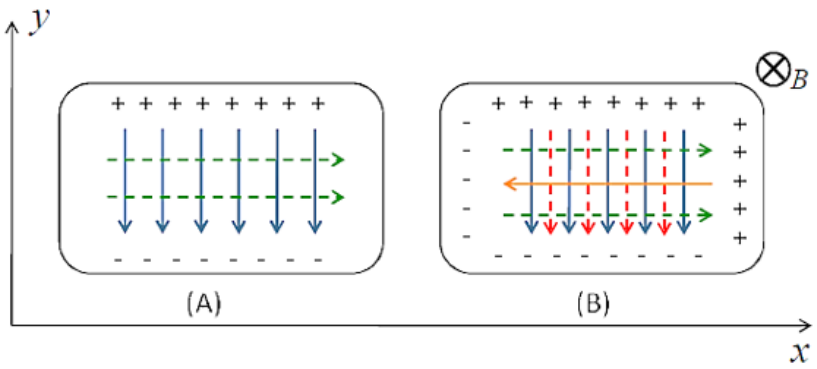

Figure 2.6: A Dipolar Edge Magnetoplasmon (EMP) in a finite-size system in a high magnetic field B at the initial (A) and subsequent (B) moments. The blue and orange solid lines depict the electric fields and the red and green dashed lines represent the electric currents, Figure taken from Ref. [4].

magnetic field ($\omega_c\tau \gg 1$), the Hall current (j_y) is much larger than the diagonal current (j_x) and the electrons move perpendicular to the internal field. Since the sample is finite, electrons reach the edge and accumulate near it, creating two positive and negative charge stripes near the edge. The linear charge densities are $\pm\rho_2$ and another electric field E_x is produced. Additionally, another Hall current j_y is present and changes the sign of the fluctuation ρ_1. This process repeats, maintaining the rotating pattern of charge, field, and current distribution, until the initial fluctuation is dampened due to scatterings and dipole radiation. This oscillating process of charge, field, and current in the finite-size 2D system is the fundamental concept of EMP.

A approximation estimate of the EMP frequency is found through a simple analysis. Based on the previous qualitative discussion, the continuity equations are written for a unit square:

$$-i\omega\rho_1 + j_y = 0, \quad -i\omega\rho_2 + j_x = 0, \tag{2.44}$$

for Ohm's law at $\sigma_{xy} \gg \sigma_{xx}$,

$$j_x = \sigma_{xy} E_y, \quad j_y = -\sigma_{xy} E_x, \tag{2.45}$$

and an estimate of the field generated by the charge density fluctuations is obtained.

$$E_x \simeq \frac{\rho_2}{4\pi\epsilon_0 \kappa L_x}, \quad E_y \simeq \frac{\rho_1}{4\pi\epsilon_0 \kappa L_y}. \tag{2.46}$$

Then, the EMP frequency is given by

$$\omega_{\mathrm{EMP}} \simeq \frac{\sigma_{xy}}{4\pi\epsilon_0 \kappa L} \propto \frac{n}{B\kappa L}. \tag{2.47}$$

The typical lateral size of the system can be defined as L. For instance, in a surface electron system on liquid helium, the estimated frequency of the EMP ($n \approx 10^{11}$ m^{-2}, $L \approx 1.0 \times 10^{-2}$ m, $\kappa = 1$ and $B \approx 10$ T) can exist in 1kHz range. In the estimation of the EMP frequency, the electric fields generated by the two

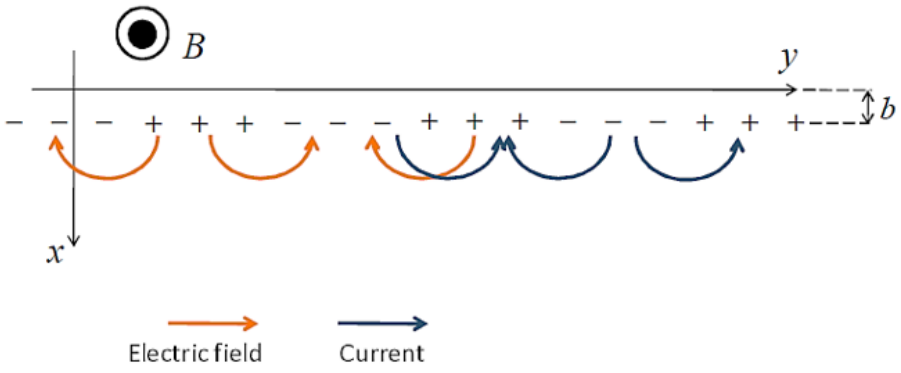

Figure 2.7: The density fluctuation near the edge. The orange line represents the electric field and the dark blue one represents the current. The magnetic field is applied perpendicular to the system, Figure taken from Ref. [4].

narrow charge stripes are approximate and differ from the actual ones. In reality, the fields are inhomogeneous and require more precise calculations. To obtain a more accurate frequency of EMP, the electric fields and currents near the edge are taken into consideration. surface electrons are assumed to be distributed in

the half-plane; $z = 0, x \geq 0, -\infty < y < +\infty$. In Fig. 2.7 illustrates the density fluctuation near the edge. According to the Volkov and Mikhailov theory [60], the potential near the edge is

$$\varphi(\boldsymbol{r}, t) = \varphi(x, z) \exp(iqy - i\omega t), \quad \omega = \omega' + i\omega'' \tag{2.48}$$

$$\varphi(x, z = 0) \approx \tfrac{-2Q}{4\pi\epsilon_0\kappa} \ln(|q|x), \quad b \lesssim x \lesssim |q|^{-1}. \tag{2.49}$$

Here q is the wave number of EMP, in particular, in a circular 2DES electron system (2DES) with a radius R and perimeter of $2\pi R$, the EMP wave numbers are $q = 2\ \pi\ \mathrm{m}\ /\ \mathrm{P} = \mathrm{m}\ /\ \mathrm{R}$, m=1,2,(the number of first mode of the frequency)... Q is the linear charge density in the width b, which is much smaller than the wavelength of EMP ($b \ll 2\pi/|q|$). Q is obtained from the current at the edge. The charge conservation law and the definition of the current given by:

$$i\omega Q \approx j_x(x \sim b). \tag{2.50}$$

Q has the same periodicity as the potential and $Q \propto \exp(iqy - i\omega t)$. In a large magnetic field ($\sigma_{xx}/\sigma_{xy} \ll 1$), j_x is

$$j_x \simeq \sigma_{xy} E_y \approx -iq\sigma_{xy}\varphi(x, z = 0). \tag{2.51}$$

Using Eq. 2.49, Eq. 2.50 and Eq. 2.51, the self-consistent relation is given by:

$$\varphi(x, z = 0) \approx \frac{2q\sigma_{xy}}{4\pi\epsilon_0\kappa\omega}\varphi(x \sim b, z = 0) \ln(|q|x). \tag{2.52}$$

In this situation, the event should be limited to the vicinity of the edge ($x \sim b$) and φ can be removed from both sides of Eq. 2.52. If the fluctuation occurs within a range much smaller than the wavelength EMP($|qb| \ll 1$), the frequency ω_{EMP} is given

$$\omega_{\mathrm{EMP}} \equiv \omega' = -\frac{q\sigma_{xy}}{2\pi\epsilon_0\kappa} \ln(|q|b), \quad |qb| \ll 1. \tag{2.53}$$

With using Eq. 2.48, the dissipation rate, ω", can also be determined. In the theory developed by Volkov and Mikhailov [61], it is defined as the ratio of Joule heating to the total energy,

$$\Gamma_{\text{emp}} \equiv |\omega''| \sim \frac{\sigma_{xx}\int E^2 dx}{\int \frac{1}{2}e\varphi dx} \sim \frac{2\sigma_{xx}\int_b^\infty \left(\frac{Q}{4\pi\epsilon_0\kappa}\right)^2 \frac{dx}{x^2}}{\varphi(b)Q} \sim \frac{-\sigma_{xx}}{4\pi\epsilon_0\kappa b}\frac{1}{\ln(|q|b)}. \tag{2.54}$$

The dissipation rate is equivalent to the linewidth of EMP and the damping of the EMP is directly proportional to the diagonal conductivity σ_{xx}. The value of b represents the width in which the electron density fluctuation is concentrated. In the model of a 2D electron system with a sharp boundary, like a step-function, the length $b \equiv |l|$ is determined by σ_{xx},

$$l \equiv l(\omega) = \frac{i\sigma_{xx}(\omega)}{2\epsilon_0\kappa\omega}, \quad \sigma_{xx}(\omega) = \sigma'_{xx} + i\sigma''_{xx}. \tag{2.55}$$

However, in a realistic system, the electron density profile is smooth at the boundary with a characteristic width w. The EMP charge density fluctuation is not localized near the boundary at a length smaller than a. For $|l| < w$, the length $|l|$ is replaced by w. The EMP frequency should be rewritten accordingly.

$$\omega_{\text{EMP}} = -\frac{q\sigma_{xy}}{2\pi\epsilon_0\kappa}[\ln(|q|w) + C]. \tag{2.56}$$

The constant C depends on the details of the equilibrium density profile.

As in our case, κ can be presented the relative dielectric constant of the surrounding medium. Then, we can replace κ by $\epsilon_{^4He}$ with value 1.057. With C =1, $q = 1/R$, R= 10 mm, $B = 0.81$ T and $w = 0.1$ mm. Also, with defining Hall conductivity $\sigma_{xy} = n_{ee/B}$, the frequency of EMP for $n_e = 1.4 \times 10^6$ cm^{-2} and $n_e = 2.2 \times 10^6$ cm^{-2} is given 2.28 kHz, and 3.58 kHz, respectively.

2.3.3 EMP in surface electrons on liquid helium

As discussed earlier, for our system of interest, an electric field is applied to press the 2DES onto the liquid surface. In this system, the electric field from the 2DES is attracted to image charges in the electrodes and does not extend beyond the distance d between the 2DES and electrodes. This is known as "screening" and a 2DES on liquid helium is generally considered a screened system. Research by Lea et al. [62], has shown that the penetration length is inversely proportional to the magnetic field B^{-1} in the Drude formalism.

In the $x-y$ plane, when a potential wave of the form $V = A\exp(i\omega t)\exp(-ikx)$ is present in the 2DES, the conservation of alternating current can be expressed as:

$$\nabla \cdot \boldsymbol{J} = -i\omega C' V. \tag{2.57}$$

Here i is the imaginary unit and $C' \simeq \epsilon\epsilon_0/h$ is a capacitance per unit area between the electrons and the electrodes. $J = (J_x, J_y)$ is the current density. Also, the relationship between J and the in-plane electric field $\mathcal{E}$ is

$$J = \sigma\mathcal{E} = -\sigma\nabla V. \tag{2.58}$$

Substitution of Eq. 2.58 into Eq. 2.57 provides the 2D wave equation

$$\frac{\partial V^2}{\partial^2 x} + \frac{\partial V^2}{\partial^2 y} = \frac{i\omega C' V}{\sigma_{xx}}. \tag{2.59}$$

In high magnetic field, the dissipation relation can be

$$k^2 = -i\omega C'/\sigma_{xx}, \tag{2.60}$$

and the wave number k is expressed by

$$k = (1-i)/\delta, \quad \delta = \sqrt{\frac{2\sigma_{xx}}{\omega C'}}. \tag{2.61}$$

The potential transforms into a strongly damped wave in a rectangular geometry with a magnetic field, with propagation parallel and perpendicular to the edge. The wave numbers $k_|$ and $k_\perp$ are present in the 2D electron system above liquid helium. The electron sheet is rigidly confined and the boundary condition requires zero current density perpendicular to the edge, $J_\perp = 0$. In the collisionless limit, characterized by $\omega\tau \gg 1$ and the Drude formalism, the penetration depth, also known as the skin depth, is presented as [62].

$$\exp\left(-s^{-1}\omega_c y\right) \equiv \exp\left(-y/\delta_\perp\right), \quad \delta_\perp = s\omega_c^{-1}b^{-1}. \tag{2.62}$$

The plasma velocity in the screening 2D electron system in a zero magnetic field is represented by $s = (ne^2d/m\epsilon\epsilon_0)^{1/2}$. For the Corbino disk electrodes, which consist of two circularly symmetric metals, the penetration length of the potential from the edge is equal to δ [62]. According to the Drude model, when $\omega\tau \ll 1$, the penetration length δ is inversely proportional to the magnetic field. In both rectangular and circular geometries, the density fluctuation caused by the potential wave decreases as the magnetic field increases.

2.4 Inter-edge magnetoplasmons

Inter-edge magnetoplasmons (IEMP) are an extension of the edge magnetoplasmon modes. Edge magnetoplasmons propagate along the outer boundary of a 2D electron system, while inter-edge modes travel along the internal boundary between two sections of a sample that may have different 2D electron densities and/or magnetic fields. In the case of a sharp boundary, the spectrum of inter-edge magnetoplasmons moving along the boundary of two half-planes with different conductivity tensors $\sigma^H_{\alpha\beta}$ and $\sigma^L_{\alpha\beta}$ is given by the expression in reference [63, 64]:

$$\omega_{iemp} = \frac{2q_y\left(\sigma^H_{yx} - \sigma^L_{yx}\right)}{\kappa}\left(\ln\frac{2}{|q_y|\,l} + 1\right), \quad \left|q_y\bar{l}\right| \ll 1, \tag{2.63}$$

where $\bar{l} = (l_H + l_L)/2$, and l_H and l_L are defined using σ_{xx}^H and σ_{xx}^l by similar equations to Eq. 2.55. If the edge is smooth with a transition layer width of w larger than $|\bar{l}|$, the length $\bar{l}$ in Eq. 2.63 should be replaced by w [65]:

$$\omega_{i\in mp} = \frac{2q_y\left(\sigma_{yx}^H - \sigma_{yx}^L\right)}{\kappa}\left(\ln\frac{1}{|q_y|\,w} + C\right), \quad |q_y|\,w \ll 1, \tag{2.64}$$

where the constant C depends on the specific equilibrium density profile. Inter-edge magnetoplasmon modes have been experimentally observed in Refs [66, 67, 68].

From Sec. 2.3.2, with $\sigma_{yx}^{\mathrm{H/L}} \propto n_{\mathrm{H/L}}/B$, then , the frequency of IEMP: $f_{IEMP} =$ 9.5 $\times 10^{11}$ Hz.

2.5 Transport properties parallel to the surface

The mobility of electrons is an important physical quantity that is used to study the transport properties of various 2D materials. The unique features of the electron mobility are observed when the temperature is changed. Measurements of the surface electrons' mobility on ^{4}He were carried out in the electron-helium vapor atom scattering regime [69, 70, 71], and that for electron-ripplon scattering [72]. The mobility of electrons on the surface of ^{4}He increases with decreasing temperature. In the regime above 0.3 K, the main scatterers with SEs are helium vapor atoms and the ripplon scattering becomes dominant below 0.3 K.

Figure 2.8 shows the temperature dependence of the electron mobility above the liquid helium ^{4}He, ^{3}He [5]. Theoretical calculations of the surface electrons' mobility were performed by Saitoh [52]. They show that the mobility is inversely related to the helium vapor density in the gas scattering region. The mobility in the ripplon scattering region exhibits weak temperature dependence. For ^{3}He, the transition from gas dominant to ripplon dominant happens at 0.3 K, and the transition occurs at 0.8 K for ^{4}He. The results of the theoretical calculation agree with the experimental results in the vapor atom and ripplon scattering temperature regions. Despite the large viscosity of ^{3}He, ripplons can still be found on the

surface down to 0.1 K. The mobility drops abruptly at a lower temperature as the SE undergo phase transition from the electron on liquid to the Wigner solid. The increase in the surface deformation due to the localized electrons causes the effective mass of the electrons to increase, which decreases the mobility.

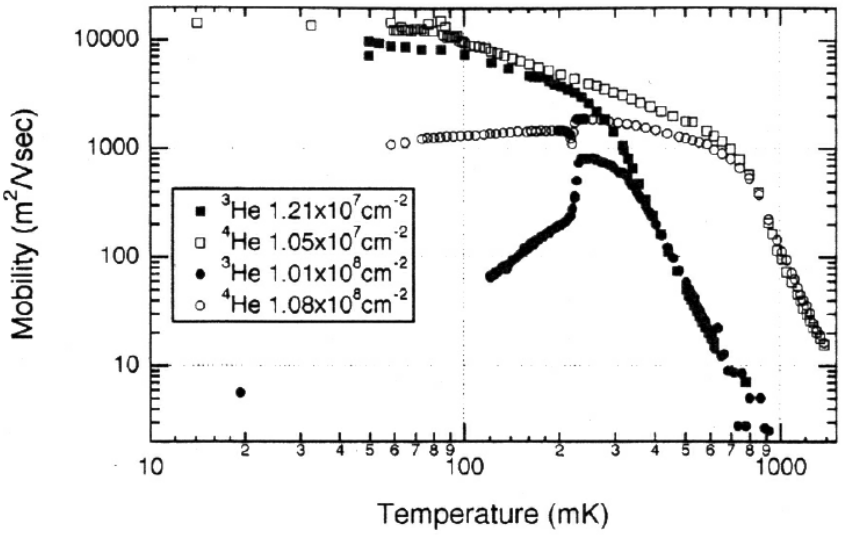

Figure 2.8: SSE mobility as a function of temperature on ^{3}He and ^{4}He, Figure taken from Ref. [5].

The transition temperature to Wigner solid T_m is theoretically obtained by [73]

$$T_m = \frac{1}{\Gamma}\frac{n_e^{1/2}e^2}{4\pi^{1/2}\epsilon_0 k_B}. \tag{2.65}$$

Where Γ is a numerical factor, which is obtained by $\Gamma = \frac{n^{1/2}e^2}{4\pi^{1/2}\epsilon_0 k_B T} \simeq 140$, n_e is the electron density.

2.6 Quantization and collision broadening

The motion of electrons parallel to the surface is free with a continuous energy spectrum which is given by $p^2/(2m_e)$, where $\mathbf{p} = p_x\mathbf{e}_x + p_y\mathbf{e}_y$ is the momentum of the electron and $\mathbf{e}_i$ is the unit vector in i direction. When a static magnetic field $\mathbf{B} = B_z\,\mathbf{e}_z$ is applied perpendicular to the surface, the in-plane electron states get squeezed into a set of Landau levels with an equidistant energy level spacing

given by $\hbar\omega_c(l{+}1/2)$, where $\omega_c = eB/m_e$ is the cyclotron frequency and $l = 0,1,..$ is the quantum number. Thus the surface electrons on liquid helium can present a singular system of free particles with discrete spectrum in the case where the interactions can be neglected. Therefore, the SEs levitate above a clean surface of liquid helium, with no defects or impurities. The only two scatterers are helium vapor atoms and capillary waves (ripplons) whose densities can be decreased by decreasing the temperature. This scattering leads to collisional broadening Γ_n of the density of states. The density of states function is presented by a set of Gaussian functions.

2.6.1 Dynamics of surface state electrons on liquid helium exposed to microwave intersubband excitation and quantizing magnetic field

Recent research has shown that in two-dimensional electron systems, including in semiconductors, the electrical resistance decreases and may approach zero when they are subjected to combined magnetic and microwave influences. A study of the magnetotransport of a two dimensional electron gas in GaAs/AlGaAs heterostructures under a magnetic field (B) and strong microwave (MW) radiation revealed an unexpected discovery, that of MW-induced resistance oscillations (MIRO) [14, 74]. These oscillations emerge periodically and they can be controlled by the ratio of the microwave frequency to the cyclotron frequency: (ω/ω_c). With high radiation power, the minima of the periodic oscillations can evolve into zero-resistance states [75, 76]. The positions of the resistance minima obey a universal law which is given by $\omega/\omega_c = m{+}1/4$ (where $m = 1, 2, \ldots$) and selecting the number m responsible for the major contribution to resistance minima at a given magnetic field [75]. These positions of the resistance minima are related to the absolute negative conductivity of the electrons [77], which is associated with photon-assisted scattering of electrons off impurities [78, 79, 80, 81].

Similar behaviour of MW-induced conductivity oscillations (MICO) and ZRS

were observed in the 2D electron gas on liquid helium [27, 29]. In studies of electrons on the surface of liquid helium, the MW-induced conductivity oscillation σ_{xx} was experimentally obtained by use of the Corbino geometry. These oscillations are unlike the MW-induced resistance oscillation (MIRO), which appear only when the excitation energy $\Delta_{2,1} = \Delta_2 - \Delta_1 = \hbar\omega_{2,1}$ is tuned to the resonance with the MW field ($\Delta_{2,1} = \hbar\omega$) through the use of the Stark effect for the one dimensional potential well $V(z)$. The remarkable features of the magnetoconductivity of SE gas on liquid helium are explained by a theory based on the nonequilibrium population of the first excited surface subband [82, 83] which leads to sign-changing terms in the electron magnetoconductivity and attains to absolute negative conductivity at high radiation power. Indeed, zero-resistance state (ZRS) coincides with nonequilibrium spatial redistribution of the 2D electrons from the center to the edge of the electron spot [8] and excitation of self-generated oscillations (SGO) of the charge density [34]. The result of the of a further experimental study of SGO of surface state electrons on liquid helium, for short length signals around (5 ms), which is presented in Fig. 2.9.

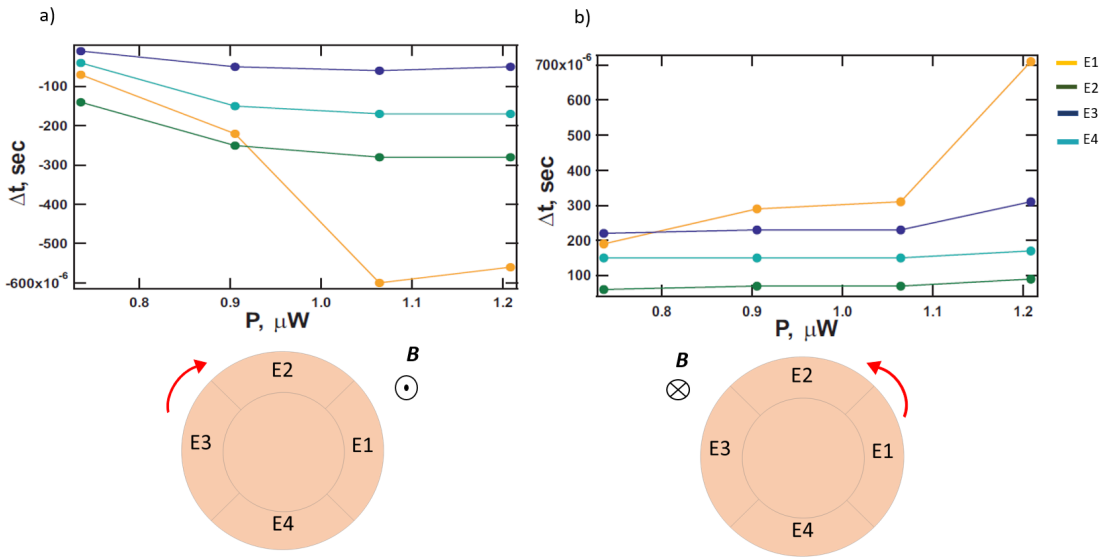

Figure 2.9: (a) and (b) The sum of phase shifts of oscillations between neighboring segments. It is an evidence of charge circular flow in the system under microwave excitation. The direction of charge flow change with polarity of magnetic field and coincides with direction of edge magnetoplasmons propagation (From [6], with permission).

The Corbino geometry cell is used with one of the ring electrodes divided into 4 segments and measure ac transient current for each segment. Cross-correlation function analysis of obtained data shows a phase shift between current oscillations for different segments that implies existence of circular charge flow within the electron layer. It is found that the charge flow changes its direction when the polarity of the magnetic field is reversed. The direction of the charge flow coincides with the direction of edge magneplasmons propagation. In fact, the self-generation of audio-frequency current oscillations at an electrode, we point out that the damping of the oscillations becomes negative, which agrees with $\sigma_{xx}<0$.

Moreover, experimental studies of MICO induced by inter-subband MW excitation led to discovery of new phenomena, including the resonant photovoltaic effect and spatial redistribution of electrons [8], an incompressible state [25]. These phenomena are manifested near the experimental condition $\sigma_{xx} \to 0$. Therefore, absolute negative conductivity can lead to instability of the spatially uniform distribution of the surface of electron above liquid helium. These new observations are interpreted by using the Coulombic effect, which favors the formation of domains of varying densities [26]. Domains eliminate or greatly reduce regions with negative conductivity

2.7 Density domains

A review of the density domain arrangement sheds light on the fascinating discoveries made in the field of photo-excited electron gas [8]. When the electron system reaches a state of negative conductivity (which is one of the condition for our experiment), it becomes unsteady and requires a certain amount of local current density to regain stability. This instability can result in a current distribution pattern where current flows in equal magnitudes but in opposite directions in neighboring domains. The location of the domain wall determines the overall current, and the current pattern in the Corbino geometry is assessed by connecting the edge current strips into a circular shape. The surface electrons on liquid helium represent a highly

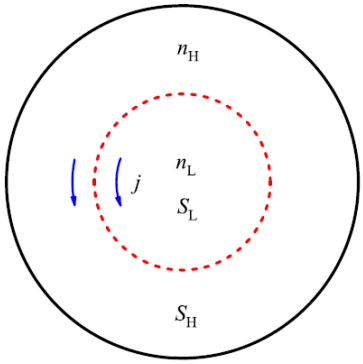

Figure 2.10: Schematic of the formation of the density distribution with a domain wall for the Corbino geometry, Figure taken from Ref. [7].

correlated system. The average kinetic energy is very much smaller than the Coulomb interaction potential energy per electron.

By tracking the changing of σ_{xx} minima under changes in the surface electron density n_e: when varying electron density at a fixed B magnetoconductivity for the first time becomes zero (the corresponding density is n_L). Further increase of density will make σ_{xx} negative, but in an experiment the system will keep $\sigma_{xx} = 0$. Then, at certain higher value of electron density, σ_{xx} becomes positive again. This point gives n_H. The electron system with $n_L < n_e < n_H$ will eventually be divided into domains with two different electrons densities n_L, n_H.

Fig. 2.10 shows the simplest stable distribution of the density with a domain wall. At $\sigma_{xx} < 0$, it is assumed that the charge displacement should be opposite to the confining force of the electrode potential acting on the surface of electrons. The local currents in different domains (blue arrows) near the domain wall (red dashed circle) flow in the same direction. The domain wall's position is determined by the simple rule:

$$\frac{S_H}{S_L} = \frac{n_e - n_L}{n_H - n_e}. \tag{2.66}$$

Where S_H and S_L are the area of high and low electrons densities, respectively. An asymmetric distribution of surface charges could be made possible by breaking a circular electron pool into a segment and rotating it in the direction determined by the magnetic field.

While the domain wall is sharp, the separation of the charge distributions in the Corbino geometry is stable and the resonant MW excitation will maintain the zero conductivity in the domains. However, if some electrons have been displaced from an area S_L to another region known as S_H, then the conductivity will become positive in both areas and the same amount will return back because of the inner electric field which generated by the separation of the charge. But, the conductivity becomes negative in both areas when electrons have moved from S_H to the area S_L, and the same number of electrons will return back moving uphill. Thus, under the conditions of Eq. (2.66), the domain structure is in a dynamic equilibrium.

Indeed, the formation of the domain resulting from $\sigma_{xx} < 0$, allows us to explain the redistribution of electrons observed under resonant MW radiation[8].

The configuration of the electron density domain provides insight into the self-generated oscillations observed [34]. When the density domain wall's inter-edge profile is uniform, a narrow strip of the domain wall can be responsible for the negative dissipative conductivity, which in turn results in the observed self-generated currents and a negative damping of the inter-edge modes. The same principle applies to edge excitations that travel along the edge of the electron pool when $\sigma_{xx} < 0$ within the edge profile.

The frequencies of both inter-edge magnetoplasmons (IEMP) and boundary displacement waves (BDW) fall within the audio-frequency range, which is comparable to the range previously recorded for self-generated oscillations [34]. As a result, the experimental detection of audio-frequency oscillations can be seen as strong evidence for the simultaneous presence of negative conductivity and a zero resistance state (ZRS) in the neighboring domains.

3. Experimental conditions

Many experiments have been conducted at low temperature to study two-dimensional electrons on the liquid helium surface and in high magnetic fields. Several important findings were made concerning their dynamics under microwave irradiation. A set of data from another experiment is shown in Fig. 3.1. The liquid ^{3}He is condensed into a cell containing a tungsten filament which is heated briefly to produce electrons. The electrons are confined to surface states with a subband that allows them to be excited by microwave radiation, which enters the cell through a pair of sealed windows (full details of the experimental setup are given in [8]. The form of the current, which is measured for short length around 2 sec by the electrodes in the cell (see Fig. 3.1), was quite unusual and not seen before [7].The use of multi-scale analysis methods, reveals oscillations which is clearly seen in the continuous wavelet transform of the time series [9]. The oscillation appears to contain separate amplitude and phase dynamics: the frequency of the oscillations is being modulated by a periodic function but at the same time the amplitude of the oscillations changes non-periodically. Such a mixture of amplitude and phase dynamics would be interpreted as a stochastic system in the frequency domain or phase space (in more details see ref [9] and Sec. 4.3.3). It is only in the time–frequency domain that the dynamics corresponding to a simple non-autonomous oscillator become apparent. From this point, we attempt to answer this question, What is the physics that best describes this behaviour?. Therefore, new set of the experimental introduces here with 5 segmented electrodes to cover all the space of localization of electron on the surface of helium. Also, the data is

measured with longer recordings of the electric currents induced in five Corbino electrodes which will provide in more details below. The longer recording is need because the photo-excited 2D electron gas on superfluid helium is considered as an experimental model of chronotaxic dynamics. Chronotaxic systems, that can sustain stable frequencies in the face of external perturbation [10, 84]. Indeed, our motivations for such Superfluid helium experiments offer an opportunity to create a theoretical understanding of chronotaxic behavior through well-controlled laboratory investigations. The unique properties of superfluid helium, such as its ability to flow without viscosity and to maintain coherence over long distances, make it an ideal system for studying the behavior of non-autonomous systems. By designing experiments that probe the behavior of electron above superfluid helium (under driving system such as MW, pressing voltage) in an open system, it will be possible to establish the links between microscopic behavior and its collective, macroscopic behavior directly. This work could provide insights into the fundamental nature of chronotaxic dynamics and help to establish the characteristics of experimentally-designed open, non-autonomous systems. This research will be among the first to investigate such systems and could have important implications for fields such as quantum mechanics and condensed matter physics.

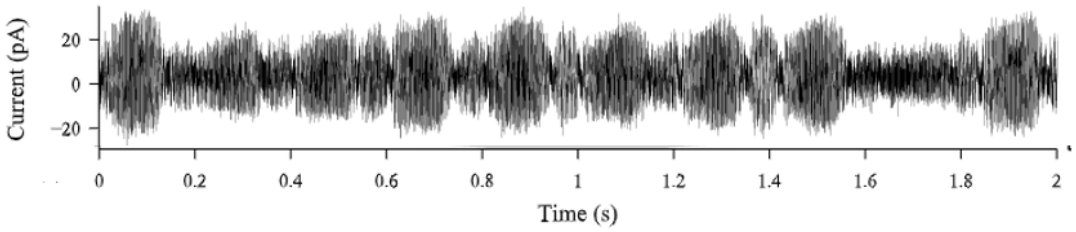

Figure 3.1: Resonant photovoltaic effect in surface state electrons on liquid ^{3}He: Time series of the current recorded by an electrode (full details of the experimental setup are given in Ref. [8], Figure taken from Ref. [9].

This Chapter presents the details of our new experimental setup to explore the spontaneous oscillatory behaviour of the electrons above the surface of liquid helium and, in particular, to establish how it changes as a function of electron density and pressing voltage.

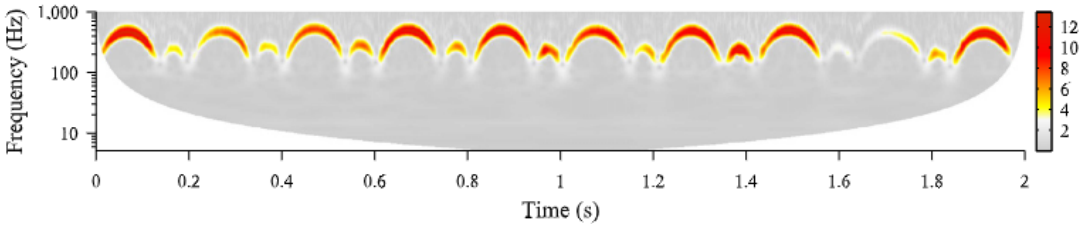

Figure 3.2: Continuous wavelet transform of the time series shown in Fig. 3.1. The calculations used the Morlet wavelet with frequency resolution =5 on the time series sampled at 4410 Hz, Figure taken from Ref. [9] .

3.1 Experimental setup

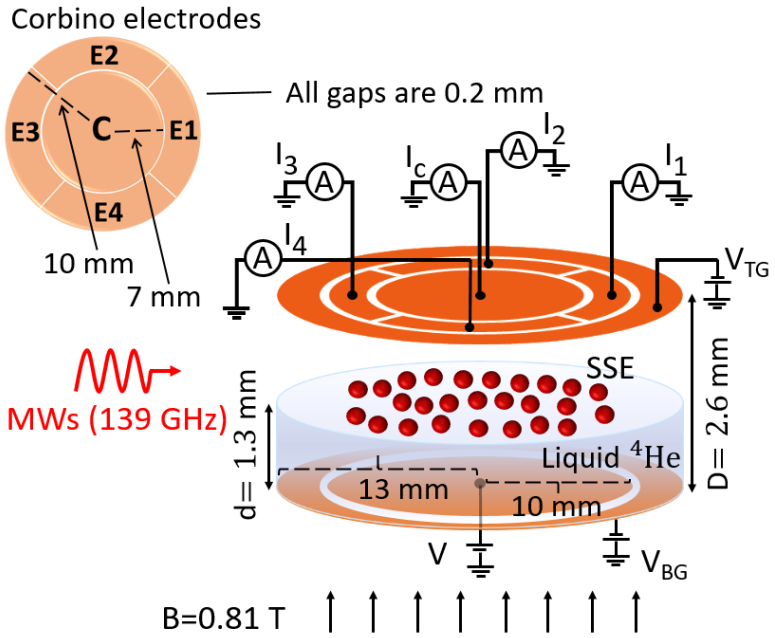

Figure 3.3: Schematic (not to scale) of the experimental arrangement used for investigating the electron gas on the surface of superfluid helium. For detailed description, see text.

Fig. 3.3 illustrates the experimental arrangement. The copper cell is attached to the mixing chamber of a dilution refrigerator at $T \sim 0.3$ K to keep the helium superfluid. After, the sample cell is installed. The white cable which connects the cell with the InSb bolometer is the plastic wave guide for microwave.

The system of electrodes represents a parallel - plate capacitor with two horizontal circular plates of 20 mm diameter, separated by $D = 2.6$ mm, for electron confinement. The separation D between the top and bottom plates is chosen no

less than 2 mm in order to avoid the capillary filling of the whole space between the plates by the liquid helium. The liquid ^{4}He surface is set midway between the plates, so that the helium depth is $d = 1.3$ mm. The helium level is controlled within $\approx 50\,\mu$m by monitoring the capacitance between the top and bottom plates. During the filling process, the sample cell temperature is maintained below 0.3 K, where the vapor pressure of ^{4}He is sufficiently low, in order to avoid shift in liquid level by residual gas condensation on further cooling. Our sample cell contains an array of electrodes for SE confinement (described below).

The capacitance between two of them, upper and lower parallel plates, is used as a sensitive level meter in the cell. We measured the capacitance by a precision meter and adjusted the liquid level to the required position. The setup includes a ^{4}He guide line to introduce helium gas into the cell. Upon introduction of the ^{4}He gas, the cell is cooled and the gas condenses into a liquid.

The depth of liquid helium in the cell can be determined through the capacitance measurement between the upper and lower electrodes. The capacitances between the bottom and the helium surface, C_1, and that between the helium surface and the top, C_2, are

$$C_1 = \epsilon\epsilon_0 \frac{S}{d} \quad C_2 = \epsilon_0 \frac{S}{D-d}, \tag{3.1}$$

where S is the area of the electrodes.The total capacitance between the upper and lower electrodes, $C(d)$, is

$$\frac{1}{C(d)} = \frac{1}{C_1} + \frac{1}{C_2} = \frac{(1-\epsilon)\,d + \epsilon\,D}{\epsilon\,\epsilon_0\,C_0\,D}, \tag{3.2}$$

and $C_0 = \epsilon_0 S/D$ is the capacitance when the cell is not filled with liquid helium. Therefore, the level of the liquid helium can be determined from the relationship $1/C(d) \propto d$. Fig. 3.4 shows an example trace of the capacitance as a function of filled amount of sample gas. The depth d is proportional to the amount of liquid helium in the cell, n and $1/C(x) \propto n$. For instant, the flat region of the

data, ($n < 0.18$ mol) shows that the surface of the liquid helium is below the lower electrode. While, in the linear region ($n_e \geq 0.18$ mol), the surface exists between the two electrodes. The top plate consists of two concentric Corbino electrodes: a

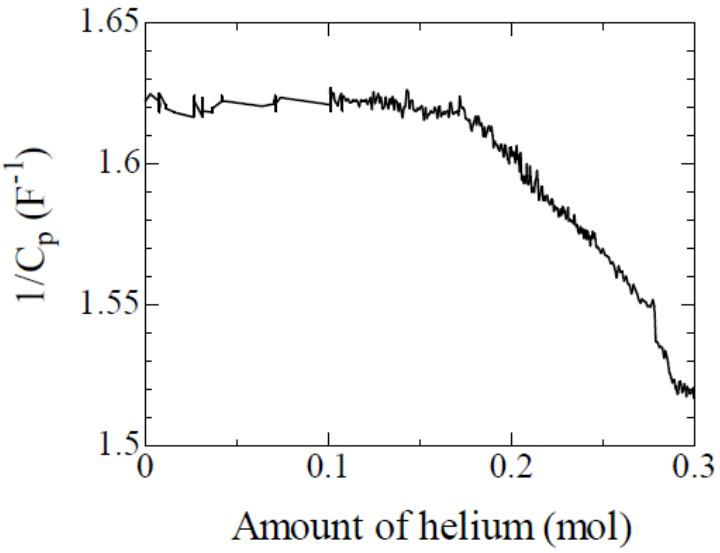

Figure 3.4: The relation between $1/C(x)\left(\mathrm{pF}^{-1}\right)$ and amount of helium n (mol)

central disk C and an outer ring divided into four equal segments E1, E2, E3 and E4. The bottom disk-shaped electrode is positively biased to press the electrons against the helium surface. The top and bottom plates are each surrounded by a negatively-biased guard-ring ($V_{\mathrm{TG}} = V_{\mathrm{BG}} = -0.5$ V) to confine the electrons within their pool.

A pulse of electrons, thermionically emitted from a tungsten filament, attached on the upper electrode as an electron source, accumulates above the liquid surface. A positive potential V on the bottom electrode controls the electron density n_e. This can provide a neutralizing background and counteracts the Coulomb repulsion between electrons and prevents them from spreading its away. Indeed, electrons are trapped on the surface until they compensate the holding electric field above the surface and the saturation condition is achieved when the electric field between the top and bottom electrodes is zero.

An electric field is generated by two parallel electrodes of a capacitor. This field is referred to as a holding field which gives a correction $eE_{\perp}z$ to $V(z)$. A holding

field is also used to determine the electron density on the liquid helium surface, where such electrons are called surface-state electrons (SSE) [85].

The electric field between the surface of electrons and the lower electrode is strong, while the field between the upper electrode and the surface of electrons is nonexistent. The electric charge density σ is related to the electric field E under Gauss's law as

$$\epsilon_0 \int \boldsymbol{E} \cdot \boldsymbol{n} dS = \sigma S. \tag{3.3}$$

Here n is the unit vector perpendicular to the surface and S is the total area covered by electrons. Hence

$$-\epsilon_0 \epsilon_{He} E_\perp = \sigma = -n_{sat} e. \tag{3.4}$$

The electric field is expressed by pressing voltage applied to the bottom electrode, V and the distance between the lower electrode and SSEs, d by

$$E_\perp = \frac{V}{d}, \tag{3.5}$$

where V is a pressing voltage applied to the lower electrode and d is the distance between the lower electrode and the surface of electrons. The saturated electron density is

$$n_{sat} = \frac{\epsilon_0 \epsilon_{He} V}{ed}. \tag{3.6}$$

Where ϵ_{He} and ϵ_0 are the helium dielectric constant and the vacuum permittivity, respectively, and e is the electronic charge. In our experiment, n_e is varied from 1–$2.5 \times 10^6\,\mathrm{cm}^{-2}$. The surface of liquid helium is usually assumed to be flat, but it can also be deformed freely. This phenomenon was observed by Williams and Crandall [16]. When electrons are attracted by the holding field to the surface, they can cause it to become depressed. The limit of the electron density above helium due to the surface deformation is caused by the holding field.

The surface state electrons are exposed to a perpendicular magnetic field

and resonant microwaves propagate parallel to the helium surface with frequency $\omega_{12}/2\pi = 139$ GHz, and power 0 dBm to excite an intersubband transition between ground and first excited surface states. The input MW power controlled by attenuator in the range 1–100 μW was introduced into the cryostat through a waveguide system having a total power loss of about -10 dB. The power output of the MW source strongly depends on the MW frequency. Therefore, in the experiment, the frequency of MW radiation is fixed and tuned to an intersubband transition between the ground and first excited surface states.

Note that, there is evidence for some temperature-dependence of the energy levels [20, 86]. The temperature increase of liquid helium due to MW, which was measured in earlier experiments of the same group, was 1% at a maximum power [33]. It was also shown that ripplon distribution does not get significant influence while electron temperature can be even 10 K. In the present work, the fridge temperature was kept constant at $\sim$ 0.3K, and it is reasonable to assume that the effective temperature of the cell was constant, thus making the temperature effect less severe. However, there is clearly a scope for future research exploring thermal influence on the magnetoplasmon-ripplon interaction. Because the transport involves ripplon scattering, zero-resistance states, electron-electron interaction, and intersubband scattering [87], the theory is likely to be challenging. The intersubband resonance condition is tuned by adjustment of V to change the gap between the two lowest surface bound states due to the Stark effect. The vertical magnetic field is set to a value $B = 0.8$ T, where one of the ω/ω_c relationship is fulfilled.

The microwaves are activated for ≈ 47 seconds. Current signals I_c, I_1, I_2, I_3 and I_4 are measured simultaneously from electrodes C, E1, E2, E3 and E4, respectively. They are converted to voltage signals by current preamplifiers with a gain 10^{-9} A/V and a frequency bandwidth 10 kHz. The pressing voltage is set to a value $4.16 < V < 4.22$ V with an electron density of either $n_e = 1.4 \times 10^6$ or n_e=2.2×10^6 cm^{-2}. The signals are sampled for 60 s with a sampling frequency of 100 kHz. The microwaves are switched on 6 s after the start of recording and switched off 7 s

before the end.

The induced charge due to vertical surface motion in the geometry of Fig. 3.3. Suppose the equilibrium 2D electron number density is n_0, corresponding to the electric field E_0 by $n_0 e/\epsilon = 2E_0$ (Gauss' theorem), where ϵ is the dielectric constant of vapor and liquid ^{4}He and e is the elementary charge. For now, we ignore the sign and the difference of ϵ between vapor and liquid, The vertical displacement of the surface $\xi(x, y)$ ($|\xi| \ll D$) induces a change of electron number density in the detector electrode

$$\delta n_1 = n_0 \frac{\xi}{D} = \frac{2\epsilon E_0}{e} \frac{\xi}{D}. \tag{3.7}$$

For the parallel contribution, note that the capacitance per unit area of 2D electrons is twice ϵ/d, so that

$$C = \frac{4\epsilon}{D}. \tag{3.8}$$

The surface displacement induces a potential variation $\delta\phi = E_t\xi$ along the surface, where E_t is the total vertical electric field ($E_t > E_0$), which presses the electrons to the surface and tunes the vertical resonance. Accordingly, the charge density variation on the surface is $e\delta n = C\delta\phi$, and the charge variation induced on the electrode δn_2 is a half of it, so that

$$\delta n_2 = \frac{2\epsilon E_t}{e} \frac{\xi}{D}. \tag{3.9}$$

Thus the two contributions are on the same order of magnitude, but the magnitude of the latter is larger in general. The contributions δn_1 and δn_2 have opposite sign, and for $E_0 = E_t$ condition, they cancel.

We apply time-resolved, nonautonomous, nonlinear dynamics methods to extract a wealth of information from the experimental data. This method provides temporal resolution and yields information about localized waves.

4. Dynamical systems and methods for analysing them

This chapter comprises three main sections. The first presents the theoretical background for dynamical systems, in particular for nonautonomous systems. Sec. 4.3 provides a review of the inverse approach to dynamical systems. The statistical tests used in our analyses are described in Sec. 4.4. Methods for the detection of chronotaxic systems via the inverse approach are then reviewed in Sec. 4.5

4.1 Introduction

In order to gain a deeper understanding of the underlying dynamics of any given system, one can apply various treatments to analyse the data it produces. Such data, recorded from the system, can be analysed by using procedures that enable its oscillatory dynamics to be times resolved, thereby extracting a wealth of information from the data such as their statistical properties. One can also investigate the system's potential oscillatory characteristics. The algorithms use the amplitude and power of oscillations, and their phase characteristics, rather than only amplitudes. The latter are more vulnerable to artifacts and noise. Moreover, the algorithms in question take into account the varying frequencies and phases of the signals as well.

Physical systems whose parameters vary in time (t), termed "dynamical sys-

tems", can be described by the equation:

$$\frac{\mathrm{d}x}{\mathrm{d}t} = f(x), \tag{4.1}$$

where f is some function acting on the previous state of x; f describes the infinitesimal change in the state x, (where x is the state of a system) in an infinitesimal time interval t. This differential Eq. (4.1) describes the progress of systems with continuous time. In cases when time is discrete, iterated maps can be used [88]. There are a variety of systems that are related to the concept of dynamical systems, for example the linear harmonic oscillator, the planetary system, and the simple pendulum. However, dynamical systems that explicitly depend on time are referred as *nonautonomous*. The simplest case can be described mathematically by the differential equation:

$$\frac{\mathrm{d}x}{\mathrm{d}t} = f(x, t). \tag{4.2}$$

In general, systems can be categorized into being linear or nonlinear. Linear systems are relatively easy to solve, and they exhibit much simpler properties than nonlinear systems. The output evolution of a linear system is exactly proportional to evolution of the input. In contrast, in nonlinear systems, such a proportionality does not exist. Most open systems are nonlinearly dynamical [89], making them difficult to analyze.

Physical systems whose parameters vary in time are called “dynamical systems”. Electrons above liquid helium in the presence of a perpendicular magnetic field and exposed to microwave radiation provide a good example of such a system. There exists an external mechanism (such as the microwave-electron interaction) which allows the system to exchange energy with its surroundings, resulting in an inherent time-variability and high nonlinearity. We need suitable analysis methods to acquire insight into the behavior of the system generating the data. Thus, we aim to use nonlinear dynamical methods to extract information about time-varying

oscillatory modes and their mutual interactions. In addition, a nonlinear system may display self-sustained oscillations. That can be represented in the system's phase space by a stable limit cycle. A limit cycle is a closed trajectory: neighboring trajectories may spiral towards it or away from it, depending on its stability.

.

4.2 Stochastic and deterministic systems

A fluctuation is referred to as a noisy or stochastic event when the suspected origin of the phenomenon involves the actions of a large number of variables or degrees of freedom. Thus, complex behavior can be caused by the effects of external random influences on a system. This can be modeled by adding a noise term to the equations describing the time-series of a system. The characteristics of the noise in the system are completely different from the characteristics of the system's internal dynamics. Such stochastic systems can therefore be treated as open.

A deterministic system is defined by differential equations which describe its evolution in time. It does not incorporate random elements in the prediction of its future. Such deterministic systems are in marked contrast to the stochastic ones. The latter are probabilistic so that system's evolution cannot be predicted with certainty. For a deterministic system, where the initial state of the system is known at a given point in time, we can infer the events that happen in the system without any uncertainty at all.

4.3 Inverse approach to dynamical systems

A more realistic framework for describing many real-world situations of the system is in terms of non-autonomous differential equations. Due to the complexity of their analysis, many such attempts have been unsuccessful. Phase space analysis is a crucial step in the process of implementing a deterministic description. It is usually performed to reconstruct the attractor in phase space. This method works well for

autonomous systems that do not explicitly depend on time, but does not consider time-dependent attractors [90]. To solve the problem of the time-dependence of these systems, additional dimensions are required in phase space. This adds complexity to the problem. The inverse problems approach is useful in solving dynamical systems. It can be used to make direct measurements of the system or to model it using a set of differential equations. The only difference between the two approaches is that, in the first, the data is the source of limitation while, in the second, the limitation appears from the approximations and simplifications of the model. Many signal analysis methods assume that the frequency distribution of the data is constant. However, this is not the case in nonautonomous systems. Nonstationarity is a feature that defines complex data. Statistically, nonstationarity is exhibited as a change either in the time series mean, or its variance, or both [91]. A common method of visualizing the dynamical properties of the time series generated by a system is to define its frequency spectrum. The discrete Fourier transform (DFT) is one of the traditional methods applied to analyse time traces. However, application of the DFT to nonstationary time series will produce blurred or misleading power spectra. This limits its usefulness: computation of the power spectral density commonly yields a "$1/f$" spectrum and crucial information is lost. Windowing methods have been used, such as the windowed Fourier transform (WFT) and the wavelet transform (WT), that are successful when applied to time traces analysis. The former suffers from limitations due to the fixed window size that badly limit the usefulness of the method in the analysis of slow oscillations, while the latter provides a solution of that limitation by introducing an adaptive window size [92]. Simultaneous visualization of the whole time-frequency representations of a signal is extremely useful in observing the dynamical features of the system and their time evolution.

As a result, progress in the development of wavelet-based methods for the treatment of nonautonomous dynamics is now very active [9], including methods for finding harmonics [93], extracting modes [11], and calculating wavelet phase coher-

ence [94] and wavelet bispectra [95] as well as the application of dynamical Bayesian inference [96]. For our system of electrons on liquid helium, current recordings from electrodes at distinct radial and axial positions need to be investigated, using techniques for the analysis of non-stationary and time-varying non-autonomous dynamics, in order to provide insight into the spatial and temporal nature of the interactions underlying their dynamics.

4.3.1 Time-domain

A signal measured from a physical system can be represented in the time-domain (time traces) as a starting point. However, the dynamical properties of nonautonomous systems are concealed inside the data and this makes it hard to visualize them in time-domain representations. In order to discern the dynamics of the time series, other methods are required. These include analyzing the variability of the frequencies and amplitudes of oscillations within the time series.

4.3.2 Preprocessing

Before analysing the physical system and using other ways of representation, preprocessing of its the time series is required to provide optimal conditions for the analysis. In time traces recorded from physical systems, artefacts may appear due to movements, missed measurements, or any non-physical influence. Therefore, the data are detrended to remove non-oscillatory trends from the original data by subtracting a best-fit cubic polynomial. Non-oscillatory trends appear as low-frequency variations of the signals, and the purpose of detrending is to remove their possible interference with low-frequency oscillatory modes within the range of interest. The detrending can be achieved by using a moving average method, in which a window moved along the data. This window has a defined width in time, and the central value is set to the mean of that window. This method is usually utilised for smoothing signals, depending on the size of the window used with the data. It is usually necessary to subtract the average of the data when doing

frequency, or time-frequency analysis. Down-sampling may be used for effectively reducing the initial sampling rate of the data. In the present case, the sampling frequency was 100 kHz, which gives a higher resolution than is needed, so all the signals were down-sampled to 10 kHz

4.3.3 Frequency-domain

Before performing a signal analysis in the frequency domain, it is important to consider the characteristics of the data. The data measured as time traces of any physical system can be represented in both the time and frequency domains. In the former, data are represented as a function of time $F(t)$, while in the latter they are shown as the distribution of the system's dynamics in the frequency domain. The maximum frequency that can be observed in the signal equals half the sampling frequency (f_s) used to measure the data, defined as the Nyquist frequency. The time between two successive measurements is equal to the reciprocal of the sampling frequency, $\Delta t = 1/f_s$. The lowest observable frequency depends on the length of the data (L); $f_{min} = 1/L$. Therefore, the data must be longer than one period of oscillation and one also cannot distinguish between two oscillations if the difference in their frequencies is less than the lowest frequency. One of the commonest ways to visualize the dynamics of a signal is to represent it in the frequency domain, which allows one to observe how its oscillations and changes are distributed over a perhaps wide range of wavelengths.

The Fourier transform

In physics, a physical process can be represented in either the time domain or the frequency domain. The time domain representation describes the values of a quantity f, such as a signal, as a function of time, typically denoted as $f(t)$. On the other hand, the frequency domain representation describes the amplitude of the process F as a function of frequency, usually represented as $F(f)$. Each of these representations of the same function will provide a different kind of information.

When the time is measured in seconds, the unit of frequency is often measured in Hertz (Hz), which is equivalent to the number of cycles per second. The discrete Fourier transform is a method that can be used to analyze signals. It is usually first considered using Fourier series. The Fourier series of a periodic function can be expressed as an infinite series of sines and cosines,

$$F(t) = a_0 + \sum_{\omega=1}^{\infty} [a_\omega \cos(\omega t) + b_\omega \sin(\omega t)], \tag{4.3}$$

where ω represents the angular frequency and a_0, a_w, and b_w are constants known as Fourier coefficients. The values of these coefficients depend on the shape of the function, $F(t)$, with the largest values corresponding to components (modes) in the signal that have stationary frequencies.

Signals representing variables measured from physical systems (e.g.electrons on the surface of liquid helium) usually involve discrete sampling. For the basis described above, the DFT of a signal $F(n)$ can be defined as:

$$F(\omega) = \sum_{n=0}^{N-1} F(n) e^{-\frac{2\pi i \omega n}{N}}. \tag{4.4}$$

The equation above can transform a signal from the time domain to its frequency domain representation. The Fourier transform exhibits peaks at the frequencies of the time series. The Fourier transform is symmetric in the range $0 \leq \omega \leq N-1$. For real-valued signals, the transform is reflected in the point $\omega = N/2$, with coefficients corresponding to positive frequencies for $\omega < N/2$ and the negative frequencies coefficients corresponding to $\omega > N/2$. The negative-frequency coefficients are usually not presented in the final plot.

The Fourier transform is thus a mathematical technique that is used to decompose a signal into its frequency components. It assumes that the signal on which it is performed is stationary, meaning that the frequency components do not change over time. However, this is not the case for data recorded from our system of interest (the 2D system of electron on the free surface of liquid helium in the

presence of a magnetic field directed normally and exposed to microwave radiation) where there are changes in the frequency components over time. Furthermore, due to an instability, the system enters a nonlinear regime. If the time variation is deterministic, it may not be distinguishable from random variations in the basic Fourier transform. Indeed, the Fourier transform uses sinusoidal functions as a basis for decomposing a signal into its frequency components. This can be problematic for signals that have irregular or non-sinusoidal oscillations as the sinusoidal basis may not accurately represent the shape of the signal.

Power spectral density

The commonest method of visualizing the dynamical properties of a signal is the Fourier transform (frequency domain) as explained in Sec. 4.3.3. The term "$1/f$ noise" refers to the shape of the spectral density, $P(f)$, of a stochastic process having the form

$$P(f) = \frac{\text{constant}}{f^{\alpha}}, \tag{4.5}$$

where $\alpha \geq 0$ and determines the functional dependence of the spectrum. Taking the logarithm of each side of Eq. (4.5), we obtain

$$\log(P) = \log(\text{constant}/f^{\alpha}) = -\alpha \log(f) + \log(\text{constant}), \tag{4.6}$$

where α is a parameter that is computed from the gradient of the straight line graph. Fig. 4.7 (c) shows the power spectral density of the time trace of signal.

Our computations for all data yield an α value in the range $-1 \leq \alpha \leq 0.9$, leading to the spectral density commonly referred to as "$1/f$" noise [97]. For systems that are nonautonomous, a representation in the frequency domain is insufficient to represent all the information that is contained in the signal. $1/f$ noise is characterized by a power spectral density that increases as the frequency decreases, but it does not provide information about how the noise changes over

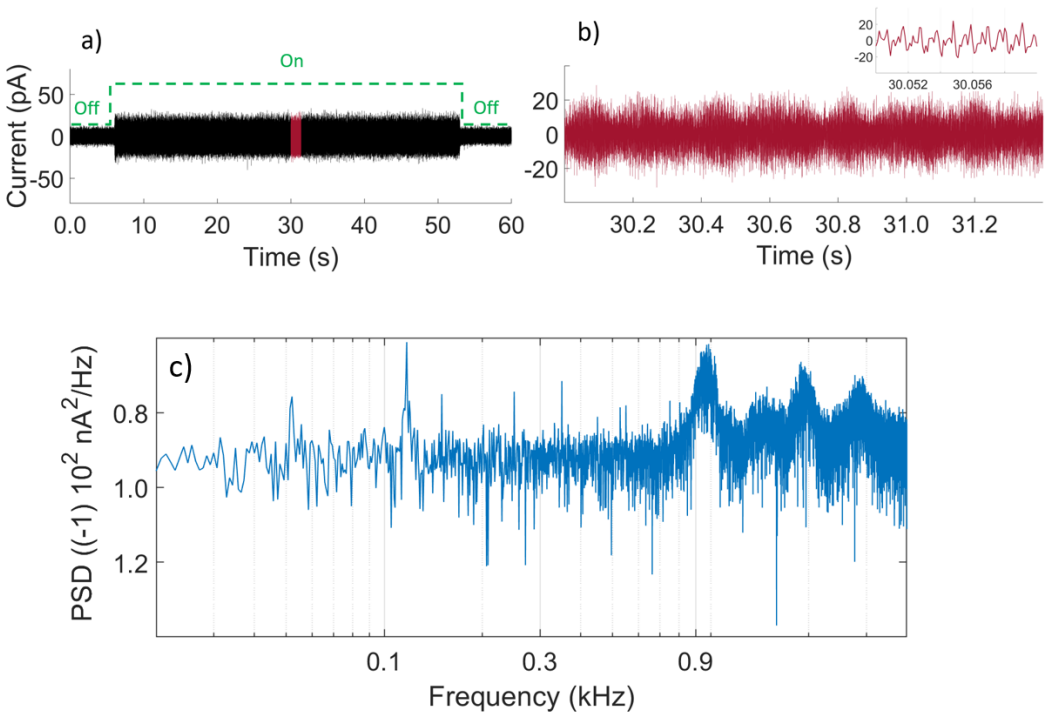

Figure 4.1: (a) Example of a full-length of time series recorded for 60 seconds at a sampling frequency of 100 kHz resampled to 10 kHz. The MW (139 GHz) is switched On and Off where the On state is inside the green dashed lines. (b) The section of the signal in red, recorded for 1.4 seconds, is investigated to elucidate the characteristics of the oscillations. The inset shows the current oscillations within a shorter time interval. (c) Example of power spectral density (PSD) of the time series of electron on the surface of liquid helium. The sampling frequency is 10 kHz. The spectrum contains peaks at frequencies 0.17, 0.95, 1.94 and 2.9 kHz.

time. Nonautonomous systems, in contrast, are characterized by a time-varying behavior, for example, the behavior of a system can change with time due to external inputs or internal dynamics. Therefore, to fully understand the behavior of nonautonomous systems, it is important to consider both the frequency content of the signal and the way that content changes over time.

Indeed, the PSD can be used to identify the frequency content of a signal, including the amplitude of each frequency component, but it does not provide information about the phase relationships between the frequency components. Also, such a representation has no physical relevance to any mechanism of frequency modulation.

4.3.4 Time-frequency analysis

Short time Fourier transform

The Short Time Fourier Transform (STFT) or Windowed Fourier Transform (WFT) goes some way to solve the problems with the Fourier transform and power spectral density. The Short Time Fourier Transform (STFT) can overcome limitations of the Fourier transform when used to analyze the nonstationary signals [92], and to create time-frequency representations of the signals. The STFT works with a time series $x(u)$ of length T, by sliding a rectangular function of length $\tau < T$ (window) over the signal. Within the window, the signal can be treated as stationary and the Fourier transform (FT) can usefully be applied. However, the STFT method still has limitations because of a trade-off between time localisation and frequency resolution, due to the uncertainty principle, which states that we cannot determine the precise frequency and the exact time simultaneously [92]. Therefore, the size of the window is adjusted depending on whether the user needs good frequency resolution or good time localisation. By using a large window we can obtain good frequency resolution but poor time localisation: the frequency resolution is proportional to the length of the window. Also, the linear frequency resolution of the STFT gives poor performance in resolving separate oscillatory modes when analyzing low frequency components in data.

Continuous wavelet transform

The wavelet transform (WT) was developed to overcome limitations of the WFT. Therefore, the wavelet transform is the optimal solution which simultaneously examines the signal in time and frequency. It makes use of an adaptive window that yields good frequency resolution and time-localization with logarithmic frequency resolution. Indeed, the wavelet scale is inversely proportional to time localization and directly proportional to frequency resolution. Thus, the size of the window is large when dealing with slow oscillations and a small window size is used when

dealing with very fast oscillations, which is known as an adaptive window. The wavelet transform is obtained from [44],

$$g(s,t) = \frac{1}{\sqrt{s}} \int_{-\infty}^{\infty} \psi \left(\frac{u-t}{s} \right) g(u) du, \tag{4.7}$$

where s is a scaling factor, t is a location on the signal in time and ψ is function. The wavelet transform is calculated by moving a wavelet function along the signal and it can be tuned according to the frequency ranges that we want to investigate [9].

If the data and the wavelet basis are a good match, then the value that calculated from their convolution will be large. In this way, a time-frequency representation of the whole signal can be generated by plotting time, frequency and amplitude on a three-dimensional graph. The wavelet power spectrum can be found by calculating the integration of the square of the wavelet transform modulus over frequency [9, 44]

$$P_W(\omega, t) = \int_{\omega - \frac{d\omega}{2}}^{\omega + \frac{d\omega}{2}} |W_T(\omega, t)|^2 d\omega. \tag{4.8}$$

This will produce a vector representing the power of the whole-time series, which can be plotted versus frequency to be used to compare power spectra between different signals. This provides a good starting point in the analysis since it can be used to identify the frequency range of the main oscillatory components in the signal under investigation.

Wavelet types

There are many types of wavelets, each with its own specific applications. Complex wavelets, e.g. the Morlet wavelet, are useful because they allow the separation of the amplitude and phase components of a signal. With our data, the Morlet wavelet was used in all analyses. The Morlet wavelet is a complex wave within a

Gaussian envelope that has unit standard deviation

$$\psi(u) = \frac{1}{\sqrt[4]{\pi}} e^{i2\pi f_0 u} e^{-u^2/2}. \tag{4.9}$$

The parameter f_0 is the frequency resolution, which determines the trade-off between time localisation and frequency resolution in the wavelet coefficients calculated from the signal under study. Higher values of f_0 give lower time resolution, but have good frequency resolution. However, at very small frequencies the wavelet becomes meaningless.

Coefficients from performing a WT with the Morlet wavelet can be complex-valued. This property can be used to determine the instantaneous amplitude and phase for each frequency and time [98].

4.3.5 Cone of influence

The wavelet transform integrates over infinite time, while the real signal has finite length. Then, the WT near the time borders becomes ill-defined. This happens close to $t = 0$ or when t approaches the end of the signal. To overcome this limitation, signal padding may be used: it makes the signal longer at its start and finish during computation of the wavelet transform; and then the added regions are removed to retain only the original interval. Various types of padding regime are used. These include zero padding, predictive padding, and periodic padding [43]. Although the WT is calculated at the boarders of original data, a boundary effect is still observed even after padding. The portion of the wavelet transform which is not affected is referred to as the cone-of-influence.

Thus, the wavelet transform is a time-frequency method which, in combination with Morlet wavelet and within the Heisenberg uncertainty principle, provides the optimum between time and frequency resolution. In this study, the frequency resolution value that gave an optimal trade-off was 3 Hz.

4.3.6 Ridge curve extraction

Ridge curve extraction is an approach for extracting the oscillatory modes or the trace of a time-varying frequency from the time-frequency representations of the data [11, 99]. The oscillatory components are shown as amplitude/power peaks in the time frequency representation. The oscillatory components with their corresponding frequencies can be visualized by using both the time-frequency representation and the time-averaged power plot as shown in Fig. 4.2. The ridge

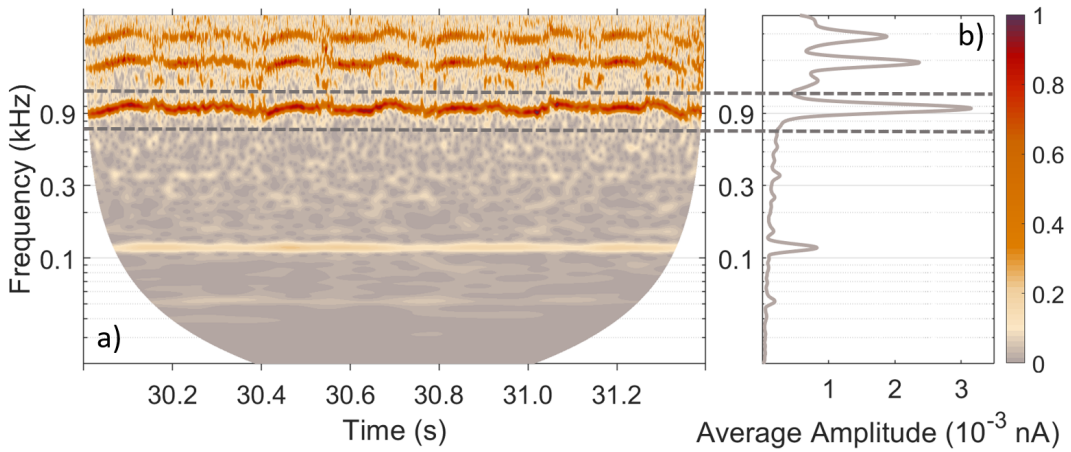

Figure 4.2: (a) Time-frequency representation (TFR) and (b) average amplitude plot of the set signal presented in Fig. 4.7 (b). Oscillatory components are shown as amplitude peaks in the TFR and average amplitude plot. The frequency band chosen for ridge extraction include the entirety of the oscillatory components (limits shown by the grey dashed lines). The colour-coding scale displays wavelet amplitude.

extraction can be defined by selecting the frequency band which includes the entirety of the oscillatory components within the signal. The frequency band should include the whole width of the oscillatory component, including the peak and the surrounding blur due to the uncertainty principle. For accurate results, we should aim to extract only one oscillatory component from this frequency band. Indeed, the frequency band for each mode in the spectrum was selected by using the time-frequency representation and the average amplitude spectrum. Minima in Finteractionsthe amplitude spectrum were then used to start setting the boundaries between the various oscillatory components; then, based on the time-frequency

representation, boundaries were adjusted to ensure that overlapping of oscillatory components would not occur, as shown in Fig. 4.2. This figure provides an example of the boundaries selected for the ridge extraction. The ridge curve is a method that shows the maximum amplitude peaks that can be expected in the time-frequency space within which the frequency interval is specified.

4.3.7 Harmonic detection

The wavelet transform (WT) is applied to the signal in order to trace the time variability of the fundamental oscillation frequencies and to obtain time-dependent phase information. The oscillatory components extracted from the time-frequency representation are often in harmonic relationships. In other words, the instantaneous frequency of one oscillation is a multiple of the instantaneous frequencies of another one at all times. A harmonic occurs when a single oscillator has a nonsinusoidal wave shape and is represented by integer multiple oscillatory components of the fundamental frequency. Thus, high frequency harmonics are expected in the data due to the nonlinearity of the measured signal. Understanding the various harmonic relationships is very important to identify the number of basic oscillators, or components that describe the system. Initially, a visual harmonic test can be performed by comparing the extracted ridges. Also, the ridge shapes can be examined: if the frequency components are in a harmonic relationship, their ridges should have almost identical shapes. A harmonic relationship can be established by determining if the components of an oscillatory system consistently exist in a rational relationship over time. An accurate method was developed by Sheppard et al. [93], for finding a harmonic relationships between various oscillatory components where there are time-varying frequencies and amplitudes, using wavelets to analyze the signal. The method can determine whether an oscillation is a harmonic of the main frequency in the signal or an independent higher-frequency oscillation. This method of finding harmonics is based on a mutual information analogy with the Shannon entropy and surrogate testing. The mutual information (M) provides a

measure of the entropy missing from a conditional distribution while considering information about another variable. The Shannon entropy introduces a measure of the unpredictability. The entropy is high if the distribution is uniform, and it is low if the distributions are sharply peaked.

Procedure for identifying harmonics: First, we need to extract phases from the wavelet transform at each point in time for each frequency in the signal where ϕ_1 and ϕ_2 represent the phases of the main frequency and the high harmonic of the main frequency, respectively. The phase time series are compared in pairs. The Shannon entropy of the phase distribution $p(\phi_1)$ of the higher-frequency component is calculated for each pair, and then the mean entropy of the distribution is determined for each moment in time $p(\phi_1\|\phi_2)$, given the corresponding phase of the lower-frequency component. Then the phases are discretized into 24 bins. These phases are obtained in order to calculate the mutual information. The mutual information is calculated for every possible pair of phases in the signal. The entropy of the 24 phases discretized is given by

$$H(\Phi_1) = -\sum_{\phi_1=1}^{24} p(\phi_1) \log_2 p(\phi_1). \tag{4.10}$$

The mean entropy of the conditional distribution is calculated using the equation

$$H(\Phi_1||\Phi_2) = -\sum_{\phi_2=1}^{24} p(\phi_2) \sum_{\phi_1=1}^{24} p(\phi_1||\phi_2) \log_2 p(\phi_1||\phi_2). \tag{4.11}$$

The mutual information of the data is calculated by the difference between Eqs. (4.10) and (4.11),

$$M(\Phi_1, \Phi_2) = H(\Phi_1) - H(\Phi_1||\Phi_2). \tag{4.12}$$

The two frequencies ω_1 and ω_2 of the phases are approaching each other as the proportion of the mutual information for $\phi(\omega_1, t)$ and $\phi(\omega_2, t)$ approaches 1. Since the mutual information is biased by the correlation of the phase signal caused by

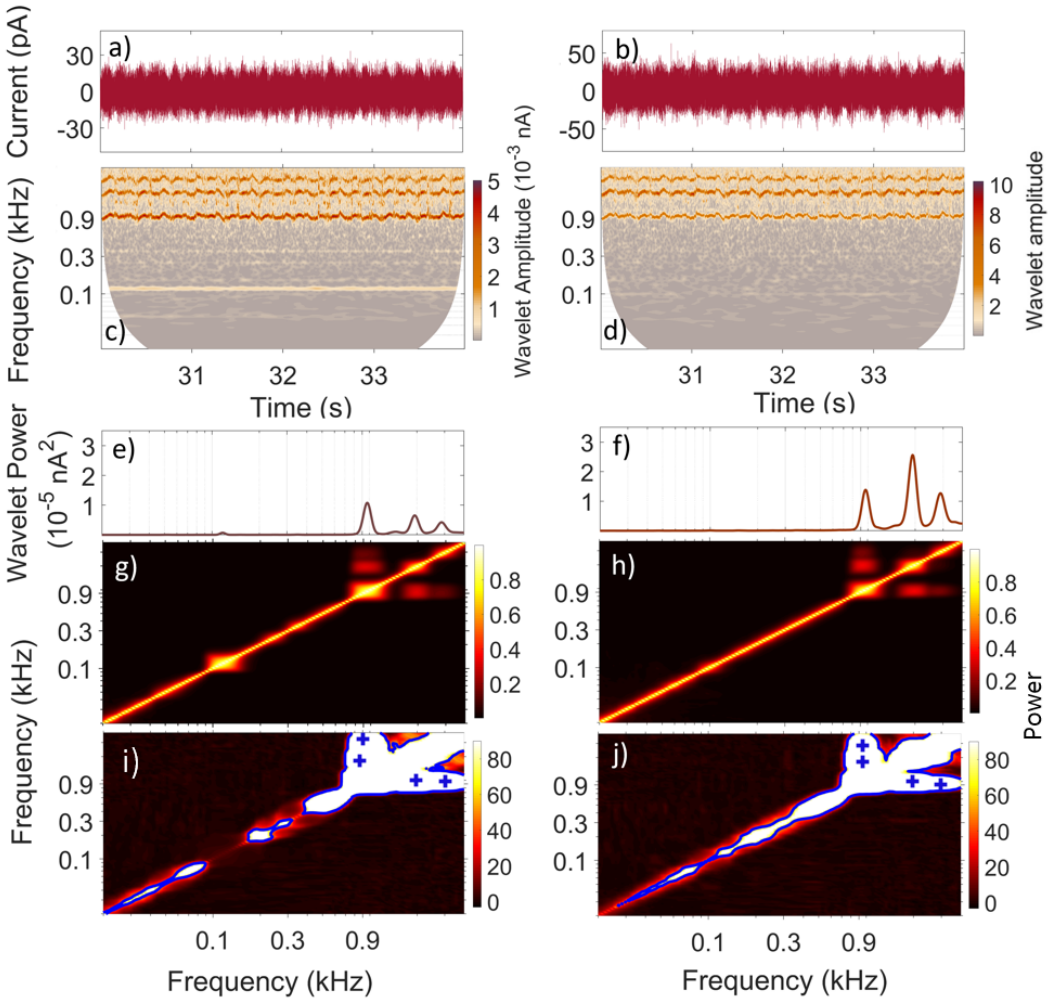

Figure 4.3: (a-b) Current signal for electrodes (2,3) (4 s sections) recorded for 60 seconds, pressing voltage 4.20 V, $B = 0.81$ T and $n_e = 1.4 \times 10^6$ cm^{-2}. (c-d) Wavelet transforms with frequency resolution 4 Hz showing the mean frequency of the main mode of each signal being around 951 Hz where the frequencies of second and third harmonics are 1884 and 2886 Hz, respectively. (e-f) time-averaged wavelet power of the signals in (a-b) showing the fundamental frequency and higher harmonic oscillations. The z-axes in panels (c-d) represents the wavelet amplitude; the y-axis of (b) and the x-axis of (e-f) are on logarithmic scales. (g-h) the corresponding the mutual information M plot. (i-j) shows the actual mutual information values relative to the surrogate distribution, which we will refer to as an M-plot. The threshold of standard deviations above the mean of the 100 surrogate distribution is marked in blue, and local maxima are marked with +. High harmonics appears in the representation due to nonlinearity. The central frequency used in calculations is 1 Hz.

binning, it is necessary to perform surrogate testing [100]. Surrogates are signals that are designed to preserve all of the properties of the original signals, except the property relating to the hypothesis that is being tested. The commonly used

methods to generate surrogates are the amplitude adjusted Fourier transform (AAFT) and the iterative amplitude adjusted Fourier transform (IAAFT). The methods conserve the amplitude distribution in real space and produce again the power spectrum (PS) of the original signals. The basic assumption of (AAFT) and (IAAFT) is that higher-order correlations can be destroyed by randomization of Fourier phases in time while preserving the linear correlations [101]. A local maximum in the values of the mutual information calculated for a pair of phases from the original data is deemed to indicate a harmonic if it occurs some number of standard deviations above the mean value of the surrogate's mutual information.

Figures 4.3 (a) and (b) show 4-second sections of the current signals from the 60 second measurements by electrodes E2 and E3. The measurements are taken simultaneously with a sampling frequency of 100 kHz, resampled to 10 kHz, and with a pressing voltage of 4.20 V, $B = 0.81$ T, and with $n_e = 1.4\times10^6$ cm^{-2}. The time frequency representation (WT) and the time-averaged wavelet power are presented in Fig. 4.3 (c,d) and Fig. 4.3 (e,f) for electrodes E2 and E3, respectively, with a frequency resolution of 3 Hz. The E2 and E3 signals oscillate at the same frequency, the mean frequency of the main mode of each signal being around 951 Hz where the second and third frequencies are 1884 and 2886 Hz, respectively, as shown in Fig. 4.3 (c). It appears from the identical frequencies that E2 and the E3 are coupled. We have calculated the coherence of the two signals, and found that they are coherent in the frequency range of the oscillatory modes: see also below.

To determine whether the second and third harmonics of the signals from E2 and E3 are independent modes, or higher harmonics of the fundamental mode, the harmonic finder method is used (see above). Fig. 4.3 (g,i) for E2, Fig. 4.3 (h,j) for E3 show the mutual information plot relative to the mean and standard deviation of the surrogates. A threshold of standard deviations above the mean of the 100 - surrogate distribution is marked in blue. High harmonics appear in the representation due to nonlinearity in both set of data. It was found that the second and third frequencies for each electrode (E2,E3) are higher harmonics of the

main mode, which results from a strong nonlinearity generated by the interaction between the liquid helium surface and the motion of the electrons.

Examining the harmonic relationships within a system is a key step in determining the number of fundamental oscillators, or modes, that define the system. By establishing these unique oscillators, it becomes possible to study and understand the underlying cause of their oscillation.

4.3.8 Interactions

Phase coherence and phase difference.

The wavelet phase coherence approach determines the relationship between phases from two signals over time, at each frequency of interest [45, 94, 102, 103, 104]. If oscillations are observed at the same frequency in two different time series, and the difference between their instantaneous phases $\phi_{1k,n}$, $\phi_{2k,n}$ is constant, then we can say that the oscillations are coherent at that frequency. The wavelet phase coherence (WPC) between the two signals $x_1(t)$ and $x_2(t)$ is obtained through their respective wavelet transforms as defined by Eq. 4.7. W_{si} is the wavelet transform of signal x_i. The WPC of the two signals [94] is given by

$$WPC_{x_1;x_2}(f) = \frac{1}{L}\int_o^L e^{iarg[W_{x_1}(s,t)W^*_{x2}(s,t)]}dt|, \tag{4.13}$$

where the scale s is related to the frequency f by $s = 1/(2\pi f)$. The phase coherence function $C_\theta(fk)$ is obtained by computing and averaging over time the sine and cosine components of the phase differences for the whole signal, effectively defining the time-averaged WPC as

$$C_\theta(\omega_k) = \sqrt{\langle\cos\Delta\theta_{kn}\rangle^2 + \langle\sin\Delta\theta_{kn}\rangle^2}. \tag{4.14}$$

The phase coherence function $C_\theta(fk)$ as defined in equation (4.14) is exactly the discrete version of the phase coherence formula in equation (4.13). In addition, we

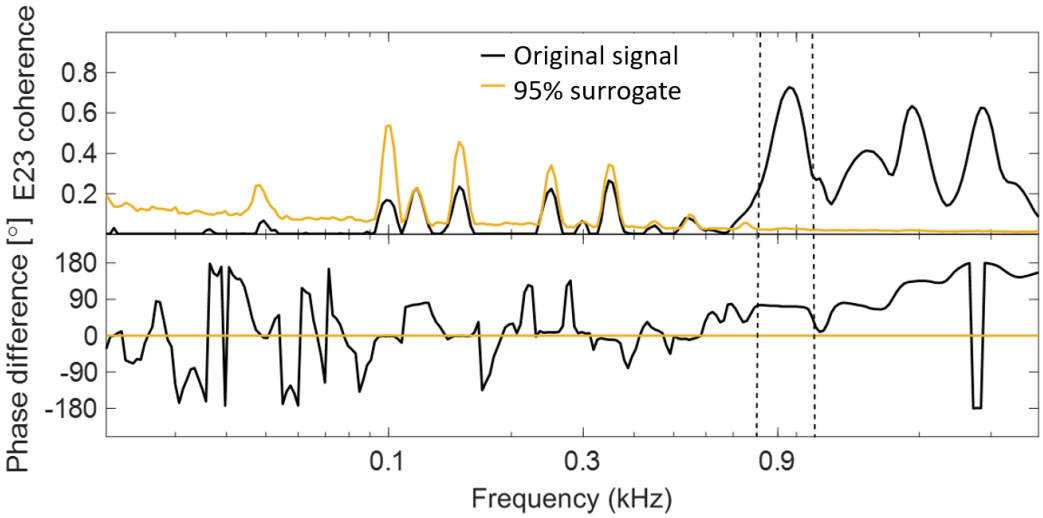

Figure 4.4: (a-b) Wavelet phase coherence and phase difference of signals from the pair of electrodes (E1,E2). The main frequency component is chosen as the significant phase coherence and the corresponding phase difference lies between the black dashed lines. Coherence below the 95th percentile of the surrogates (yellow curve) is not considered significant.

can also calculate the phase difference $\Delta\theta_{kn}$ between two signals according to

$$\Delta\theta_{kn} = \theta_{2k,n} - \theta_{1k,n}. \tag{4.15}$$

The value of $\Delta\theta_{kn}$ lies within 180° and gives information about the phase of one oscillator relative to the other.

Connections may be found between two signals or components due to the interactions between them, or common external influences affecting both. The calculated coherence between processes is not reliable unless we can repeat the calculation while the interaction or common influence is absent. One way to test for significance coherence uses surrogate signals [105]. The type of surrogate that we use with our signals is the iterative amplitude adjusted Fourier transform (IAAFT) that we introduced in Sec. (4.4). The null hypothesis here is that the phase between the signals is independent for all frequencies. It means that surrogates can be produced by randomization of the time-phase information [44].

In our study, the wavelet phase coherence and the corresponding phase difference were calculated between pairs of signals, for example those from electrodes E2 and

E3 as shown in Fig. 4.4. The phase coherence at each frequency was considered significant if the original signal is higher than the 95th percentile of 100 surrogates in the frequency range of interest. Fig. 4.4 shows that the phase coherence exists in the range 826 - 111 Hz where the two peaks above this range are considered to be high harmonics. The phase difference (constant) was only taken into consideration at the frequencies where significant coherence was observed.

Couplings

Before introducing the dynamical Bayesian inference method, which is used to determine if a pair of oscillators in a system are coupled [106, 107, 108, 109], we describe a more basic approach that can be used to measure the similarity between two signals, which is cross correlation.

Cross correlation is a measure of similarity or coherence between two sets of signals relative to one another as a function of the time delay applied to one of them. The cross correlation between a pair of continuous time series, $u(t)$ and $v(t)$ is given by

$$\begin{aligned} w(t) = u(t) \otimes v(t) &\triangleq \int_{-\infty}^{\infty} u^*(\tau) v(\tau + t) d\tau \\ &= \int_{-\infty}^{\infty} u^*(\tau - t) v(\tau) d\tau \quad [\text{sub: } \tau \to \tau - t] \, . \end{aligned} \tag{4.16}$$

The complex conjugate, $u^*(\tau)$ makes no difference if $u(t)$ is real-valued but makes the definition work even if $u(t)$ is complex-valued.

Correlation versus Convolution:

$$\begin{aligned} u(t) \otimes v(t) &= \textstyle\int_{-\infty}^{\infty} u^*(\tau) v(\tau + t) d\tau \qquad [\text{correlation}] \\ u(t) * v(t) &= \textstyle\int_{-\infty}^{\infty} u(\tau) v(t - \tau) d\tau \qquad [\text{convolution}] \, . \end{aligned}$$

Unlike convolution, the integration variable, τ, has the same sign in the arguments of $u(\cdots)$ and $v(\cdots)$. Thus, the arguments have a constant difference instead of a constant sum (i.e. $v(t)$ is not time-flipped). The argument of $w(t)$ is named the "lag" (= delay of u versus v).

Normalized Cross-correlation: The cross-correlation given by Eq. (4.16) is not unitless. It depends on the units of the two signals and thus it will be difficult to compare cross-correlations from different data sets. Hence normalized cross-correlation is needed to prevent a reduction in the sum of the products with increasing lags, by making the cross-correlation unitless.

From Eq. (4.16), if we present $y(t) = u(t - t_0)$ for some fixed t_0, then $E_y = E_u$:

$$E_y = \int_{-\infty}^{\infty} |y(t)|^2 dt = \int_{-\infty}^{\infty} |u(t - t_0)|^2 dt$$
$$= \int_{-\infty}^{\infty} |u(\tau)|^2 d\tau = E_u \quad [t \to \tau + t_0] .$$

Cauchy-Schwarz inequality: $\left| \int_{-\infty}^{\infty} y^*(\tau) v(\tau) d\tau \right|^2 \leq E_y E_v$

$$\Rightarrow |w(t_0)|^2 = \left| \int_{-\infty}^{\infty} u^*(\tau - t_0)\, v(\tau) d\tau \right|^2 \leq E_y E_v = E_u E_v$$

but t_0 was arbitrary, so we must have $|w(t)| \leq \sqrt{E_u E_v}$ for all t.
We can provide the normalized cross-correlation as

$$z(t) = \frac{u(t) \otimes v(t)}{\sqrt{E_u E_v}} \tag{4.17}$$

with properties:

- $|z(t)| \leq 1$ for all t
- $|z(t_0)| = 1 \Leftrightarrow v(\tau) = \alpha u(\tau - t_0)$ with α constant

Correlation coefficient: The presence or absence of a relationship between two random variables in the first approximation is judged by the correlation field. From Fig. 4.5, A positive correlation between random variables characterizes such a probabilistic dependence at which, with the increase of one of them, the other will increase on average as shown in Fig. 4.5 a). For a negative correlation with an increase in one random variable, the other decreases on average Fig. 4.5

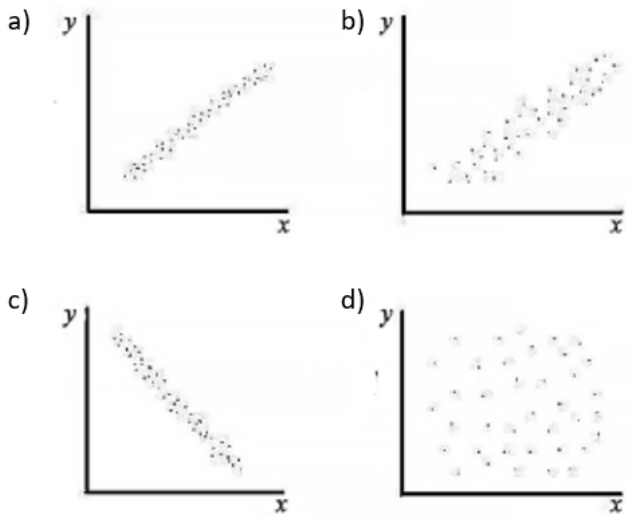

Figure 4.5: Correlation field of two random variables: with different kinds of correlation: a) strong positive; b) weak positive; c) strong negative; d) absence of correlation.

b). Correlation analysis helps us to estimate the closeness of the relationship of differences parameters or factors affecting the process. In general, the task of identifying and assessing the strength of communication in mathematical statistics has not been solved. There are only indicators that allow to evaluate one or another side of a random connection.

Regression: It is a statistical technique that predicts the value of the dependent variable Y based on the known value of the independent variable X through an equation of the form $Y = a + bX$.

P-value: A p-value defines the probability that the null hypothesis can be true. In our case, it represents the probability that the correlation between two time series occurred by chance. A p-value of 0.05 means that there is only a 5% probability that results from the signals occurred due to chance. A p-value of 0.01 means that there is only 1%probability. So lower p-values are good, but how low is "low enough"? In most research the threshold to what we consider statistically significant can be a p-value of 0.05 or below and it is called the significance level α_p.

Cross-correlation works well for linear and stationary signals, but it is not suitable for nonlinear and nonstationary signals because, by definition, the cross-

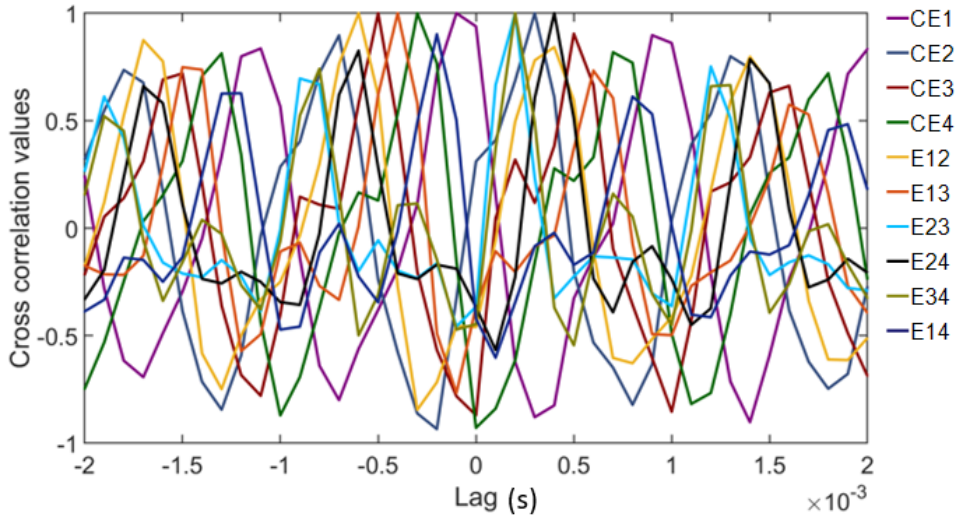

Figure 4.6: The cross-correlation series of pairs of electrodes signals at low electron density and pressing voltage $V = 4.20$ V with a maximum delay of 0.002 s. The lines are color-coded to indicate particular electrode pairs.

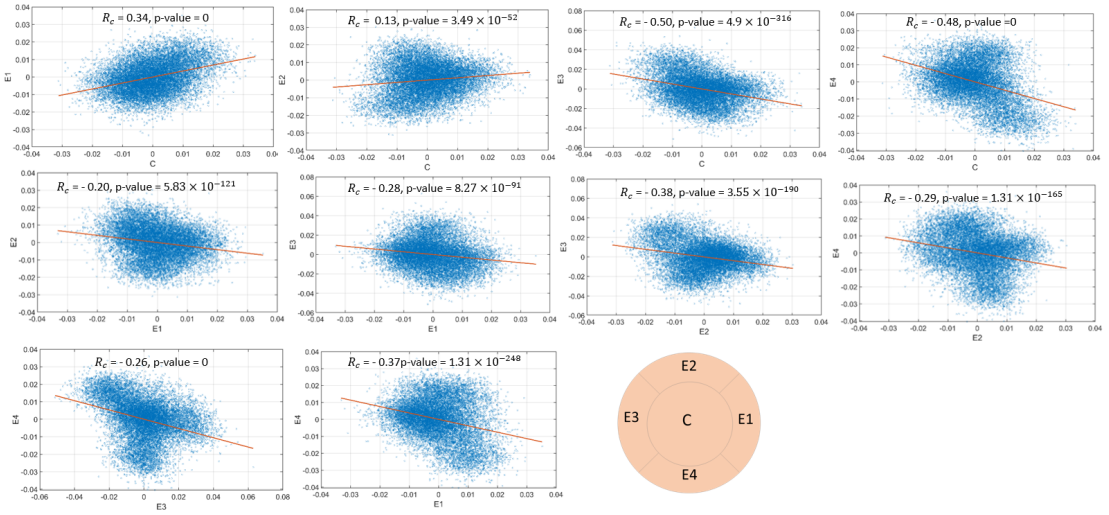

Figure 4.7: A regression plot of pairs of electrodes signals at low electron density and pressing voltage $V = 4.20$ V with the values of the slope and p- values.

correlation function assumes that the signals are linear and time-invariant. In nonlinear systems, the relationship between the input and output signals is not linear and cannot be described by a simple mathematical function. In nonstationary signals, the statistical properties of the signals change over time, making it difficult to compare two signals at different points in time. Therefore, cross-correlation is inappropriate for use in conjunction with nonlinear and nonstationary signals [110]. The important thing in our study is visualizing the interaction between the electrons and the surface of the liquid helium, which can be nonlinear. Therefore,

cross-correlation is unsuitable for our data and we need nonlinear dynamics methods to study the nonlinear features characterising our system.

As an illustration, we now compute the cross-correlation to investigate the relationship between pairs of electrodes signals at low electron density and pressing voltage $V = 4.20$ V in the time domain. Fig. 4.6 presents examples of the resultant cross-correlations between the signals from pairs of electrodes at low electron density and a pressing voltage $V = 4.20$ V with a maximum delay of 0.002 s. Obviously, there are no positive correlations, no regressions, and no linear relationships between most of the pairs of signals, for both electron densities, and with various pressing voltages.

Indeed, conventional stationary analysis methods and linear statistical approaches have inherent limitations in their ability to capture nonlinear and non-stationary variations in the data. For instance, the power spectral density cannot identify the temporal localization of particular frequency components or reveal their features, because it assumes that the spectral components are stationary. Furthermore, linear statistical approaches, e.g. regression models or the analysis of correlation, have certain difficulties in capturing the nonlinearity and non-stationarity of time series [111]. Inevitably, therefore, linear and stationary methods lead to less realistic characterization and estimation of the time series from our electrons on helium system.

Dynamical Bayesian Inference (DBI): This method can be used to estimate the relationship between the two components and how they are coupled. The frequencies and amplitudes of certain oscillators may change in time within a system. Then, their interactions with other components may also evolve in time. Indeed, dynamical Bayesian inference (DBI) identifies the couplings between oscillators as functions of time; thus, this method may be used to understand the true nature of underlying a system [108, 112, 113]. It is based on Bayes' theorem using knowledge of the system's evolution to predict its future condition. DBI can identify the

model of the dynamical system for a pair of the oscillators in terms of coupling functions. These functions provide the interaction between two oscillators [46]. An approximation that can be used, especially when the coupling is weak, is that the joint phase dynamics can be decoupled (unidirectionally) from the overall dynamics, giving differential equations:

$$\begin{cases} \dot{\phi}^1(t) = q_1\left(t, \phi^1(t), \phi^2(t)\right) \\ \dot{\phi}^2(t) = q_2\left(t, \phi^1(t), \phi^2(t)\right) \end{cases} \tag{4.18}$$

where $\phi^i(t)$ is the phase oscillator i at time t, and q_i is the coupling function from ϕ^j to ϕ^j [108]. A phase coupling is a process that describes how the phase of one oscillator affects the phase of another.

To obtain the interactions between oscillatory components within the signal, we need first to calculate the phases of the oscillatory components for equation (4.18). These are determined from time-frequency representations via using ridge extraction. The interactions between various pairs of oscillators are studied in order to determine their direction in the system. During the ridge extraction process, the oscillatory components must occupy the disjoint frequency bands to prevent interference.

The coupling function is time-dependent and it assumed to be slowly varying because of the assumption of the oscillator frequencies being slowly varying. Thus, the $q_i^{t_n}\left(\phi^1, \phi^2\right)$, time-independent coupling strength approximations, are calculated within specified time windows. The coupling strength within each time-window is computed by determining whether the phase of one component is influenced by the other and vice versa. For accurate results, the window size is selected to include at least 10 cycles of the lowest frequency across the two frequency ranges. The approximating coupling functions $q_i^{t_n}$, can be selected to lie within the span of some finite number of Fourier basis functions, for all pairs of phases (ϕ^1, ϕ^2) at a time t_n is given by

$$q\left(\phi^1,\phi^2\right)=a_0+\left(\sum_{j=1}^{K}b_j\cos\left(j\phi^2\right)+c_j\sin\left(j\phi^2\right)\right)$$
$$+\left(\sum_{i=1}^{K}\sum_{j=-K}^{K}d_{ij}\cos\left(i\phi^1+j\phi^2\right)+e_{ij}\sin\left(i\phi^1+j\phi^2\right)\right), \tag{4.19}$$

for the constants a_0, b_j, c_j, d_{ij} and e_{ij}. Based on Bayes' theorem, a statistical inference algorithm is utilized within each window to identify the values of the signal $(\phi^i(t), \phi^j(t))$ [96]. For a given K- value called the Fourier order, there are $(2K+1)^2$ degrees of freedom for each of the two functions $(\phi^i(t), \phi^j(t))$ when determining the interaction between two oscillators. This K is chosen as a second-order Fourier coefficient which is used to determine the number of degrees of freedom, and the set of K avoids introducing too many degrees of freedom which can cause overfitting leading to inaccurate predictions. After computing the result in a given time window, the degree to which it affects the calculation of the subsequent window is determined by the propagation constant $p \geq 0$ (cf. our other use of p for statistical likelihood). A larger value of p means that the result impacts more on the calculation within the next window. Having too large a value of p for coupling functions which change with time will limit the accuracy of the results.

During each time window, the coupling strength from one signal to another is defined as

$$\epsilon_{2\to1}\left(t_n\right):=\left(\int_0^1\int_0^1 q_1^{t_n}(2\pi u,2\pi v)^2 dudv\right)^{\frac{1}{2}}=\left\|q_1^{t_n}\right\|$$
$$\epsilon_{1\to2}\left(t_n\right):=\left(\int_0^1\int_0^1 q_2^{t_n}(2\pi u,2\pi v)^2 dudv\right)^{\frac{1}{2}}=\left\|q_2^{t_n}\right\|. \tag{4.20}$$

We refer to $\epsilon_{2\to1}$ as the coupling strength from ϕ^2 to ϕ^1 at time t_n. Each of these values $\epsilon_{j\to i}$ is simply equal to the Euclidean norm of the $(2K+1)^2$-dimensional vector of coefficients in the Fourier expression for $q_i^{t_n}$. Eqs. (4.20) are rewritten

$$\epsilon_{j\to i}:=\left(\int_0^1\int_0^1\left[q_i^{t_n}(2\pi u,2\pi v)-a_0^{(i)}\right]^2 dudv\right)^{\frac{1}{2}}, \tag{4.21}$$

where $a_0^{(i)}$ defines the constant term in the Fourier expression for $q_i^{t_n}$. Indeed, the angular velocity of the phase oscillator i at time t should be constant if it is not being affected by another oscillator j. The significance of the coupling strength $\epsilon_{2\to1}$ from ϕ^2 to ϕ^1 is tested by using the surrogates method. Surrogates are used to test the statistical significance of the apparent coupling between two oscillators.

Cross-correlation is a useful tool for finding the similarity between two signals, but it has some limitations when dealing with nonlinear and nonstationary signals. In these cases, cross-correlation can give misleading results because it assumes linearity and stationarity of the signals.

Dynamical Bayesian Inference (DBI), on the other hand, provides a more flexible framework for estimating the coupling between nonlinear and nonstationary signals. DBI models the underlying dynamics of the signals as a probabilistic process and uses Bayesian inference to estimate the parameters that describe the coupling between the signals.

DBI can also incorporate prior knowledge about the system and can incorporate uncertainty in the measurements, making it a more robust method for estimating the coupling between signals in noisy and complex systems.

4.4 Surrogates

Surrogates can be defined as artificial signals that are utilized to investigate whether systems might have a certain property. They behave like the system that is under investigation, but they do not own the property under investigation. There are various types of surrogates that can be used for different applications [100]. The original ("real") signal from any system, and its surrogates are treated in exactly the same way. After applying the chosen technique to the original signal, and to the surrogate set, the results obtained from the original data are compared to the distribution of results obtained from the surrogates. If the difference between the original data and the set of the surrogates is significant, with a certain confidence level (depending on the chosen statistical threshold), then one can consider that the

original system has the particular property of interest. However, if the test is not sufficiently strong, then the system cannot be regarded as having such a property. Surrogates are thus used to test the significance of results obtained during the analysis of wavelet phase coherence and dynamical Bayesian inference.

For dynamical Bayesian inference (Sec. 4.3.8), the surrogates method is utilized to test the statistical significance of the calculated coupling between two oscillators. The surrogates test provides a relative value of the coupling strength. The type of surrogate test used for dynamical Bayesian inference uses cyclic phase permutation (CPP). The signals will cycle between 0 and 2π. The signal is divided into complete cycles, which are randomly permuted, while the incomplete cycles at the beginning and end remain fixed.

The surrogates are created from the signals themselves. In the analysis for the wavelet phase coherence analysis, IAAFT surrogates are used, see Sec. 4.3.8 possible existence of high harmonics, as well as in and 4.3.7. We used the amplitude adjusted Fourier transform (AAFT), and iterative amplitude adjusted Fourier transform (IAAFT) surrogates in testing for significance in wavelet phase coherence: see Sec. 4.3.8. The null hypothesis for both is that the phases in the signals are independent for all frequencies, which means that surrogates can be generated by the randomization of the time-phase information in the signals [44].

Thus, for the case of phase coherence, the baseline for significance detection was the phase coherence calculated between the signal and IAAFT surrogates. However, in harmonic detection, a local maximum in the values of the mutual information calculated for a pair of phases from the original data is deemed to indicate a harmonic if it occurs some number of standard deviations above the mean value of the surrogates' mutual information [93].

The surrogates are used to test a null hypothesis at a chosen level of significance α, where the signficance level $\alpha \in (0, 1)$. For a one-sided test $1/(1-\alpha)-1$ surrogates should be generated, and $2/(1-\alpha)-1$ surrogates for a two-sided test. Comparing the value of the statistic from the data under investigation with the distribution of

values calculated from the surrogates, the null hypothesis may be rejected when the data deviate sufficiently from the surrogates. Otherwise, it may not [114]. To increase discrimination power, we need to increase the number of surrogates. The number of surrogates was chosen to be 100 for both methods (phase coherence and DBI).

The analysis is performed on both the original data and a set of surrogate data. The outcome from the original data is then compared with the distribution of outcomes obtained from the surrogates. If the comparison reveals a substantial discrepancy, it can be concluded that the original data and the system they represent have a specific characteristic with a specified level of confidence. Conversely, if there is no noticeable difference, it cannot be stated that the system possesses such a property, or the test may not be sufficient to confirm it.

4.5 Chronotaxic systems: stability of non-autonomous interacting systems

Stable oscillatory dynamics may be described by, model autonomous, self-sustaind limit-cycle oscillators. Although this model provides stable amplitude dynamics, its frequencies can easily be affected by even the weakest external perturbations [115]. However, there is a type of stable oscillatory system which has a determined frequency. The frequency of its oscillations are time dependent but stable—i.e., its time-dependent value is stable against external perturbations. To account for this frequency stability a completely new approach is required. Such systems are nonautonomous and if, at the same time their frequencies exhibit resistance to external perturbations, they may also be designated as chronotaxic [10, 84, 116]. A chronotaxic system is explicitly time-dependent. It possesses a time-dependent point attractor making it robust against e.g. an external drive system. This can allow the frequency to be determine externally through this drive and response system, giving rise to determinism even when faced with strong perturbations.

These chronotaxic (*chronos*-time, *taxis*-order) systems were introduced to provide a framework for non-autonomous systems that can endure continuous external perturbation. These systems can also characterize oscillatory systems with time-varying, but stable, amplitudes and frequencies.

The definition of a chronotaxic system is given by,

$$\dot{\mathbf{p}} = \mathbf{f}(\mathbf{p}); \quad \dot{\mathbf{x}} = \mathbf{g}(\mathbf{x}, \mathbf{p}), \tag{4.22}$$

where $\mathbf{p} \in R^n, \mathbf{x} \in R^m, \mathbf{f} : R^n \to R^n, \mathbf{g} : R^m \times R^n \to R^m$, where n and m can be any positive integers; $\mathbf{x}\,(t, t_0, \mathbf{x}_0)$, the solution of Eqs. (4.22) depends on the time t and the initial condition $(t_0, \mathbf{x}_0)$, while the solution $\mathbf{p}\,(t - t_0, \mathbf{p}_0)$ depends on the time of development $(t - t_0,)$ and on the $\mathbf{p_0}$ which defines the initial condition. The nonautonomous system $\mathbf{x}$ can be considered as driven by the system $\mathbf{p}$ in the sense that it can be described by an equation which depends on time explicitly, $\dot{\mathrm{x}} = \mathrm{g}(\mathrm{x}, \mathbf{p}(t))$. The driven system $\mathbf{x}$ is assumed to be known, and $\mathbf{p}$ which is assumed to be in not accessible for observation, as often occurs in many case of the real system. Thus, the dynamics of $\mathbf{x}$ are used to study the evolution of the system $\mathbf{p}$. With these assumptions the system $\mathbf{p}$ creates a time-dependent steady state in the dynamics of $\mathbf{x}$ as shown in Fig. 4.8 (a).

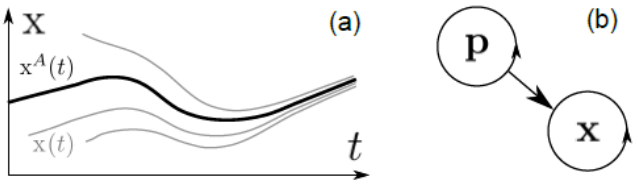

Figure 4.8: (a) Moving point attractor in a chrontaxic system, (b) simplest case of a chronotaxic system $\mathbf{x}$, driven by $\mathbf{p}$.

Therefore, $\mathbf{x}$ is a system which is considered to be thermodynamically open. The driving $\mathbf{p}$ makes the system chronotaxic. External perturbations are also considered, arising from everything in $\mathbf{x}$ and $\mathbf{p}$ that can affect the system. For the unperturbed state, the dynamical system $\mathbf{x}$ is a time-dependent steady state, also called a point attractor, and denoted $\mathbf{x}^A(t)$. For the initial condition $\mathbf{x_0}$ at

$\mathbf{t_0}$, when the solution of the system asymptotically approaches the time-dependent steady state $\mathbf{x^A}$, a condition of forward attraction for $\mathbf{x^A}$ is,

$$\lim_{t\to+\infty} \left|\mathbf{x}\left(t, t_0, \mathbf{x}_0\right) - \mathbf{x}^A(t)\right| = 0. \tag{4.23}$$

It can only be satisfied when the chronotaxic system is not perturbed. Indeed, this condition may not be adequate to describe the time-dependent point attractor in a real system, especially when considering the stability of the system at the current time t, not the infinite future. To resolve this, a condition of pullback attraction must also be satisfied by $\mathbf{x}^A(t)$, in a chronotaxic system,

$$\lim_{t_0\to-\infty} \left|\mathbf{x}\left(t, t_0, \mathbf{x}_0\right) - \mathbf{x}^A(t)\right| = 0. \tag{4.24}$$

This condition defines a time-dependent point attractor at current time t. With considering the condition in Eq. (4.24) at times $t > -\infty$, it follows that the point attractor $\mathbf{x}^A(t)$ satisfies the condition of invariance, the condition that $\mathbf{x}^A$ presents a solution of the system in Eq. (4.22),

$$\mathbf{x}\left(t, t_0, \mathbf{x}^A\left(t_0\right)\right) = \mathbf{x}^A(t). \tag{4.25}$$

The two Eqs.(4.23) and (4.24) determine an asymptotic convergence in the infinite future, starting from the infinite past. This convergence will let $\mathbf{x}\left(t, t_0, \mathbf{x_0}\right)$ deviate from the time-dependent steady state $\mathbf{x}^A$ during a finite time interval. It means that, this interval, the ability of the system to resist continuous external perturbations will not be available. Thus, in order to describe the ability of system to maintain its dynamics, another condition for a chronotaxic system is that it should satisfy the condition of contraction. The phase space R^m, $\mathbf{x} \in R^m$ should be within $C(t)$, a contraction region to that, for any trajectories $\mathbf{x}_1$, $\mathbf{x}_2$ of the system inside the $C(t)$, $\mathbf{x}_i\left(t, t_0, \mathbf{x}_{0i}\right) \in C(t)$, i=1,2, the distance between two trajectories can only decay in time,

$$\frac{d}{dt}\left|\mathbf{x}_1\left(t,t_0,\mathbf{x}_{01}\right)-\mathbf{x}_2\left(t,t_0,\mathbf{x}_{02}\right)\right|<0. \tag{4.26}$$

The $C(t)$ can be finite, and the two trajectories can eventually leave this area. Thus, the contraction region $C(t)$ within a chronotaxic system should have a finite area $A', A' \subset C$: the solutions of the system will start in A' and never leave it, $\forall t_0 < t, \forall \mathrm{x}_0 \in A'\left(t_0\right), \mathrm{x}\left(t,t_0,\mathrm{x}_0\right) \in A'(t)$.

In a case where the conditions are fulfilled, the time-dependent attractor x^{A} will be located inside the area A' of the contraction region C.

If the above condition are fulfilled, then, the dynamics of $\mathbf{p}$ can be either chaotic or stochastic. In unperturbed chronotaxic systems, the dynamics of $\mathbf{x}$ will be defined by the dynamics of $\mathbf{p}$ and will still be deterministic. For a chronotaxic system to be considered perturbed, it is only important to consider the perturbations to the $\mathbf{x}$ component. as any perturbations to $\mathbf{p}$ can be included in its dynamics assuming that $\mathbf{x}$ cannot be easily changed by $\mathbf{p}$.

For example, the following system can be considered to be chronotaxic,

$$\begin{aligned}
\mathbf{x} &= \left(r_{\mathbf{x}}\cos\left(\alpha_{\mathbf{x}}\right), r_{\mathbf{x}}\sin\left(\alpha_{\mathbf{x}}\right)\right), \\
\dot{r}_{\mathbf{x}} &= \varepsilon_r r_{\mathbf{x}}\left(r_0 - r_{\mathbf{x}}\right), \\
\dot{\alpha}_{\mathbf{x}} &= \varepsilon\omega_0(t)\sin\left(\alpha_{\mathbf{x}} - \alpha_{\mathbf{p}}(t)\right) + \xi(t).
\end{aligned}$$

where ε_r and ε are constants and $|\varepsilon| \geq 1$, $\omega_0(t) > 0$. The external perturbations $\xi(t)$ do not cause $\alpha_{\mathbf{x}}$ to drift from the unperturbed phase as shown in Fig. 4.9 (a). By reducing the coupling to $\alpha_{\mathbf{p}}(t)$ so that $|\varepsilon| < 1$, the system is no longer chronotaxic and $\alpha_{\mathbf{x}}$ strongly deviates from the unperturbed phase as presented in Fig. 4.9 (b).

4.6 Identifying chronotaxic systems

After the characteristics of a system have been defined as chronotaxic, the next question is how to deduce these dynamics and interactions from direct observation,

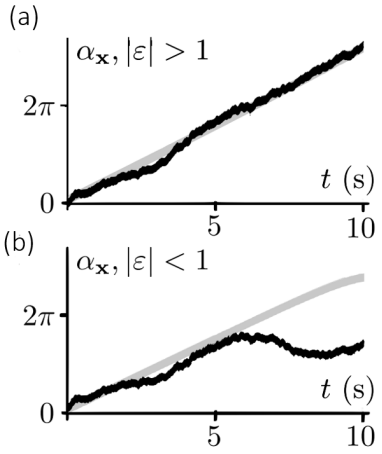

Figure 4.9: (a) The position (phase) α_x of the chronotaxic system on the limit cycle when unperturbed (straight gray line) and perturbed (noisy black line). (b) A moving point attractor does not exist on a limit cycle, the perturbed phase strongly deviates from the unperturbed phase. From [10], with permission.

i.e, via the inverse approach. As the underlying dynamics is recognized by the external driver, the system may also be impacted by other factors, which may be considered as noise. These may hide the chronotaxic dynamics if the accurate analytical method is not applied. Indeed, any methods dependent on averaging cannot provide an accurately method of recognizing the essential time-variability of the frequency emerging from the chronotaxic system. Therefore, with this novel class of system, new methods are needed to extract and identify the dynamics of complex drive systems. These methods are focused on the study of the influence of a drive system on a response system.

Two different methods are used to detect chronotaxicity [117]. They are phase fluctuation analysis (PFA) and dynamical Bayesian inference: see Sec. 4.3.8 on interactions. The current methods are only deal with the phase dynamics, i.e. the focus of these techniques is the ability of the time- varying frequency to resist external perturbations. Both approaches depend on different inferential bases to measure the effects of a signal. Phase fluctuation analysis takes into account the statistical effects observed in a signal. But, the Bayesian inference method can provide a model based on differential equations that can be used to produce a

measure of the dynamical mechanisms. The evaluation of chronotaxicity depends on the parameters of the inferred model. A functional connectivity is inferred via the phase fluctuation technique while the Bayesian inference method infers effective connectivity [118]. Which method is optimal depend on the properties of the signal.

4.6.1 Extracting the phase estimates

As described above, the first step that we should take to find out if the time series contain chronotaxic phase dynamics is based on the principle of extracting the unperturbed and perturbed phases of the oscillatory components. This process involves separating the phase and amplitude for an oscillation in the time series. It can be done through the use of the time-frequency representation analysis (continuous wavelet transform): see Sec. 4.3.4 [119]. This method can provide a good time localization and optimal frequency resolution that is ideal for the extraction of the instantaneous phases of oscillations.

The frequencies of certain oscillators can be traced in the continuous wavelet transform (CWT) $W_T(s,t)$ by using the ridge-extraction technique [99, 120]. This extraction method can be used to estimate the instantaneous frequencies of the oscillatory components in a signal: see Sec. 4.3.6. By following the extraction, the corresponding phase $\varphi_{\mathbf{x}}$ of the observed system is then $\arg[W_t(s,t)]$, which is purely time-dependent, where s and t denote the determined positions of the oscillations in the $s-t$ plane. After the estimated perturbed phase $\varphi^*_{\mathbf{x}}$ has been extracted, the next step is to determine the estimated unperturbed phase $\varphi^{A*}_{\mathbf{x}}$. It is hard to separate the dynamics corresponding to the phase $\varphi^A_{\mathbf{x}}$ from the effect of noise perturbations $\eta(t)$. This can be simplified by assuming that a signal cycle is smaller than the dynamics of $\varphi^A_{\mathbf{x}}$, which are confined to time scales. Also, the noise can be either weak or comparable in magnitude to these dynamics [117]. Based on these assumptions, the dynamics of the phase $\varphi^A_{\mathbf{x}}$ can be attained by filtering out the high frequency components of $\varphi^*_{\mathbf{x}}$, taking into account the need to retain the dynamics of $\varphi^A_{\mathbf{x}}$. The optimal way to achieve this, removing the high

frequency noise fluctuations without affecting the unperturbed dynamics, is by smoothing over the instantaneous frequency extracted from the continuous wavelet transform [9]. This will present the estimated angular velocity $\dot{\varphi}^A_{\mathbf{x}}$, which will be integrated over time to obtain the estimated driver phase $\varphi^{A*}_{\mathbf{x}}$. For improved accuracy in phase extraction and determination of an extracted oscillatory mode's physical significance, the nonlinear mode decomposition method can be used [43].

4.6.2 Dynamical Bayesian inference

Dynamical Bayesian inference can be used to detect chronotaxicity. It involves extracting the perturbed ($\varphi_{\mathbf{x}}$) and unperturbed ($\varphi^A_{\mathbf{x}}$) phases estimates from the collected data in order to model their interaction. The characteristics of the coupling functions between the extracted perturbed and unperturbed phases can reveal the dynamics of the system in terms of chronotaxicity. The ability of Bayesain inference to track time-dependent system parameters can be used to detect the chronotaxicity in the system which can move in and out of the chronotaxic state. To do that, Bayesian inference is applied to the two $\varphi^*_{\mathbf{x}}$ and $\varphi^{A*}_{\mathbf{x}}$ phases, following their extraction from the continuous wavelet transform, as described in Sec. 4.6.1. Then, DBI is used to simultaneously determine the coupling functions and their strengths between $\varphi_{\mathbf{x}}$ and $\varphi^A_{\mathbf{x}}$: see Sec. 4.3.8. We can conclude that the system is chronotaxic, if the strength coupling is only from the driver $\varphi^A_{\mathbf{x}}$ to $\varphi_{\mathbf{x}}$.

4.6.3 Phase fluctuation analysis

After estimation of the two phases $\varphi_{\mathbf{x}}$, $\varphi^A_{\mathbf{x}}$, the next step is to study the distribution of fluctuations in the system relative to the unperturbed trajectory, by computing the phase fluctuations $\Delta\varphi_{\mathrm{x}} = \varphi^*_{\mathrm{x}} - \varphi^{A*}_{\mathrm{x}}$.

Their distribution can vary, depending on whether the system is chronotaxic or not. To quantify it, we perform a detrended fluctuation analysis (DFA) on the phase fluctuations $\Delta\varphi_{\mathrm{x}}$ [121]. Indeed, DFA is used to determine the statistical self-similarity of the fluctuations on different time scales. It can distinguish the random

walk fluctuations of systems that are not chronotaxic from the less-integrated fluctuations of chronotaxic systems. The scaling of the various fluctuations that occur is determined by the existence of a self-similarity parameter α. The fluctuations on each time scale are equal to t/a which can be the same on large time scales t after multiplying by a^{α}.

The self-similarity parameter α can be computed by integrating the signal $\Delta\varphi_{\mathrm{x}}$ over t. Then, it is divided into parts of length n. The local trend is removed from each section by subtracting a fitted polynomial after choosing a first order linear fit [121, 122]. The root mean square fluctuation for the scale equal to n is then given by

$$F(n) = \sqrt{\frac{1}{N}\sum_{i=1}^{N} Y_n\left(t_i\right)^2}, \tag{4.27}$$

where $Y(t)$ defines the integrated and detrended signal and N is the length of the signal. If the signal is fractal, then the fluctuation amplitude $F(n)$ will follow the scaling law. By plotting $\log F(n)$ as function of $\log n$, the value of α is simply the gradient of the line. A chronotaxic system can be expected to have a DFA exponent between 0.5 and 1. When $\alpha > 1$, the system is non-chronotaxic.

The system will be affected if there are big perturbations which cause it to move forward or behind the current cycle to be attracted rather than an adjacent cycle. This behavior will be defined as a phase slip which will cause an increase in the DFA exponent and will cause a large jump in the estimated phase fluctuation. In this case, we need to distinguish between the cases of (i) a chronotaxic system with phase slips and (ii) a non-chrontaxic system. Phase slips can be identified by computing the distribution of the difference between the $\Delta\varphi_{\mathrm{x}}$ and the delay of these fluctuation by a timescale τ. Computing this $d\Delta\varphi_{\mathrm{x}}^{\tau}(t) = \Delta\varphi_{\mathbf{x}}(t+\tau) - \Delta\varphi_{\mathbf{x}}(t)$ will provide information about the perturbations of the system along τ. If phase slips occur, then the distribution of $|d\Delta\varphi_{\mathrm{x}}^{\tau}|$ will change with respect to a timescale [117].

4.6.4 Practical considerations

Phase fluctuation analysis and dynamical Bayesian inference both depend on precise phase extraction of the estimated attractor $\varphi_{\mathrm{x}}^{A*}$ and on its perturbed dynamics φ_{x}^{*}. Thus, these parameters in the respective methods must be selected carefully, based on the characteristics of the given signal.

The time-frequency representation provided by the wavelet transform will give the optimal compromise between time and frequency resolution. In fact, the wavelet frequency resolution f_r can be changed to suit specific needs. For instance, where there are phase slips, it may be appropriate to extract an estimate of the attractor, $\varphi_{\mathrm{x}}^{A*}$, with a higher frequency resolution. In our case we selected $f_r = 3$ to obtain good frequency resolution and smoother dynamics. However, the perturbed phase φ_{x}^{*} can also be extracted using a lower frequency resolution: if we choose $f_r = 0.2$, it results in increased time localization, which is useful for locating the time of each phase slip. The frequency resolution may also be increased to give greater distinction between oscillatory components, but of course this will adversely affect the time resolution. It should be borne in mind that frequency components must be separable in the time–frequency plane in order for these inverse methods to be applicable.

Indeed, the inverse methods presented will increase in reliability with longer signals. But, it is often not feasible to measure hundred of cycles of oscillation. Therefore, the time of signal recording should in practice be a compromise between a long signal and e.g. subject comfort when measurements are being made on a human. It is important, and more useful, to determine the lowest number of measured oscillations for which we can reliably test for chronotaxicity. It is found that, to make reliable observations of the dynamics and to test for chronotaxicity, the signal should include at least 30 cycles of the slowest oscillation.

An example of the use of phase fluctuation analysis (PFA) is presented in Fig. 4.10. The signal, of length of 47 seconds, was recorded at a pressing voltage of $V = 4.20\,\mathrm{V}$ and electron density $n_e = 1.4{\times}10^6\,\mathrm{cm}^{-2}$. It was analyzed using the

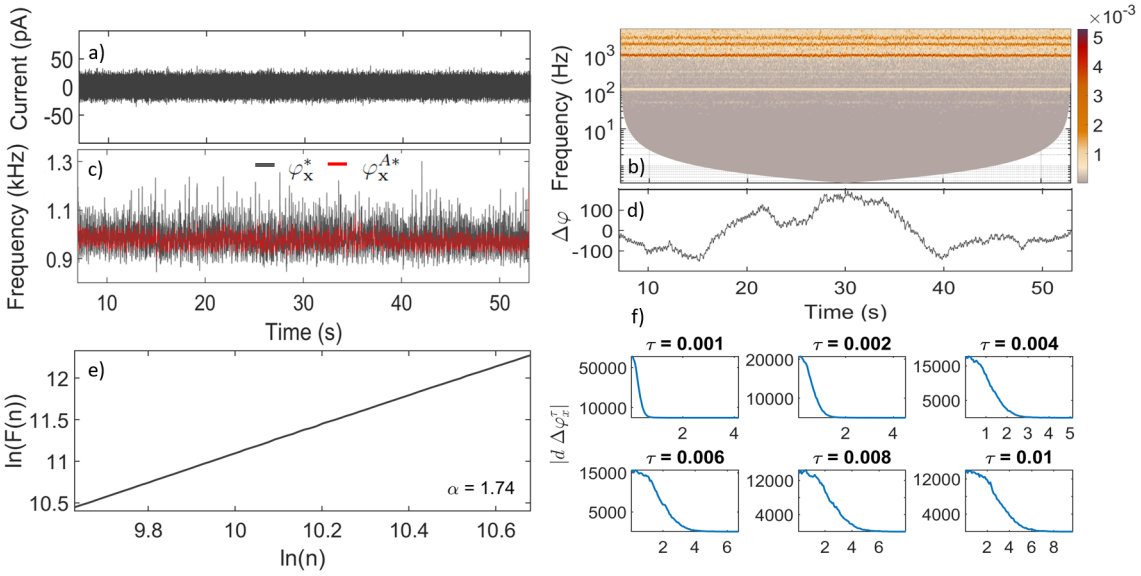

Figure 4.10: Example of application of the phase fluctuation analysis to the signal from E2, and its spectral analyses. (a) Signals with length 47 seconds at a pressing voltage of $V = 4.20$ V and electron density $n_e = 1.4{\times}10^6$ cm^{-2}. (b) The continuous wavelet transform with $f_0 = 4$ of signal in (a). (c) The instantaneous frequency is extracted from the wavelet transform in (b) using ridge extraction $\varphi_x^*($ (dark grey line), and smoothed. The smoothed frequency is then integrated in time to obtain an estimate of the unperturbed phase (red line) φ_x^{A*}. (d) $\Delta\varphi_x$ was calculated as $\varphi_x^* - \varphi_x^{A*}$. (e) shows the results of DFA analysis of $\Delta\varphi_x$: the DFA exponent is calculated and was 1.74 for the signal shown, suggesting that the system is not chronotaxic. Checking for phase slips in (f) shows the distributions of $|d\Delta\alpha_x^\tau|$, where the range shown was divided into 200 bins and the numbers in seconds indicate the value of τ.

continuous wavelet transform with a central frequency of $f_0 = 4$. The instantaneous frequency was extracted from the wavelet transform and smoothed, and the smoothed frequency was then integrated in time to obtain an estimate of the unperturbed phase (red line) φ_x^{A*}. The difference between the smoothed frequency and the unperturbed phase was calculated as $\Delta\varphi_x$ and was subjected to detrended fluctuation analysis (DFA). The resultant DFA exponent was 1.74, suggesting that the system is not chronotaxic. The analysis was further validated by checking for phase slips in Fig. 4.10 (f), thereby confirming that there were no phase slips.

However, the PFA method has limitations. It is based on averaging with a linear frequency resolution, which can provide a rough estimate of the two phases under clear and obvious conditions. However, it may fail to detect chronotaxicity if the contribution of nonlinearity is not incorporated with logarithmic frequency

resolution. In such cases, other methods such as dynamical Bayesian inference (DBI) are required. The DBI method is more precise than PFA when there is no full synchronization in the system, but it fails and is not recommended for use when there is full synchronization. In our case, the DBI method was successful in detecting chronotaxicity (as shown in Sec. 5.3.2). While applying the nonlinear mode decomposition (NMD) method would be interesting for future research, it is mathematically and computationally more demanding and was not applied in the present work

5. Results

This chapter introduces the analysis and results of the data measured as described and illustrated in chapter 3. It is divided into three sections. The first Sec. 5.1 discusses the characteristics of the oscillations measured from each of the five electrodes, at two different electron densities and varying the pressing voltage. Sec. 5.2 presents the frequency modulation of the main components. Sec. 5.3 provides the inferred direction of motion of the electrons inside the cell by using two ways to detect the motion: first, based on phase coherence and phase shift, as presented in Sec. 5.3.1; and secondly by use of dynamical Bayesian inference see as described in Sec. 5.3.2.

5.1 Characteristics of oscillations

5.1.1 Does the oscillation frequency fluctuate?

The signals, are used to show their frequency features, are sampled for 60 s with a sampling frequency of 100 kHz. The microwaves are switched on 6 s after the start of recording and switched off 7 s before the end. Fig. 5.1 (a) shows an example of a typical signal, with (b) an enlargement of the part that we analyze. Signals from all electrodes increase in amplitude under the MW irradiation. For low n_e and small V, the greatest increases are at electrodes C and E3 (closest to the MW input). With the nonautonomous system under investigation, representation in the frequency domain only is insufficient for obtaining all the information contained within the raw data. Conventionally, time-dependence is treated as noise and frequencies are

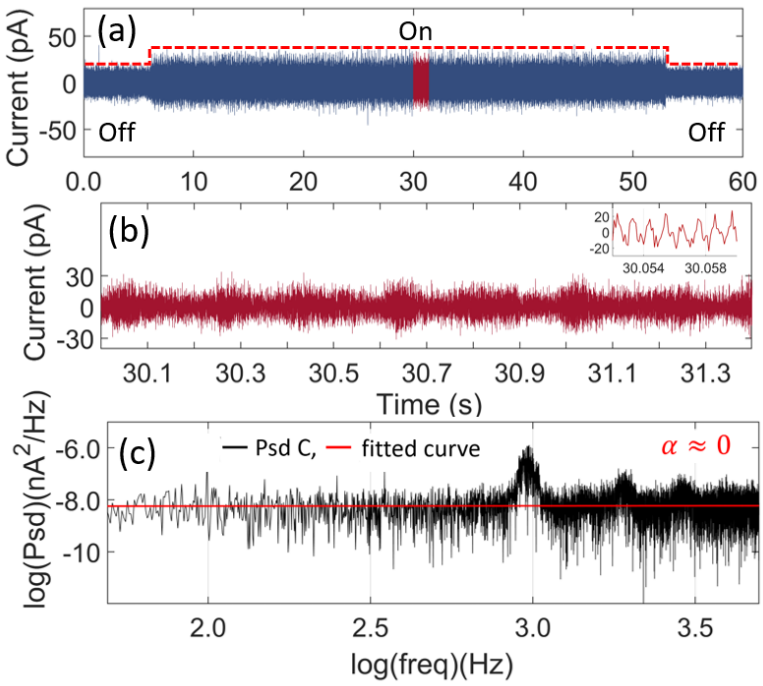

Figure 5.1: (a) Signal on the center electrode C recorded for 60 seconds at a pressing voltage of $V = 4.20\,\mathrm{V}$ and electron density $n_e = 1.4\times10^6$ cm^{-2}. The MW (139 GHz) is switched On/Off where indicated. (b) Zoomed-in reddened 1.4 s-long part of the signal in (a) used to obtain the characteristics of the oscillations, where the inset shows a further zoom to illustrate the pattern that emerges. Our conclusions are unaffected by the time interval chosen for this analysis. (c) Power spectral density of the oscillations in (b) showing the fundamental frequency and higher harmonics; its average gradient (α_{PSD}) is near zero.

time-averaged thus losing the information in the frequency variations. The power spectral density (PSD) [123] is computed for all signals within the selected 1.4 s of the original signal after down-sampling from 100 kHz to 10 kHz. The gradient of the PSD, for both electron densities and varying pressing voltages are leading to a spectral density commonly referred to as noise.

Application of the wavelet transform to the signal recorded from electrode C yields the spectra shown in Fig. 5.2 (a), where it is clearly evident that the basic frequency is varying. Similar behaviour was observed earlier using a single electrode [7, 34, 117]. Time-averaged wavelet powers for the signals recorded on each of the electrodes at $V = 4.18$ and $V = 4.20\,\mathrm{V}$ are shown in (c) for lower n_e and in (d) for higher n_e. The higher frequencies in the wavelet transform can be attributed to harmonic components due to the presence of nonlinearities [93].

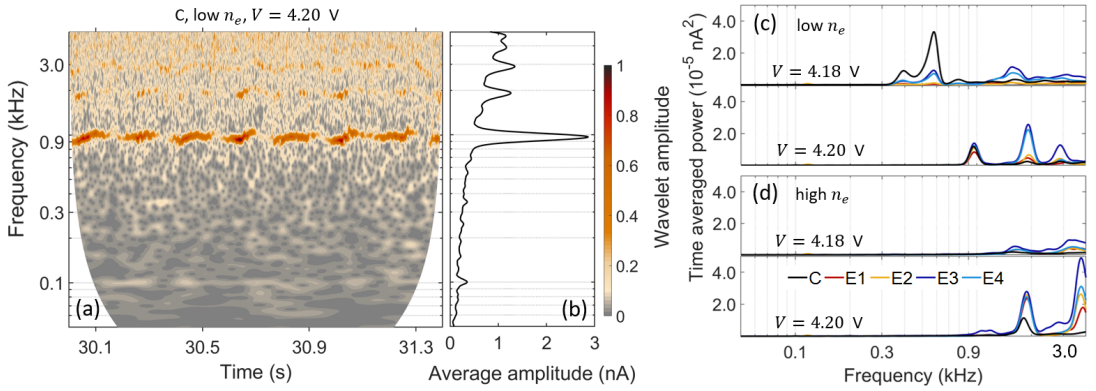

Figure 5.2: (a) The time-frequency representation (obtained via the wavelet transform with frequency resolution 3 Hz) of the signal is presented in Fig.5.1 (b), and (b) the corresponding time-averaged amplitude.(c-d) Time-averaged wavelet power of signals with MW on for each of the electrodes, as indicated: (c) is for the lower $n_e = 1.4\times10^6$ cm^{-2} and two different pressing voltages; (d) is for the higher $n_e = 2.2\times10^6$ cm^{-2} and the same two pressing voltages.

The more pronounced peak in the time-averaged spectral power for C at low n_e and $V = 4.18$ V in Fig. 5.2 (c) implies electron motion mostly under electrode C. For the given values of V and n_e, the frequency is found to be the same on all electrodes. At low electron density, the power is unevenly distributed among the electrodes. For $V = 4.16 - 4.20$ V, most of the power is associated with the central electrode, but it becomes more uniformly distributed among the four outer electrodes for $V = 4.21$ and 4.22 V. For the higher n_e, Fig. 5.2 (d), the spectral power is more uniformly distributed between the edge electrodes but is consistently lower for the central electrode (see Sec 5.1.2.

5.1.2 Time-averaged wavelet power analysis

We now present the time-averaged wavelet power for both electron densities and the current from each of the five electrodes (C, E1, E2, E3 and E4) with pressing voltages in the range $4.16 \leq V \leq 4.22$ V. Figs 5.3 5.4 shows the time-averaged wavelet power for low and high electron density, respectively. It is immediately evident that significant changes occur in the spectra for all electrodes as the pressing voltage changes. In Figs 5.3, We found that the most intense oscillation peak is at the C, E3 and E4 for pressing voltages V in the range 4.16 to 4.19 V; the peak starts

to decrease as V is increased from 4.20 to 4.22 V; while, for E1, E2, E3 and E4, the most intense oscillation peak is at a pressing voltage of 4.20 V. The occurrence of a uniform distribution in cells occurs at a resonance voltage of 4.20 V. For higher n_e, the electrons tend to concentrate near the edge of the cell: see Fig. 5.4.

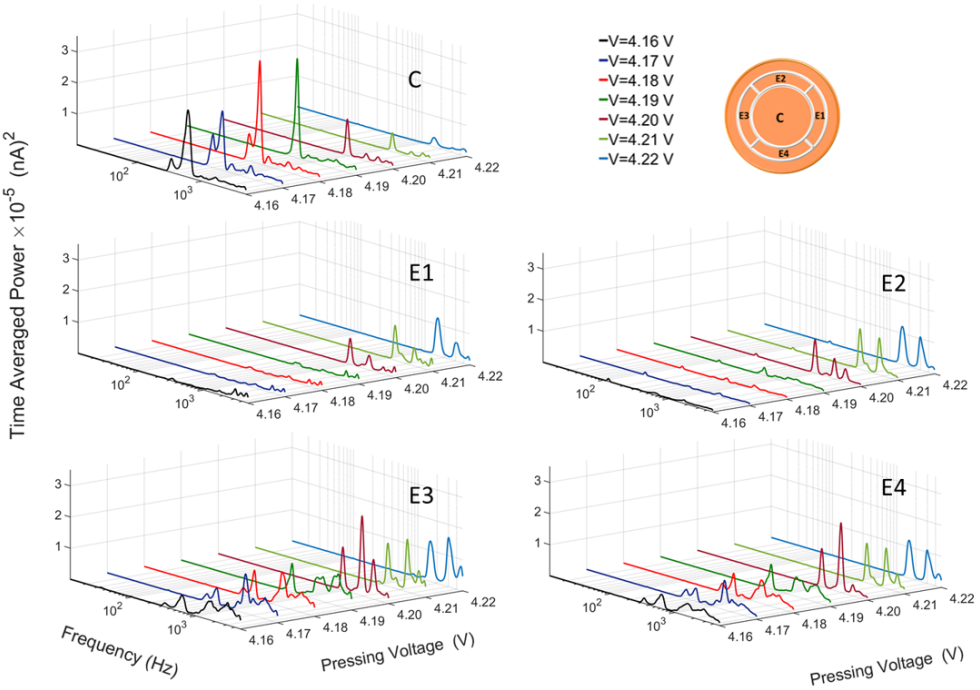

Figure 5.3: 3D time-averaged wavelet power of signals with MW On for each of the electrodes, as indicated for the lower $n_e = 1.4\times10^6$ cm^{-2} with different V.

5.2 Frequency modulation

The *instantaneous frequency* of each mode can be determined by ridge extraction (see Sec. 4.3.6), which traces in time the loci of the highest amplitude/power [11]. Typical results are shown in Figs. 5.5 (a) and (b). As shown in Fig. 5.5 (c), the highest peaks occur at ≈ 5 Hz for different pressing voltages and electron densities. These peaks define the frequency modulation of the oscillatory mode. This low frequency modulation ≈ 5 Hz revealed by the ridge extractions in Fig. 5.5 (a), (b) is almost independent of V. It is slightly different when n_e is high, compared with low n_e. For example, the average value at all v in the C is 5.21 Hz at low e_n and 5.10 Hz at high n_e.

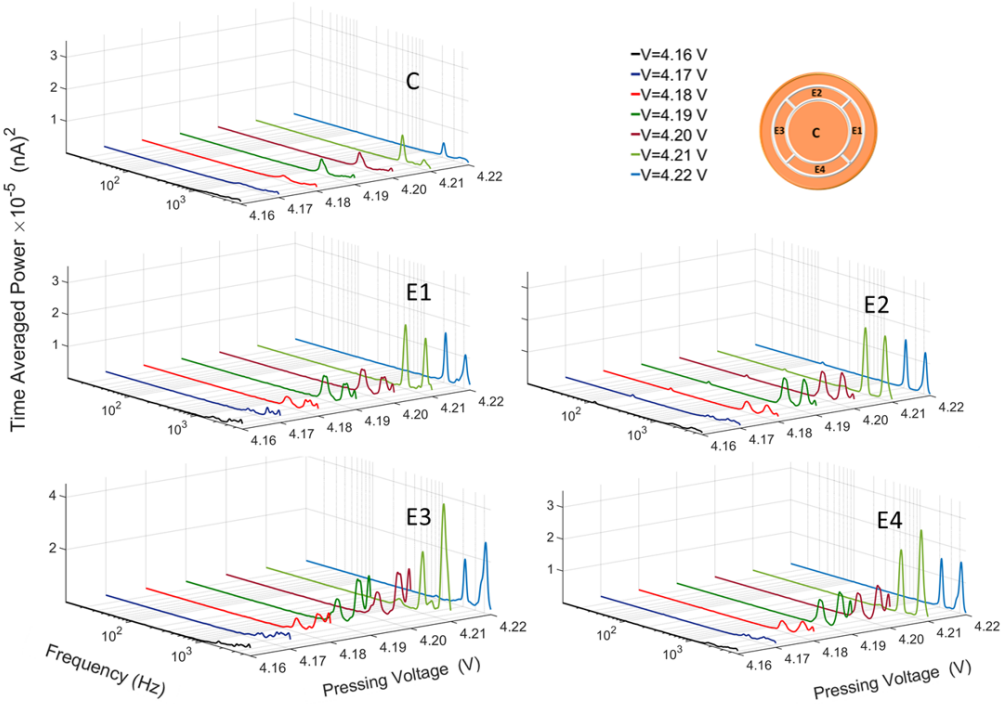

Figure 5.4: 3D time-averaged wavelet power of signals with MW On for each of the electrodes, as indicated, for the higher $n_e = 2.2\times10^6$ cm^{-2} and the same V as in Fig. 5.3.

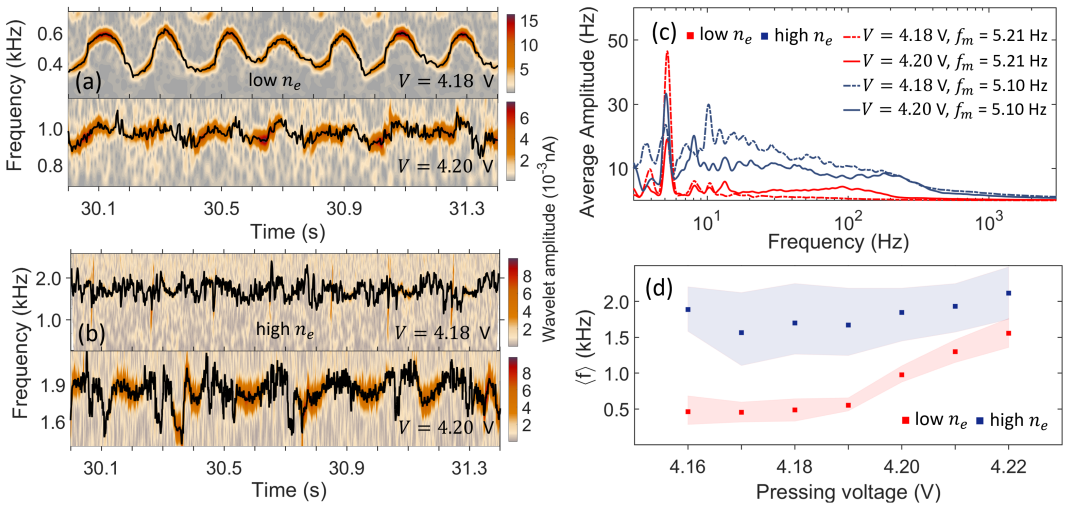

Figure 5.5: (a) Ridge extractions (black lines) for the signal on C, obtained from the time-frequency representation [11], showing the instantaneous frequency variations of the main component, for the lower electron density $n_e = 1.4\times10^6$ cm^{-2} and two different pressing voltages V. Colour bars show the intensity of the oscillations. (b) As in (a) but for higher electron density $n_e = 2.2\times10^6$ cm^{-2}. (c) Average amplitudes of the ridge extractions in (a) and (b). The frequencies of the sharp peaks near 5 Hz are indicated. (d) Mean oscillation frequency on C as a function of V for the lower (red squares) and higher (blue squares) electron densities n_e, respectively. The shadows show the full frequency ranges of the oscillations.

Fig. 5.5 (d) shows how the mean oscillation frequency for C changes with V for different n_e. We note that the mean frequency starts to increase at $V \sim 4.19\,\mathrm{V}$ when the electron density is low with only a minimal difference between the maxima and minima of the oscillations (red shadow), perhaps due to an accumulation of electrons under the edge electrodes [7]. For larger n_e, the mean frequency is higher and almost independent of V. Table 5.1 shows examples of the mean, frequency modulation and standard deviation of the instantaneous oscillation frequency for different pressing voltages, calculated for the C electrode at low electron density. This table shows the maximum and minimum frequencies of the main frequency mode of oscillations. The mean of the main frequency component increase with increasing the pressing voltage. However, in Table 5.1, the standard deviation of the instantaneous frequency oscillations for the main component decreases with rising pressing voltage until 4.20 V, and then starts to increase.

C						
Pressing Voltage (V)	f_{max} (Hz)	f_{min} (Hz)	Median f (Hz)	Frequency modulation f_m (Hz)	Mean Frequency $\langle f \rangle$ (Hz)	Standard deviation f (Hz)
4.16	683	285	430	5.25	463	116
4.17	597	319	454	5.10	454	78
4.18	643	331	453	5.22	488	81
4.19	656	474	549	5.22	553	47
4.20	1102	875	965	5.22	975	44
4.21	1466	1149	1297	5.25	1300	68
4.22	1763	1358	1539	5.33	1555	97

Table 5.1: Maximum, minimum frequency, mean frequency and deviation of the instantaneous frequency oscillations for the main component with varying pressing voltage calculated for the signals from C electrode at low electron density.

5.3 How to visualize the motion of the electron inside the cell?

In this section we will introduce two methods to investigate the dynamics and interactions of the oscillatory components within the data. These methods allow for showing the motion and the direction of the electrons inside the cell to be inferred. The first Sec. 5.3.1 presents the phase coherence and the phase shift for

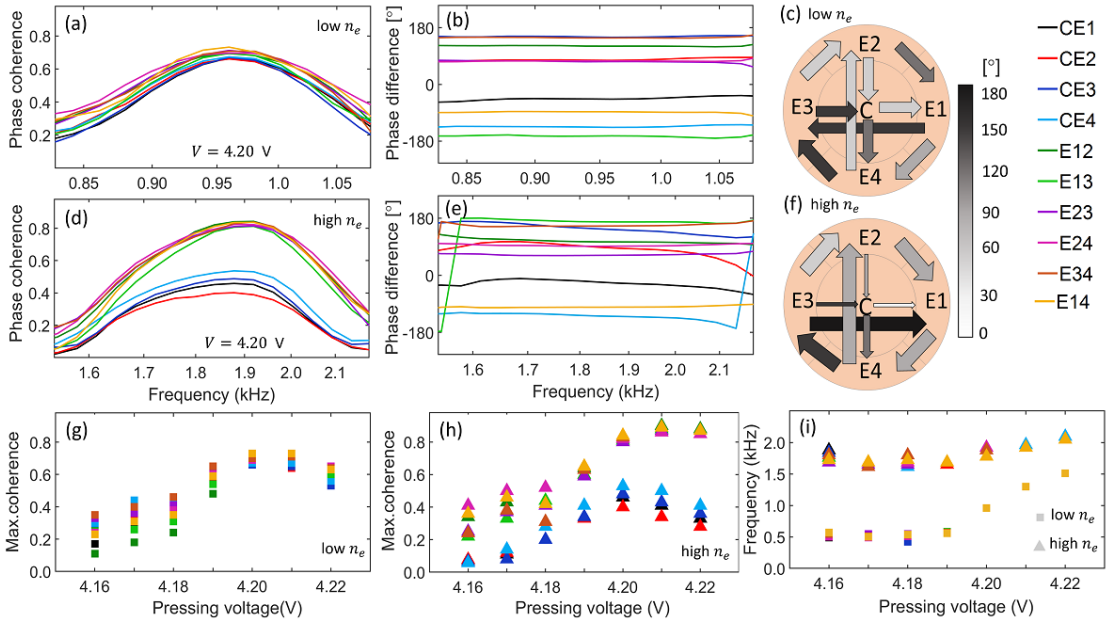

Figure 5.6: (a-b) Wavelet phase coherence and phase difference of pairs of electrodes for the lower electron density of $n_e = 1.4 \times 10^6$ cm^{-2} at a pressing voltage of $V = 4.20$ V for a fixed depth of liquid helium. High phase coherence is observed in the range of 0.85 - 1.05 kHz with a constant phase difference. (c) The circular schematic summarises the coherences and phases shifts between the currents. The thickness of the arrows indicates the magnitude of the coherence and the white/black shading the size of the phase shift. (d-f) Same as (a-c) but with the higher $n_e = 2.2 \times 10^6$ cm^{-2}. The lines are color-coded to indicate particular electrode pairs. (g-h) Maximum coherence values for all pairs of electrodes obtained at different V for both electron densities, showing that the resonance condition, i.e. similar coherence between all electrode pairs, is satisfied only at the lower n_e. (i) The change in frequency of the maximum coherence at each n_e value as functions of V for all electrode pairs.

all possible pairs of electrodes. Sec. 5.3.2 investigate the coupling strength between two oscillations, obtained over time, for both directions of coupling.

5.3.1 Phase coherence and phase shift

We have studied the mutual relationships of the current oscillations in the five electrodes by calculating the wavelet phase coherence and phase differences between different electrode pairs. The results for low and high n_e are shown in Figs. 5.6 (a-c) and (d-f), respectively, for $V = 4.20$ V. At low n_e, significant coherence was found for all electrode pairs for $V = 4.20$ V (Fig. 5.6 (a)). For high n_e at $V = 4.20$ V (Fig. 5.6 (d)), there is lower coherence between the central electrode and each of

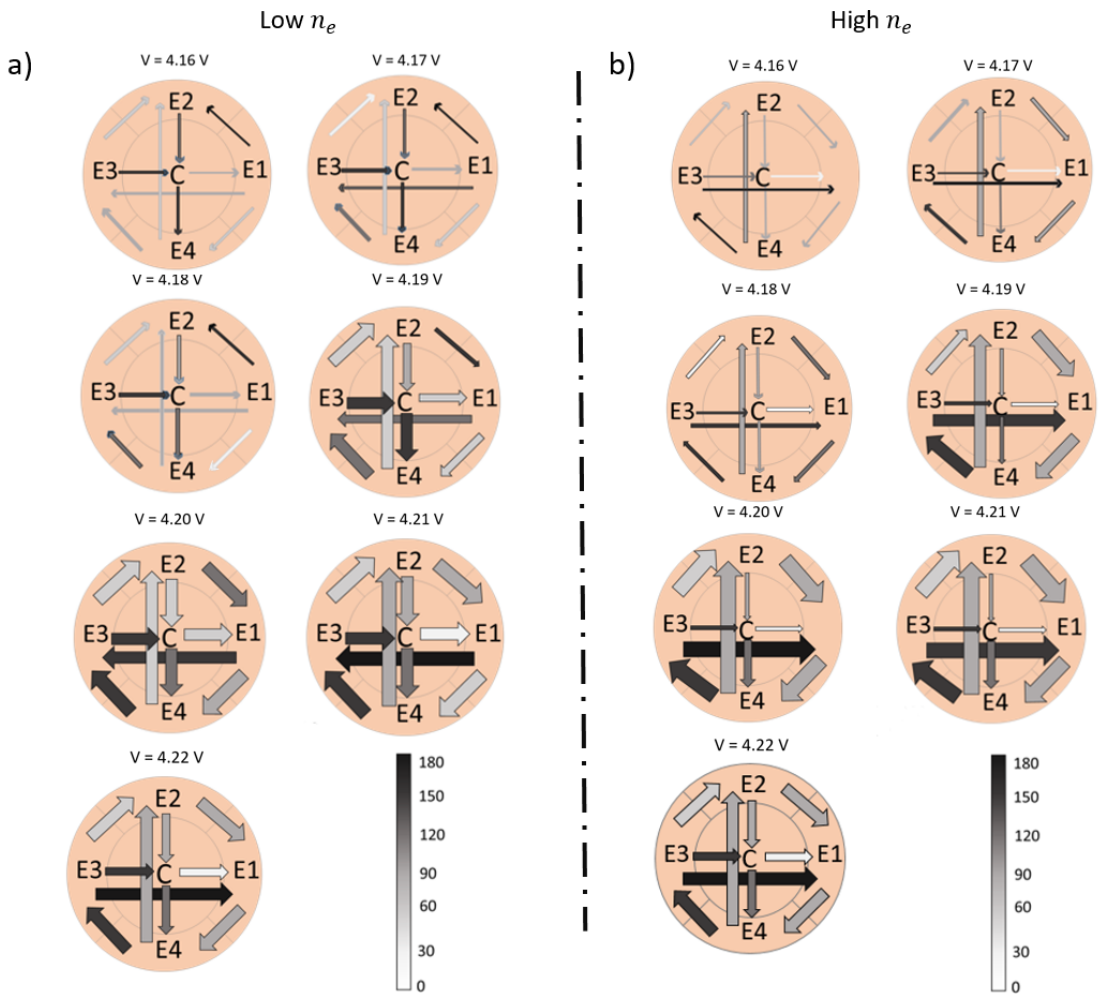

Figure 5.7: (a)-(b) The circular schematics show the motion of the electrons below the electrodes for different pressing voltages with low electron density $n_e = 1.4 \times 10^6$ cm^{-2} and high $n_e = 2.2 \times 10^6$ cm^{-2}, respectively. It summarises the coherences and phases shifts between the currents in the cell. The thickness of the arrows indicates the magnitude of the coherence. The white/black shading gives the size of the phase shift of the low and high electron densities n_e.

the edge electrodes, but high coherence when the edge electrodes are paired. It is clear from Fig. 5.6 (b) and (e), that the phase difference is constant for both low and high electron density around the frequency where maximal phase coherence occurs. For high n_e Fig. 5.6 (e) shows that some of the currents are almost in antiphase.

The most plausible explanation of the phase differences between the signals from differently-positioned electrodes is that there is a complex clockwise circumferential electron flow, and there are also flows towards and away from C: the circular schematics (c) and (f) illustrate the electron flow at the same $V = 4.20\,\mathrm{V}$ but at

different n_e. It is clear that changing n_e changes the flow pattern. At higher n_e, the flow is in the same direction for all values of V. At lown_e, we have three different patterns of motion (see Fig. 5.7). First, at pressing voltages 4.16 to 4.18 V, the motion is mainly in C, E3 and E4 part of the cell. For pressing voltages 4.19 to 4.21 V, it becomes more homogeneous and spans across the entire cell and motion at the edges becomes obvious. At the highest voltage 4.22 V, the direction of motion becomes the same as that observed at high n_e.

The complexity of the flow may in part be attributable to interaction between the electrons and gravity waves (see below). Fig. 5.6 (g,h) show that, for all paired electrodes, the maximum phase coherence changes with V for both n_e: (g) shows that, for low n_e, the resonance condition is satisfied at $V = 4.20$ V, implying that the coherence is uniform over the electrodes. Fig. 5.6 (i) shows that the frequency of maximum coherence changes with V at both electron densities, similarly to the behavior of the mean frequency of oscillation on each of the electrodes as shown in Fig. 5.5 (d).

5.3.2 Coupling and the direction of the motion for both electron densities

For each electrode (C, E1, E2, E3 and E4), dynamical Bayesian inference (DBI) was performed for all the possible combinations of their instantaneous frequencies, on oscillations obtained by ridge extraction (see Sec. 4.3.6) from the time-frequency representation.

As described above, DBI enables the coupling strength between two oscillations to be followed over time, for both directions of coupling and for both low and high electron densities while varying the pressing voltage from 4.16 V to 4.22 V. In Fig. 5.8, the black and the blue solid lines denote the results from DBI using the pairs of phases; and the dotted red lines are results obtained from surrogate data. Only values above the surrogate threshold are considered as significant as shown in Fig.5.8.

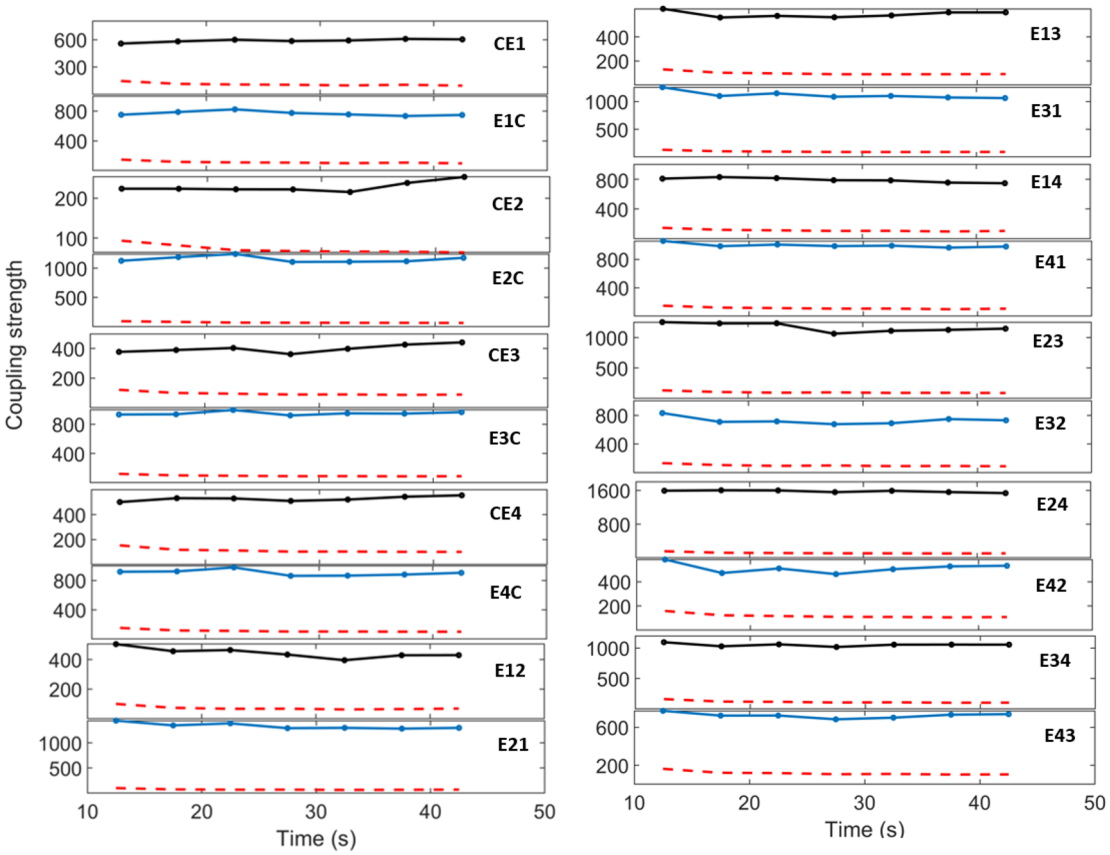

Figure 5.8: The coupling strength over time between five oscillations of signal from the C and four edge electrodes (oscillation C, E1, E2, E3 and E4), at a pressing voltage of $V = 4.20$ V and electron density $n_e = 1.4\times10^6$ cm^{-2}. The black and blue solid lines denote the coupling strength results over time for the five electrode pairs, obtained from dynamical Bayesian inference. The dotted red lines are the surrogate significance tests. Only results above the surrogate lines are significant. The couplings are computed within seven windows and we obtain seven points (solid circles).

Figs. 5.9 and 5.10 for the low and high electron densities, respectively, give the mean and standard deviation (SD) of the coupling strength for the significant results in both directions. The coupling directions CE3, CE4 and E43, and their reverse directions, show that the mean coupling strengths are much higher than for the other couplings at pressing voltages from $V = 4.16$ V to $V = 4.18$ V. For pressing voltages $V = 4.17$ V the couplings CE2, E12, E23 and E24, together with their reverse directions, gave no results with significance above the surrogate thresholds. However, there are finite coupling strengths for all electrode pairs, together with their reverse directions, from pressing voltages $V = 4.19$ V to $V = 4.21$ V; while, the values of mean coupling strength are reduced for all electrode pairs (and their

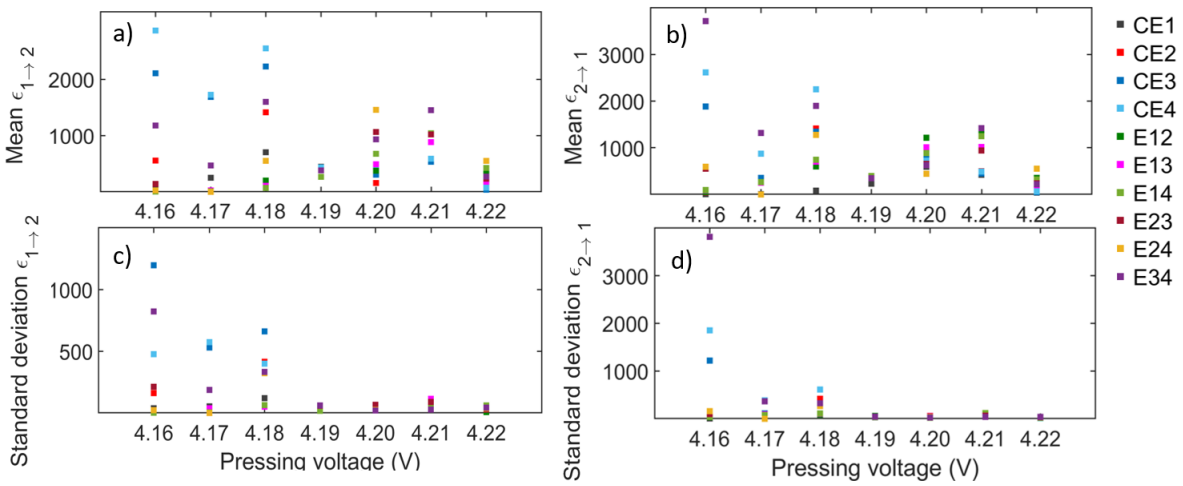

Figure 5.9: (a),(c) Mean and SD of coupling strength in direction 1→2, where 1 and 2 are electrodes as shown in the bar on the right hand side, where 1 indicates the first of the two electrodes in the pair, and 2 the second electrode. (b),(d) Mean and SD of coupling strength in direction 2→1. Shown are values for electron density $n_e = 1.4\times10^6$ cm^{-2}. Only values which are above the surrogate level are shown.

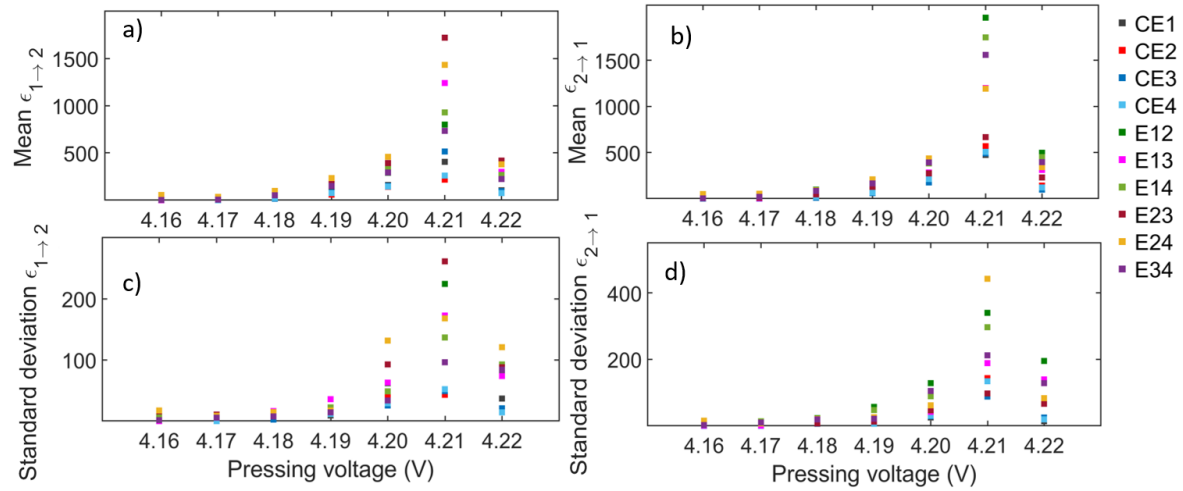

Figure 5.10: (a),(c) Mean and SD of coupling strength in direction 1→2, where 1 and 2 are electrodes as shown in the bar on the right hand side, where 1 indicates the first of the two electrodes in the pair, and 2 the second electrode. (b),(d) Mean and SD of coupling strength in direction 2→1. Shown are the values for electron density $n_e = 2.2\times10^6$ cm^{-2}. Only the values which are above the surrogate level are shown.

reverse directions) at the pressing voltage $V = 4.22$ V. Fig. 5.10 for high electron density, the coupling strengths for the significant results of all electrode pairs at different pressing voltages seem to be lower compared with those at low electron density. There are higher value of the coupling strength, for both directions, at

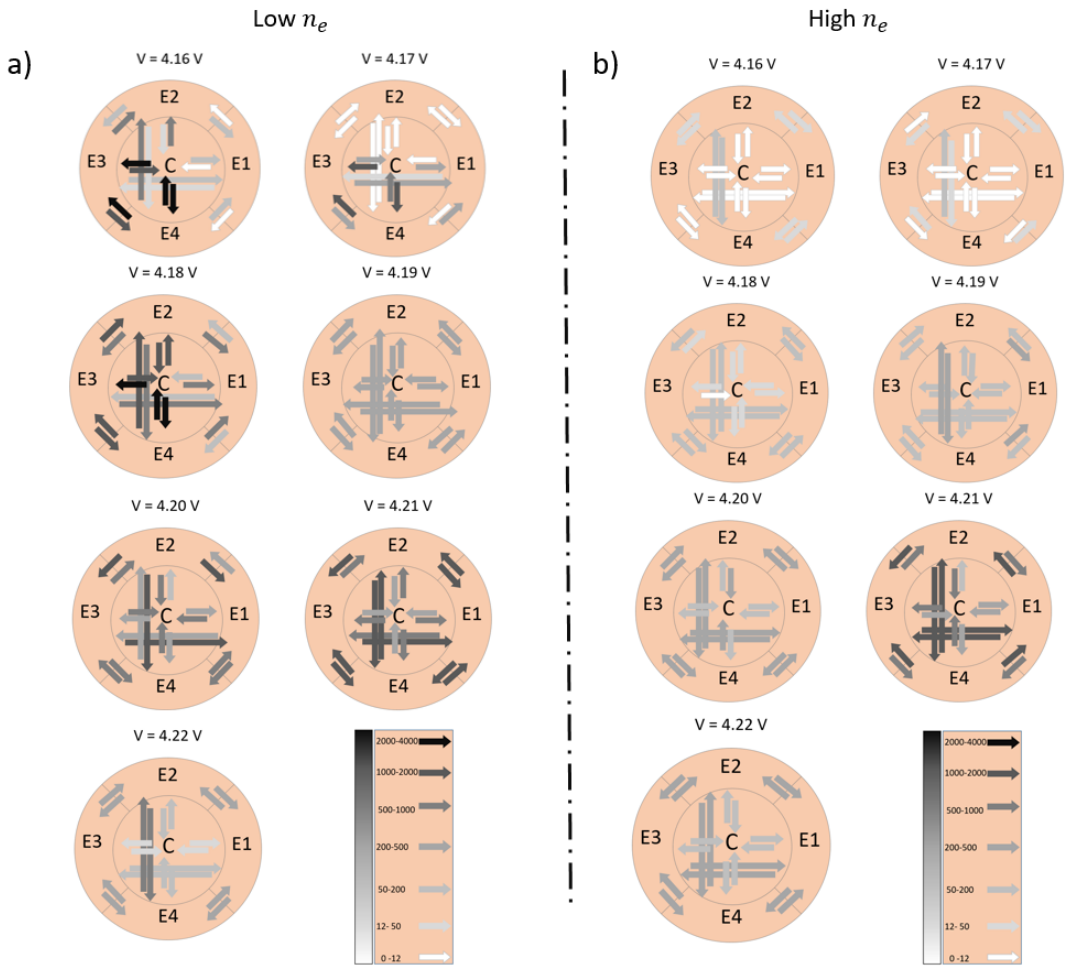

Figure 5.11: (a) (b) The direction of the coupling strength for both electron densities $n_e = 1.4{\times}10^6$ cm^{-2}, $n_e = 2.2{\times}10^6$ cm^{-2}, respectively, between the electrode pairs at different pressing voltages. The arrows indicate the direction of the coupling strength of electrode pairs where the white/black shading indicates the magnitude of the coupling strength.

the pressing voltage V=4.21 V than at other pressing voltages. Figs. 5.11 (a), (b) summarise the couplings computed between all electrode pairs for low and high electron density, respectively, at different pressing voltages. The arrows indicate the coupling directions for electrode pairs, while the white/black shading shows the magnitude of the mean coupling strength, which seems to be stronger at the lower electron density.

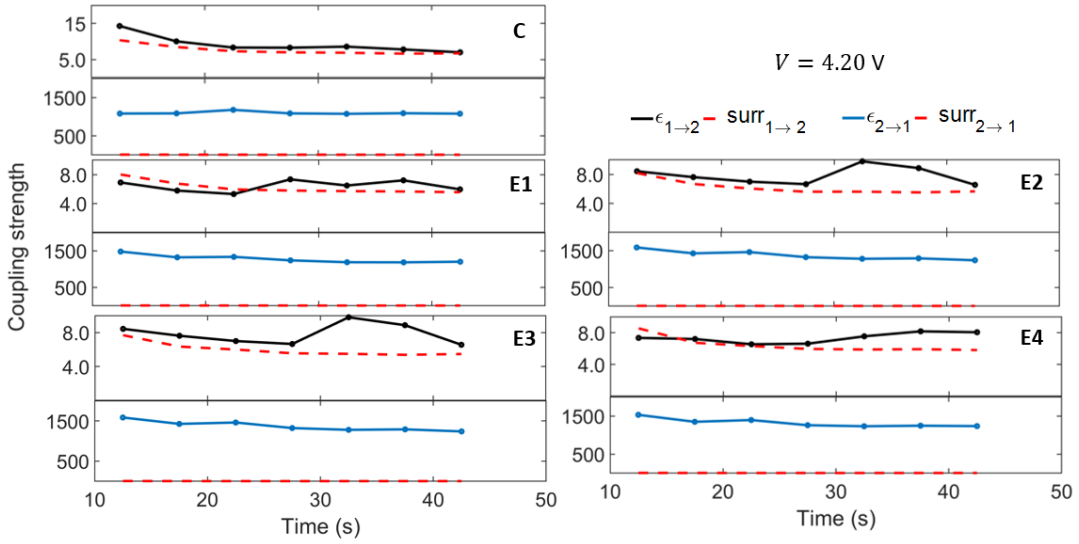

Figure 5.12: Identifying chronotaxicity using dynamical Bayesian inference. Bayesian inference was performed on φ_{x}^{*} and $\varphi_{\mathrm{x}}^{A*}$ extracted from signals of C and four edge electrodes. φ_{x}^{*} is the instantaneous frequency extracted from the wavelet transform with $f_0 = 3$ Hz, while $\varphi_{\mathrm{x}}^{A*}$ is the smoothed instantaneous frequency. The black solid lines denote the results from DBI using the pair of phases as (φ_{x}^{*} to φ_{x}^{A*}) which are indicated by $\epsilon_{1\to2}$. The blue solid lines denote the results from DBI using the pair of phases as φ_{x}^{A*} to φ_{x}^{*} which and indicate by $\epsilon_{2\to1}$. The dotted red lines are results obtained from surrogate data at a pressing voltage of $V = 4.20$ V and electron density $n_e = 1.4\times10^{6}$ cm^{-2}.

Coupling strength for $V = 4.20$ V																					
	($\epsilon_{1\to2}$)										($\epsilon_{2\to1}$)										
electrdoes	1	2	3	4	5	6	7	mean	median	SD	1	2	3	4	5	6	7	mean	median	SD
C	4	2	1	1	2	1	0	2	1	1	857	885	991	911	895	913	906	900	906	41
E1	0	0	0	2	1	2	0	1	0	1	1301	1176	1207	1121	1067	1070	1088	1147	1121	86
E2	0	1	1	1	4	3	1	2	1	1	1404	1280	1332	1199	1157	1167	1122	1237	1199	104
E3	1	1	1	1	4	3	1	2	1	1	1403	1291	1339	1199	1159	1171	1123	1241	1199	105
E4	0	0	0	1	2	2	2	1	1	1	1341	1212	1266	1137	1110	1127	1115	1187	1137	89

Table 5.2: The coupling results between oscillations φ_{x}^{*} and $\varphi_{\mathrm{x}}^{A*}$ with both direction for C, E1, E2, E3 and E4 electrodes with the mean, median and standard deviation. The coupling strengths are much higher in the direction $\epsilon_{2\to1}$ as shown in Fig. 5.12.

5.4 Is the system chronotaxic?

The dynamical Bayesian inference (DBI) method (see above) can be used to detect chronotaxicity. It involves extracting the perturbed ($\varphi_{\mathbf{x}}$) (extracted) and unperturbed ($\varphi_{\mathbf{x}}^{A}$) (obtained by smoothing) frequency estimates from the collected data in order to model their interaction. The time series should include at least

30 cycles of oscillation to test for chronotaxicity. The length of the signal that we used, was around 47 sec. The characteristics of the coupling functions between the extracted perturbed and unperturbed phases can reveal the dynamics of the system in terms of chronotaxicity. The ability of Bayesian inference to track time-dependent system parameters can be used to detect chronotaxicity in the system, which can move in and out of the chronotaxic state. To do that, Bayesian inference is applied to the two $\varphi^*_{\mathbf{x}}$ and $\varphi^{A*}_{\mathbf{x}}$ phases, following their extraction from the continuous wavelet transform, as described in Sec. 4.3.6. Then, DBI is used to determine simultaneously the coupling functions and their strengths between $\varphi_{\mathbf{x}}$ and $\varphi^{A}_{\mathbf{x}}$: see Sec. 4.3.8. We can infer uni-directional coupling between the unperturbed (obtained by smoothing) frequency and the perturbed (extracted) frequency. This indicates the presence of chronotaxicity. From DBI, the coupling strength between two oscillations is obtained over time, for both directions of coupling. The first coupling strength terms are in the direction (1→2) ($\epsilon_{1\to2}$) which means $\varphi^*_{\mathrm{x}} \to \varphi^{A*}_{\mathrm{x}}$, while the second coupling strength terms are in the direction (2→1) ($\epsilon_{2\to1}$) which means $\varphi^{A*}_{\mathrm{x}} \to \varphi^*_{\mathrm{x}}$. An example is shown in Fig. 5.12 for low electron density at pressing voltage $V = 4.20\,\mathrm{V}$. The black solid lines denote the results from DBI using the pair of oscillations φ^*_{x} and $\varphi^{A*}_{\mathrm{x}}$ presented with direction $\epsilon_{1\to2}$. The blue solid lines denote the coupling strength for the reverse direction represented by $\epsilon_{2\to1}$. The dotted red lines are results obtained from the surrogate data. Only the values above the surrogate levels are considered to be significant.

Table 5.2 gives the coupling strength results between oscillations φ^*_{x} and $\varphi^{A*}_{\mathrm{x}}$ for the significant results in both direction for all five electrodes with the mean, median and standard deviation. The coupling strengths are much higher in the direction $\epsilon_{2\to1}$ as shown in Fig. 5.12. The coupling results are similar for all electrodes at a pressing voltage $V = 4.20\,\mathrm{V}$ (see Fig. 5.12 especially for the direction $\epsilon_{2\to1}$ ($\varphi^{A*}_{\mathrm{x}} \to \varphi^*_{\mathrm{x}}$). There seems to be strong and stable coupling from $\varphi^{A*}_{\mathrm{x}}$ to φ^*_{x} which persists over time. In the reverse direction, the coupling is weaker and almost absent. Similar results were also obtained at a pressing voltage $V = 4.21\,\mathrm{V}$ at low

electron density. Therefore, the coupling strength at low electron density for the two pressing voltages $V = 4.20\,\mathrm{V}$ and $V = 4.21\,\mathrm{V}$ is seen to be stronger and stable from ($\varphi_{\mathrm{x}}^{A*}$ to φ_{x}^{*}). There is significant coupling strength in both directions, at different pressing voltages, for both electron densities, but that in the direction from φ_{x}^{*} to $\varphi_{\mathrm{x}}^{A*}$ is weaker and less stable.

6. Discussion

In this chapter, we present a comprehensive review and consideration of the experimental results described in chapter 5. Our aim is to provide the most plausible interpretation for our findings based on the data collected and analyzed, which we now summarize.

We revealed oscillatory electron motion of varying frequency (kHz) and showed that the characteristic frequencies change with electron density and pressing voltage. Then, we studied the time-averaged wavelet power to provide additional information about the distribution of electrons inside the cell, and how it changes at different electron densities and pressing voltages. After that, we extracted the ridges corresponding to the characteristic frequencies for each of the five currents at both electron densities, and at each pressing voltage. As a result, we detected a frequency modulation of $\sim$5 Hz in all cases and showed that it is almost independent of the pressing voltage, and varies very slightly with the electron density (5.2 Hz at low n_e and 5.1 Hz at high n_e, at the central electrode).

The coupling analysis revealed strong and weak phase couplings between pairs of signals, which was confirmed at different pressing voltages and electron densities. Application of DBI to the measured signals from the differently positioned electrodes allowed us to visualise the motion of electrons inside the cell. Similar values of coupling strength between the centre and the four edge electrodes in both directions was detected at the resonance pressing voltage, at both low and high electron densities, indicating uniform electron distribution. In short, we discuss in this chapter the nonlinear and nonautonomous dynamics of electrons on the

liquid helium surface, and study their interactions including phase coherence and couplings.

6.1 Conventional EMP vs. experimental data

Electrons are confined on the surface of liquid helium by applying a positive pressing voltage V to the bottom electrode plate as shown in Fig. 6.1. Owing to the linear Stark shift of the Rydberg levels (see Sec. 2.1.1) caused by an electric field $E_\perp$ applied perpendicular to the surface, the transition frequency of the SEs, $\omega_{21}(E_\perp) = (E_2 - E_1)/\hbar$, can be adjusted to match the microwave frequency ω_{MW} by varying the value of V.

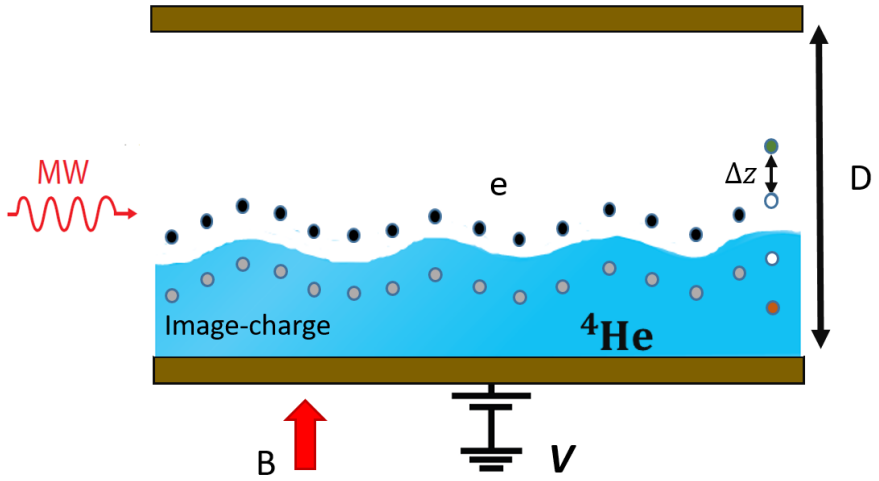

Figure 6.1: An electron floating above a liquid helium surface induces an image charge inside the helium. The MW-excited electrons (green circles) are elevated above the charged layer of the ground-state electrons by a distance $\Delta z_2 = z_{22}$-z_{11}, where z_{22} is the average value of the z coordinate (measured from the helium surface) of an electron occupying a Rydberg state of index n.

At low temperatures and in the absence of external drive, electrons tend to occupy the low energy levels due to the large energy gap between the ground and first excited states as compared to energy of thermal fluctuations, $\hbar\omega_{1,2} \gg k_B T$. As is well-known, in the presence of a homogeneous magnetic field $\mathbf{B} = (0, 0, \mathrm{B})$ applied along the z-axis, electrons confined to move in the xy-plane experience a Lorentz force given by $\mathbf{F} = e(\boldsymbol{v} \times \mathbf{B})$. Here, $\boldsymbol{v} = (v_x, v_y, 0)$ is the velocity of the

electron and e is its charge. This force is always perpendicular to the velocity $\boldsymbol{v}$ and acts as a centripetal force. The radius of the circular motion performed by each electron on the xy-plane, referred to as the cyclotron radius, is determined by the equation:

$$\frac{mv^2}{r_c} = evB, \tag{6.1}$$

which leads to

$$r_c = \frac{mv}{eB}. \tag{6.2}$$

In the case of a two-dimensional, nondegenerate system of noninteracting electrons, the thermal velocity v of each electron can be determined from the equipartition theorem, which states that each of the two available degrees of freedom has a mean kinetic energy of $k_BT/2$. The velocity is therefore given by:

$$\frac{1}{2}mv^2 = k_{\mathrm{B}}T \Longrightarrow \quad v = \sqrt{\frac{2k_{\mathrm{B}}T}{m}}. \tag{6.3}$$

The cyclotron radius r_c and cyclotron frequency ω_c, which describe the circular motion of electrons in a magnetic field, can also be calculated. The cyclotron radius is given by:

$$r_c = \frac{\sqrt{2\ mT}}{eB},$$

and the cyclotron frequency is:

$$\omega_{\mathrm{c}} = \frac{eB}{m}. \tag{6.4}$$

It is important to note that the physical interpretations of r_c and ω_c only hold for a classical electron gas, and not for any modified systems. In a static magnetic field $\mathbf{B} = B_z\mathbf{e}_z$ perpendicular to the surface, the in-plane motion of SEs is quantized into states of equidistant energy separation, known as Landau levels, which have energies of $\hbar\omega_c(l + 1/2)$, where l is a positive integer or zero.

In our experiments, the surface state electrons are exposed to a perpendicular magnetic field and resonant microwave radiation of frequency $\omega_{12} = 139$ GHz that excites intersubband transitions between the ground and first excited surface states.

The intersubband resonance condition is tuned by adjustment of the holding electric field that changes the gap between the two lowest surface bound states due to the Stark effect. In order to achieve the zero resistance regime, the vertical magnetic field is set to a value near $B = 0.8\,\mathrm{T}$. By fine adjustment of the magnetic field strength, the electronic energy levels can be optimized for creation of the zero resistance state. If the MWs are powerful enough, it is possible for the conductivity to become negative $\sigma < 0$. A negative conductivity implies that the electrons will move against the confining forces of the electrodes (displaced). Moreover, a nonzero signal ΔI [7], and a displacement of the surface charge are observed only in the intervals of the magnetic field near conductance minima. This suggests that the latter are linked to the transient current, as the presence of the magnetic field in these specific intervals is necessary for the observation of a nonzero signal. However, when the electrons are tuned away from the inter-subband resonance by changing the pressing voltage, no signal is observed. This further supports the idea of a relationship between the conductance minima and the transient current, as the absence of the minima results in the absence of the nonzero signal.

For a finite 2D electron system, if a strong perpendicular magnetic field is applied, and in addition, a parallel electric field is applied, current flows in the direction perpendicular to the electric field. At the edge, charges accumulate. This accumulation of charge produces an electric field parallel to the electron sheet, and then the current does not stop in the absence of dissipation. This is the EMP. The dissipation effect is suppressed because the electric field and current are almost perpendicular. With dissipation, the EMP will decay after some time. Therefore, even if there are fluctuations to excite edge magnetoplasmons, the average current remains small.

However, the negative conductivity induced in the 2D system by microwave irradiation means that a small fluctuation will be amplified. As in the stationary case, formation of a domain of two different electron densities is possible. The densities will be so determined that negative conductance would disappear because

of the resonance detuning. The negative conductance is sensitive to the electron density because the electron-electron interaction plays a role. After establishing the density domains, at the boundary there may be many possible dynamic modes in addition to the EMP, which could account for the observed self-generated currents [124]. No signal is observed when electrons are tuned away from the inter-subband resonance by changing V.

From our data, we have explored the characteristic features of the current oscillations induced in the five electrodes different electron densities and pressing voltages, at fixed magnetic field, depth of liquid helium and temperature. One of the main findings is:

- The electrons exhibit oscillations at approximately 1-2 kHz when subjected to driving at 139 GHz.

Based on these considerations, it appears highly probable that the 1–2 kHz oscillations observed for different electron densities may be caused by edge-magnetoplasmons (EMPs). According to the calculation by Volkov and Mikhailov [61], the EMP frequency is given by

$$\omega_{EMP} = 2\pi f_{EMP} = -\frac{q\sigma_{xy}}{2\pi\epsilon\epsilon_0}\Big(\ln|q|w + C_f\Big), \tag{6.5}$$

where $\sigma_{xy} \propto n_e/B$, the constant C_f depends on details of the density profile, w is the width of the transition layer, and q is the wavevector component along the boundary. This gives frequencies of ≈ 2.28 and 3.58 kHz for low and high electron densities, respectively, i.e. close to the values shown in Fig. 5.5(d) for different n_e. One of the specific characteristics of an EMP is that its frequency is proportional to the electron density n_e, inversely proportional to the magnetic field normal to the the surface of liquid helium and the wavelength of EMP. What we observe is very similar given that, as the electron density increases, the frequency also increases (Fig. 5.5 (d)).

6.2 Velocity of electrons

When a microwave field is applied to the system of electrons on helium, it can induce transitions between the energy levels (see Fig 6.1). The transition frequency is affected by the energy difference between the levels $E = E_2 - E_1$, which is influenced by the Stark effect. For the first excited state, $n = 2$, this distance is $\Delta z_2 \approx 35$ nm for $E_\perp = 0$, and somewhat decreases with increasing $E_\perp$ [39]. The reason behind the dependence of the oscillation frequency on the applied pressing voltage is as follows: at low electron densities, changes in the pressing voltage result in shifts of the energy levels, which in turn impact the transition frequency due to differences in the shifted levels. This explanation is supported by the findings of Andrei et al. [85].

The effect of the pressing voltage on the transition frequency depends on the relative strength of the electric field compared to the magnetic field, and the specific energy levels involved in the transition. In addition, the pressing voltage can change the frequency of oscillatory electrons on helium under microwave irradiation and magnetic field by affecting the trapping potential of the electrons. The trapping potential is created by applying a voltage to the electrodes beneath the helium surface, and it can confine the electrons to a specific region of the Corbino disk.

When the pressing voltage is increased, the trapping potential becomes stronger and the electrons will be confined to a smaller region, which causes the frequency of the magnetoplasmon modes to increase. An increase in the electron density can also affect the Landau level spacing. The energy spacing between the Landau levels is inversely proportional to the electron density, so when the electron density is increased, the energy spacing between the Landau levels will decrease. Then, the electron will move faster at higher electron density.

Also, the electrons experience strong Coulomb interactions (electron-electron), which can counteract the effect of the pressing voltage on the trapping potential and limit the change in frequency. Fig. 5.2 (d), shows how the mean oscillation

frequency for electrode C changes with V for different n_e. We note that the mean frequency starts to increase at $V = 4.19\,\mathrm{V}$ when the electron density is low with only a minimal difference between the maxima and minima of the oscillations (red shadow). For larger n_e, the mean frequency is higher and almost independent of V.

A noticeable difference between the maximum and minimum values of the oscillation frequency is observed to be larger in comparison to low electron densities. Indeed, the excitation of a portion of the SEs to the higher energy level results in the position change of the image charges for these SEs. The shift of the image charges for the excited SEs results in the variation of the force being exerted on the surface of liquid helium. This force variation causes the surface of liquid helium to move and alters the distance between the electron and the surface. This change in the distance between the electron and the surface could be responsible for the variation in the frequency range of the oscillations observed for different electron densities (low or high). In other words, the magnitude and direction of the image charge and its resulting force play a crucial role in determining the oscillation frequency range, making it dependent on the electron density.

Moreover, at high electron densities, the interaction between electrons also plays a significant role in determining the characteristics of the oscillations. This interaction between electrons can result in the changes of the magnitude and direction of the image charge and its resulting force, leading to alterations in the frequency range of the oscillations. Thus, both the image charge and electron-electron interaction contribute to the observed changes in oscillation frequency at high electron densities.

6.3 Electron interaction with the helium surface

Higher harmonics revealed through the analysis of the experimental data are attributable to a strong nonlinearity that is generated from the coupling between the liquid helium surface and the moving electrons. Ridges corresponding to the characteristic frequencies were extracted for each of the 5 currents, at both electron

densities, and at each pressing voltage [11]. By using the ridge extractions, a frequency modulation with $\sim 5\,\mathrm{Hz}$ was detected in all cases. The low frequency modulation that is revealed by the ridge extractions in Fig. 5.5 (a) and (b) and has an approximate value of 5 Hz can be considered a resonant frequency of the system being analysed. The fact that it is almost independent of the pressing voltage but slightly varies with electron density suggests that it is a fundamental frequency of the system, determined by its physical properties. The small difference in the average value at all pressing voltages in the C region, from 5.21 Hz at low electron density to 5.10 Hz at high electron density, highlights the sensitivity of this frequency to changes in the electron density (Fig. 5.5 (c)). Moreover, one possible explanation for the small fluctuation of this frequency is that it is modulated by an external factor, such as the magnetic field, microwave intensity or temperature.

The perpendicular electric field, $E_\perp = \frac{V}{D}$, exerts a vertical force on the sheet of electrons, and thus applies a pressure to the surface of the liquid helium. This causes a steady surface deformation that is proportional to the electron density and the pressing electric field. The surface depression was experimentally observed by Williams and Crandall [125]. Thus, the surface depression is intrinsic and can reach around 0.1 mm at high electron density n_e and pressing electric field $E_\perp$. Indeed, the pressing voltage can change the distribution of the electron charge and this will also induce a change in the surface depression.

Somewhat counter-intuitively, the electron charge decreases in the centre of the circular pool and increases in the edge regions, as we increase the pressing voltage. As the pressing voltage increases, the induced electric currents shift from the centre of the circular pool towards the edge regions, as indicated by our results from analysing the time-averaged wavelet power (see Fig. 5.2 (c)(d) and Figs. (5.3, 5.4). At low electron density ($n_e = 1.4\times10^6\ \mathrm{cm}^{-2}$), it seems that the electrons are mostly at the centre for low pressing voltages of (4.16 - 4.19) V, with some at the edge electrodes (E3, E4). Increasing the pressing voltage displaces the electrons from the centre towards the edges for $V = 4.21$ and $4.22\,\mathrm{V}$. However, with high

electron density ($n_e = 2.2\times10^6\,\mathrm{cm}^{-2}$) and low pressing voltage, the electrons are unaffected. This behaviour can be explained by the balance between the force induced by the electric field and the repulsive forces between the electrons. At high electron density, the repulsive forces between the electrons are stronger, causing them to resist motion in response to changes in the electric field. On the other hand, at low electron density, the repulsive forces are weaker, allowing the electrons to move more easily in response to changes in the electric field.

With increasing the pressing voltage, the electrons seem to crawl along the edge of the liquid surface. This suggests that the highest frequencies correspond to electrons moving predominantly below the edge electrodes, while the lower frequencies correspond to them moving mainly below the central electrode. These changes of the surface depression in the central and edge regions will not detune the electron system from the inter-subband resonance due to the corresponding corrections to the excitation energies, which can be about four orders of magnitude smaller than the typical linewidth γ_{mw} of the resonance caused by inhomogeneity of the electric field: $2\gamma_{\mathrm{mw}} \simeq 0.2\,\mathrm{GHz}$. The inhomogeneity can be larger in the edge area than in the centre of the electron pool. Under these conditions, the small increase in the width of the resonance may detune the displaced surface electrons from the inter-subband resonance in the edge region, and may lead to a vanishing of the negative conductivity. Therefore, the deformation effect can cause radial oscillations of electron density coupled with gravity waves.

During experiments with liquid helium, classical vibrations may be induced due to external excitation of the experimental setup, such as from the refrigerator or the laboratory environment. At temperatures above 0.3 K, the viscous damping in liquid helium is typically strong enough to quickly dampen these vibrations and minimize their impact on the experiments. However, a relatively high microwave power is used to obtain distinct oscillation recordings and to enhance the signal-to-noise ratio. Because this inevitably warms the cell, it makes it difficult to achieve stable operation at temperatures below 0.3 K. Therefore, these classical

vibrations can manifest as gravity waves. These waves stem from the disturbance of the surface and the accompanying changes in pressure, leading to the presence of excitatory interactions between the electrons and the gravity waves. This results in the modulation of the oscillation frequencies, as demonstrated in Figs. 5.2 (a) and (b).

Hence, the frequency modulation with a period of 0.2 s ($\sim$ 5 Hz) might arise from oscillations of electron density coupled with gravity waves [7, 27]: for radially symmetric modes, the lowest resonant frequency is $f \approx 0.609\ \sqrt{gd}/R$, where g is the acceleration due to gravity, and d and R are, respectively, the height and radius of the circular liquid pool [126]. This yields 5.28 Hz, comparable with the observations (see Table. 5.1). We suggest that a full theory of these phenomena will need to take explicit account of electron motion in the third (i.e. vertical) dimension. Although 2D electron motion will usually predominate over 3D, a 3D component of the electron motion certainly exists and may affect the currents detected by all electrodes.

6.4 Direction of electron motion

The most plausible explanation of the phase differences between the signals from the differently positioned electrodes is that there is a complex clockwise circumferential electron flow, and there are also flows towards and away from C: the circular schematics (Fig. 5.6) illustrate electron flow at different pressing voltages and electron densities. It is clear that changing n_e changes the flow pattern. The flow direction is independent of V at higher n_e, but dependent on it at lower n_e, The explanation for this phenomenon is discussed in Sec. 6.2.

The complexity of the flow may in part be attributed to the interaction between the electrons and the gravity waves. For all paired electrodes, we observe that the maximum phase coherence changes with V for both n_e values (Fig. 5.6 (g,h)): we show that, for low n_e, the resonance condition is satisfied at $V = 4.20$ V, implying that the coherence is uniform over the electrodes. The frequency of maximum

coherence changes with V at both electron densities, similarly to the behaviour of the mean frequency of oscillation on each of the electrodes (Fig. 5.5 (d)).

Coupling analysis of the ridge-extracted instantaneous frequencies revealed strong and weak phase coupling from the pairs of signals at different pressing voltages V and electron densities n_s (Fig. 5.11). The coupling strength for instantaneous frequencies between the differently-positioned electrodes using the DBI method helps us to reveal the motion of electrons inside the cell. A uniform electron distribution in the centre and four edge electrodes is noted at the resonance pressing voltage ($V = 4.20\,\mathrm{V}$ for low n_e and $V = 4.21\,\mathrm{V}$ for high n_e). Also, the higher coupling strength and uniform electron distribution are observed at $V = 4.21\,\mathrm{V}$ for low electron density. The higher coupling strength and uniform electron distribution at particular pressing voltages might indicate that the voltage is resonant with the energy level of the electrons, allowing for more efficient transfer of energy and distribution of electrons.

6.5 Chronotaxicity

Chronotaxicity may arise when oscillations are modulated [127]. The property of stability, or ability to resist external perturbations, is defined by the theory of chronotaxic systems [10, 84, 107, 116, 117] . Indeed, the analysis shows that there is strong and stable coupling strength in the direction from the unperturbed phase (smoothed frequency) to the perturbed phase (extracted frequency) for low electron density at the pressing voltage $V = 4.20\,\mathrm{V}$. This implies a motion of electrons on the surface of the liquid helium at these n_e and V, and that the system is chronotaxic.

At resonant pressing voltage, with low electron density, under microwave irradiation, the system is capable of maintaining the stability of these oscillations. Physically, this could be because the MW frequency (external driving force) matches the transition frequency (determined by the pressing voltage) and cyclotron frequency (determined by the strength of the magnetic field). Indeed, chronotaxicity refers to the ability of a system to accurately measure time or to have a sense of

time.

The term is used in various fields such as biology, neuroscience, and engineering to describe the ability of a system to measure time and the influence of time on the system's behaviour or function. In the context of biological systems, chronotaxicity refers to the ability of a system to respond in a stable way when perturbed and thus adjust its behaviour accordingly. In the context of engineering, chronotaxicity refers to the ability of a system to accurately measure time and to respond to time-dependent inputs. Chronotaxicity in the electron-on-helium system can be useful for understanding the dynamics of the electrons on the helium surface and how they respond to different inputs. It can also provide information about the stability of the system and the time scales of the electron's behaviour.

6.6 Summary

This section summarises the physics underlying the oscillations observed in the five electrodes for different electron densities and pressing voltages in a fixed magnetic field, within a liquid helium environment at a specific temperature. To examine the unique features of these oscillations, we employed a wavelet transform analysis. Higher harmonics resulted from the strong nonlinearity generated from the coupling of the liquid helium surface to the moving electrons. The ridge extraction technique was used to identify a modulation frequency of around 5 Hz. The electrons were found to oscillate at about 1-2 kHz in response to being driven at 139 GHz. At low electron density, the frequency depended on the pressing voltage, but not at high electron density.

The direction of electron motion in the cell was visualized through the use of phase coherence and phase shift methods. It was influenced by the applied pressing voltage, with the effect being more pronounced at low electron densities than at high electron densities. By using a dynamical Bayesian approach, we were able to detect the existence of chronotaxicity under resonant conditions in the system. At the resonant pressing voltage and low electron density, with microwave irradiation,

the system is able to maintain stability of its oscillations.

The observed phenomena appear to involve –

1. Magnetoplasmons. These were observed only in the presence of microwaves. Within the framework of nonlinear dynamics, the microwaves can be seen as acting as an external perturbation on the interacting electron-helium system.

2. Coupling between the electrons and the helium; it is modulated by the pressing voltage, via the image charge effect. The higher the voltage, the faster the electrons become un-trapped to move further, but this relationship is not linear, as will be explained in item 5 below.

3. Distinct directions of electron motion. From the phase coherence analyses, it is evident that the movement is more than just orbital motion at the edges of the cell, and that its direction depends on the direction of the magnetic field.

4. Velocity of electrons. The frequency of the magnetoplasmons is generally higher with the higher electron density. Hence, it may be concluded that the electron-electron interaction, which is stronger at higher electron density, is one of the main factors influencing the frequency of the magnetoplasmon, and hence the electronic velocity.

5. Chronotaxicity. This phenomenon arises in non-autonomous systems. Under the present experimental conditions, it results from the alignment of the frequency of the external driving force (MW) and the transition frequency of the Rydberg states. At resonance, the MW frequency and the cyclotron frequency of electrons become synchronized.

7. Conclusion

Through an extensive analysis of time traces of electric currents measured from five electrodes positioned above the surface of liquid ^{4}He, and while subjected to microwaves and a dc magnetic field, we utilized the wavelet transform and ridge extraction to determine that the measured signals exhibit periodicity with well-defined frequencies of 1-2 kHz for different electron densities and varying pressing voltages. These frequencies were observed to be modulated at a frequency of around 5 Hz. We conclude that the main kHz signals are generated by edge magnetoplasmons (which may be the origin of the observed self-generated currents) [61] modulated by interaction with gravity waves at about 5 Hz [7, 34].

Based on our analysis, the electrons are moving in the cell with various velocities and in various directions in a complex oscillatory manner, occupying 3D space. These results may be derived from the most perfect example of a classical (the observed self-generated currents may be understood as a classical motion), rather than a quantum, 2D electron system. Indeed, our use of segmented electrodes, combined with the time-frequency analysis, has illuminated the dynamics of the surface electrons.

If the power spectral densities alone were calculated for the signals, they would mostly look much like white noise, with some peaks that are broad. Adding the time dimension enabled the varying frequency to be followed and brought new insight. We found that increasing V changed the pattern of phase differences and coherence between the signals induced at the differently-positioned electrodes. Moreover, based on the phase coherence method we emphasize that the resonance

condition is met at a characteristic pressing voltages ($V = 4.20\,\mathrm{V}$) for low electron density.

Coupling analysis enabled us to detect the motion of electrons between the electrodes inside the cell, with high accuracy. Using dynamical Bayesian inference, we were able to infer uni-directional coupling from the unperturbed (obtained by smoothing) frequency to the perturbed (extracted) frequency, indicating the presence of chronotaxicity. Physically, this could occur because the frequency of the MW (external driving force) matches the transition frequency between the Rydberd states, (determined by the pressing field). Also, at resonance, the electron cyclotron frequency and the microwave frequencies were synchronized, so that electrons were continuously accelerated by the electric field.

Thus, treating the time-resolved dynamics with logarithmic frequency resolution, has opened up new possibilities for understanding these paradigmatic far-from-equilibrium phenomena, bringing together the quantum and classical processes involved. So far, chronotaxic dynamics has been observed mainly in living systems that exhibit oscillatory dynamics on many time and size scales – from the cellular scale [10, 40, 41], up to system, and population scales – but allowing only very limited possibilities for studying experimentally the effect of changing relevant parameter values. Unlike observational studies in biology, the experiments on superfluid helium provide a chance to comprehend chronotaxic behavior through rigorously controlled laboratory investigations that have the potential to uncover the connection between the physical world and the fundamental essence of chronotaxic dynamics. These studies could be pioneers in establishing the characteristics of a designed open non-autonomous system, which allows for a direct correlation between the microscopic actions of its components and their collective macroscopic behavior.

The electron-on-helium system is a valuable tool for investigating similar phenomena in biological systems. Its simplicity provides a higher degree of control over experimental conditions and allows for a more focused examination of specific

aspects. Measuring the response of electrons to changes in microwave, magnetic fields, and pressing voltage over time can serve as a model for exploring the response of biological systems to stimuli. Measuring the distribution of electrons on the helium surface can also provide information on the temporal dynamics of biological systems.

The stability of the electron-on-helium system at various pressing voltage and electron density under certain conditions (resonance), makes it a promising platform for quantum computing. Its well-controlled and predictable environment provides a valuable advantage for quantum information processing.

7.1 Original contributions

The original contributions of this work are listed below:

- It was shown that the measured signals, induced in five Corbino electrodes by the spontaneous oscillation of surface electrons on liquid helium just below them, at low temperature, with a perpendicular magnetic field and microwave radiation, are not noise. These signals represent significant features and contain important information about the system of electrons.

- The frequencies of five signals, one from each electrode, were extracted as a function of time. It was shown that, for data measured simultaneously, the frequencies are identical.

- It was shown that the signals contain a higher harmonic with a frequency equal to twice the main frequency.

- Oscillations in the kHz range were observed at both electron densities (low and high) and at different pressing voltages. It was plausibly demonstrated that they were generated by edge magnetoplasmons. Their frequency was dependent on the electron density. It was found to increase with changes in

the pressing voltage at low electron density; but, at high n_e, it was shown to be independent of the pressing voltage.

- Variability of the frequency at different pressing voltages and electron densities was demonstrated for the first time, by using the wavelet transform. The time-averaged wavelet power provided additional information about the distribution of electrons inside the cell, and how it changes under different conditions of electron density and pressing voltage.

- Ridge extractions, obtained from the time-frequency representations of the signals, showed for first time that there are instantaneous frequency variations of the main component, but with a constant modulation frequency. The constant modulation frequency is attributed to the surface of the liquid helium not being flat and to the interaction between the electrons and gravity waves on the surface.

- Significant phase coherence was found between the current oscillations in each electrode pair, for each electron density. Maximum coherence values for all pairs of electrodes were obtained at different V for both electron densities. It was shown that the resonance condition, i.e. similar coherence between all electrode pairs, is satisfied only at the lower n_e for the pressing voltage $V = 4.20$ V. Information about the phase difference was used to reveal the motion of electrons between all the electrodes inside the cell, at different pressing voltages and electron densities.

- The directions of coupling between pairs of electrodes, and the corresponding coupling strengths, were found for both electron densities at different pressing voltages and used to reveal the electron motion between electrodes. It was found that the coupling strength between pairs of electrodes is stronger at low electron density; for high electron density, it was only stronger at the resonance pressing voltage $V = 4.21$ V.

- The inverse approach for the detection of chronotaxicity was applied to our

data for the first time. The analysis provided evidence of chronotaxicity: there is strong and stable coupling from the unperturbed phase (smoothed frequency) to the perturbed phase (extracted frequency) at the resonant pressing voltage ($V = 4.20\,\mathrm{V}$ for low electron density). Motion of electrons on the surface of liquid helium show that they constitute systems that, for low electron density and a specific pressing voltage, are capable of maintaining their stability in the face of continuous external driving (MW).

7.2 Future work

The work presented in this thesis provides the first evidence of interaction between the electrons and surface ripplons (~ 5 Hz), with the latter requiring consideration of the third dimension. In order to identify the contribution from the 3D motion of electrons, it is necessary to solve a problem with an electric potential (Poisson equation) including charge redistribution by mobility. Such a system of electrons on helium may, however, need to be treated as a non-isolated non-autonomous system (open system). Moreover, current measurements at different liquid helium levels might help to establish the resultant changes in the motion of the electrons inside the cell. Creating a model of the interaction between electrons and the surface of liquid helium in the presence of a perpendicular magnetic field and microwave radiation, is another goal, seeking more information about the nature of the interactions within the cell. To do so, we would aim to use the same methodology as was used in this work, but with some modifications e.g. to enable the liquid helium level to be adjusted, as well as exploring in more detail how the phenomena change with electron densities.

In contrast to the observational studies in biology, the superfluid helium experiments offer an opportunity to gain an understanding of chronotaxic behaviour based on well-controlled laboratory investigations that promise to reveal fully the relationship between the physical world and the fundamental nature of chronotaxic dynamics. New studies could be aiming at establishing directly the link between the

characteristics of an experimentally-designed, open, non-autonomous system and the microscopic behaviour of its elements together with their collective, macroscopic, behaviour.

References

[1] H. Byeon, *Studying electrons on helium via surface acoustic wave techniques*. Michigan State University, 2020.

[2] C. Grimes, T. Brown, M. L. Burns, and C. Zipfel, "Spectroscopy of electrons in image-potential-induced surface states outside liquid helium," *Phys Rev B*, vol. 13, no. 1, p. 140, 1976.

[3] Y. P. Monarkha and K. Kono, *Two-dimensional Coulomb liquids and solids*, vol. 142. Springer, 2004.

[4] S. Yamanaka, *Damping of novel edge-excitation in a two-dimensional electron system on liquid helium.* PhD thesis, Graduate School of Sciences, 2011.

[5] K. Shirahama, S. Ito, H. Suto, and K. Kono, "Surface study of liquid ^{3}He. using surface state electrons," *J Low Temp Phys*, vol. 101, no. 3, pp. 439–444, 1995.

[6] K. Nasyedkin and K. Kono, "Dynamics of surface state electrons on liquid helium exposed to microwave intersubband excitation and quantizing magnetic field," in *International Symposium on Dynamics in Artificial Quantum Systems*, p. P32, Jan. 2016.

[7] Y. P. Monarkha and D. Konstantinov, "Magneto-oscillations and anomalous current states in a photoexcited electron gas on liquid helium," *J Low Temp Phys*, vol. 197, no. 3, pp. 208–249, 2019.

[8] D. Konstantinov, A. Chepelianskii, and K. Kono, "Resonant photovoltaic effect in surface state electrons on liquid helium," *J Phys Soc Jpn*, vol. 81, no. 9, p. 093601, 2012.

[9] P. T. Clemson and A. Stefanovska, "Discerning non-autonomous dynamics," *Phys Rep*, vol. 542, no. 4, pp. 297–368, 2014.

[10] Y. F. Suprunenko, P. T. Clemson, and A. Stefanovska, "Chronotaxic systems: A new class of self-sustained nonautonomous oscillators," *Phys Rev Lett*, vol. 111, p. 024101, Jul 2013.

[11] D. Iatsenko, P. V. E. McClintock, and A. Stefanovska, "Extraction of instantaneous frequencies from ridges in time–frequency representations of signals," *Signal. Processing*, vol. 125, pp. 290–303, 2016.

[12] T. Arai, S. Yamanaka, H. Yayama, A. Sawada, and A. Fukuda, "Linewidth broadening in edge-magnetoplasmon resonance of helium surface state electrons," in *Journal of Physics: Conference Series*, vol. 400, p. 042001, IOP Publishing, 2012.

[13] M. W. Cole, "Electronic surface states of liquid helium," *Rev Mod Phys*, vol. 46, no. 3, p. 451, 1974.

[14] M. Zudov, R. Du, J. Simmons, and J. Reno, "Shubnikov–de Haas-like oscillations in millimeterwave photoconductivity in a high-mobility two-dimensional electron gas," *Phys Rev B*, vol. 64, no. 20, p. 201311, 2001.

[15] M. W. Cole and M. H. Cohen, "Image-potential-induced surface bands in insulators," *Phys Rev Lett*, vol. 23, no. 21, p. 1238, 1969.

[16] R. Williams and R. Crandall, "Deformation of the surface of liquid helium by electrons," *Phys Lett A*, vol. 36, no. 1, pp. 35–36, 1971.

[17] D. Glattli, E. Andrei, G. Deville, J. Poitrenaud, and F. Williams, "Dynamical

hall effect in a two-dimensional classical plasma," *Phys Rev Lett*, vol. 54, no. 15, p. 1710, 1985.

[18] D. Mast, A. Dahm, and A. Fetter, "Observation of bulk and edge magnetoplasmons in a two-dimensional electron fluid," *Phys Rev Lett*, vol. 54, no. 15, p. 1706, 1985.

[19] I. Grodnensky, D. Heitmann, K. Von Klitzing, and A. Y. Kamaev, "Dynamical response of a two-dimensional electron system in a strong magnetic field," *Phys Rev B*, vol. 44, no. 4, p. 1946, 1991.

[20] M. Dykman, K. Kono, D. Konstantinov, and M. Lea, "Ripplonic lamb shift for electrons on liquid helium," *Phys Rev Lett*, vol. 119, no. 25, p. 256802, 2017.

[21] K. M. Yunusova, D. Konstantinov, H. Bouchiat, and A. Chepelianskii, "Coupling between rydberg states and landau levels of electrons trapped on liquid helium," *Phys Rev Lett*, vol. 122, no. 17, p. 176802, 2019.

[22] P. Platzman and M. Dykman, "Quantum computing with electrons floating on liquid helium," *Science*, vol. 284, no. 5422, pp. 1967–1969, 1999.

[23] D. Schuster, A. Fragner, M. Dykman, S. Lyon, and R. Schoelkopf, "Proposal for manipulating and detecting spin and orbital states of trapped electrons on helium using cavity quantum electrodynamics," *Phys Rev Lett*, vol. 105, no. 4, p. 040503, 2010.

[24] G. Koolstra, G. Yang, and D. I. Schuster, "Coupling a single electron on superfluid helium to a superconducting resonator," *Nat Commun*, vol. 10, no. 1, p. 5323, 2019.

[25] A. D. Chepelianskii, M. Watanabe, K. Nasyedkin, K. Kono, and D. Konstantinov, "An incompressible state of a photo-excited electron gas," *Nat Commun*, vol. 6, no. 1, pp. 1–7, 2015.

[26] Y. P. Monarkha, "Density domains of a photo-excited electron gas on liquid helium," *Low Temperature Physics*, vol. 42, no. 6, pp. 441–445, 2016.

[27] D. Konstantinov and K. Kono, "Photon-induced vanishing of magnetoconductance in 2D electrons on liquid helium," *Phys Rev Lett*, vol. 105, no. 22, p. 226801, 2010.

[28] Y. P. Monarkha, "Microwave-resonance-induced magnetooscillations and vanishing resistance states in multisubband two-dimensional electron systems," *Low Temperature Physics*, vol. 37, no. 8, pp. 655–666, 2011.

[29] D. Konstantinov and K. Kono, "Novel radiation-induced magnetoresistance oscillations in a nondegenerate two-dimensional electron system on liquid helium," *Phys Rev Lett*, vol. 103, no. 26, p. 266808, 2009.

[30] H. Ikegami, H. Akimoto, D. G. Rees, and K. Kono, "Evidence for reentrant melting in a quasi-one-dimensional wigner crystal," *Phys Rev Lett*, vol. 109, no. 23, p. 236802, 2012.

[31] D. G. Rees, N. R. Beysengulov, J.-J. Lin, and K. Kono, "Stick-slip motion of the wigner solid on liquid helium," *Phys Rev Lett*, vol. 116, no. 20, p. 206801, 2016.

[32] E. Collin, W. Bailey, P. Fozooni, P. Frayne, P. Glasson, K. Harrabi, M. J. Lea, and G. Papageorgiou, "Microwave saturation of the Rydberg states of electrons on helium," *Phys Rev Lett*, vol. 89, no. 24, p. 245301, 2002.

[33] H. Isshiki, D. Konstantinov, H. Akimoto, K. Shirahama, and K. Kono, "Microwave absorption of surface-state electrons on liquid ^{3}He," *J Phys Soc Jpn*, vol. 76, no. 9, p. 094704, 2007.

[34] D. Konstantinov, M. Watanabe, and K. Kono, "Self-generated audio-frequency oscillations in 2D electrons with nonequilibrium carrier distribution on liquid helium," *J Phys Soc Jpn*, vol. 82, no. 7, p. 075002, 2013.

[35] A. Zadorozhko, Y. P. Monarkha, and D. Konstantinov, "Circular-polarization-dependent study of microwave-induced conductivity oscillations in a two-dimensional electron gas on liquid helium," *Phys Rev Lett*, vol. 120, no. 4, p. 046802, 2018.

[36] E. Kawakami, A. Elarabi, and D. Konstantinov, "Image-charge detection of the Rydberg states of surface electrons on liquid helium," *Phys Rev Lett*, vol. 123, no. 8, p. 086801, 2019.

[37] M. A. Nielsen and I. L. Chuang, "Quantum computation and quantum information," *Phys Today*, vol. 54, no. 2, p. 60, 2001.

[38] A. Dahm, J. Goodkind, I. Karakurt, and S. Pilla, "Using electrons on liquid helium for quantum computing," *J Low Temp Phys*, vol. 126, pp. 709–718, 2002.

[39] M. Dykman, P. Platzman, and P. Seddighrad, "Qubits with electrons on liquid helium," *Phys Rev B*, vol. 67, no. 15, p. 155402, 2003.

[40] G. Lancaster, Y. F. Suprunenko, K. Jenkins, and A. Stefanovska, "Modelling chronotaxicity of cellular energy metabolism to facilitate the identification of altered metabolic states," *Sci Rep*, vol. 6, no. 1, pp. 1–12, 2016.

[41] M. Morris, S. Yamazaki, and A. Stefanovska, "Multiscale time-resolved analysis reveals remaining behavioral rhythms in mice without canonical circadian clocks," *J. Biol Rhythms*, vol. 37, no. 3, pp. 310–328, 2022.

[42] M. Dykman, O. Asban, Q. Chen, D. Jin, and S. Lyon, "Spin dynamics in quantum dots on liquid helium," *Phys Rev B*, vol. 107, no. 3, p. 035437, 2023.

[43] D. Iatsenko, P. V. E. McClintock, and A. Stefanovska, "Nonlinear mode decomposition: a noise-robust, adaptive decomposition method," *Phys Rev E*, vol. 92, no. 3, p. 032916, 2015.

[44] P. T. Clemson, G. Lancaster, and A. Stefanovska, "Reconstructing time-dependent dynamics," *Processing. IEEE*, vol. 104, no. 2, pp. 223–241, 2016.

[45] L. W. Sheppard, A. Stefanovska, and P. V. E. McClintock, "Testing for time-localized coherence in bivariate data," *Phys Rev E*, vol. 85, no. 4, p. 046205, 2012.

[46] T. Stankovski, T. Pereira, P. V. E. McClintock, and A. Stefanovska, "Coupling functions: universal insights into dynamical interaction mechanisms," *Rev Mod Phys*, vol. 89, no. 4, p. 045001, 2017.

[47] M. A. Woolf and G. Rayfield, "Energy of negative ions in liquid helium by photoelectric injection," *Phys Rev Lett*, vol. 15, no. 6, p. 235, 1965.

[48] W. Sommer, "Liquid helium as a barrier to electrons," *Phys Rev Lett*, vol. 12, no. 11, p. 271, 1964.

[49] V. Shikin, "Motion of helium ions near a vapor-liquid surface," *Sov Phys JETP*, vol. 31, no. 936, p. 3, 1970.

[50] A. A. Fragner, *Circuit quantum electrodynamics with electrons on helium*. Yale University, 2013.

[51] T. Sanders Jr and G. Weinreich, "Energies of external electron surface states on liquid helium," *Phys Rev B*, vol. 13, no. 11, p. 4810, 1976.

[52] M. Saitoh, "Warm electrons on the liquid ^{4}He surface," *J Phys Soc Jpn*, vol. 42, no. 1, pp. 201–209, 1977.

[53] C. Grimes and T. Brown, "Direct spectroscopic observation of electrons in image-potential states outside liquid helium," *Phys Rev Lett*, vol. 32, no. 6, p. 280, 1974.

[54] L. D. Landau and E. M. Lifshitz, *Course of theoretical physics*. Elsevier, 2013.

[55] D. S. Drumheller, *Introduction to wave propagation in nonlinear fluids and solids*. Cambridge University Press, 1998.

[56] K. Birdi, *Surface tension and interfacial tension of liquids*. CRC: New York, 1997.

[57] O. Darrigol, "The spirited horse, the engineer, and the mathematician: water waves in nineteenth-century hydrodynamics," *Arch Hist Exact Sci*, vol. 58, no. 1, pp. 21–95, 2003.

[58] T. N. Theis, "Plasmons in inversion layers," *Surf Sci*, vol. 98, no. 1-3, pp. 515–532, 1980.

[59] L. Wilen and R. Giannetta, "Impedance methods for surface state electrons," *J Low Temp Phys*, vol. 72, no. 5, pp. 353–369, 1988.

[60] V. Volkov and S. A. Mikhailov, "Theory of edge magnetoplasmons in a two-dimensional electron gas," *JETP Lett*, vol. 42, no. 11, 1985.

[61] V. A. Volkov and S. A. Mikhailov, "Electrodynamics of two-dimensional electron systems in high magnetic fields," in *Modern Problems in Condensed Matter Sciences*, vol. 27, pp. 855–907, Elsevier, 1991.

[62] M. Lea, A. Stone, P. Fozooni, and J. Frost, "The ac response of a 2-d electron gas on liquid helium in a magnetic field," *J Low Temp Phys*, vol. 85, no. 1, pp. 67–89, 1991.

[63] V. Volkov and S. A. Mikhailov, "Edge magnetoplasmons: low-frequency weakly damped excitations in inhomogeneous two-dimensional electron systems," *Zh Eksp Teor Fiz*, vol. 94, pp. 217–241, 1988.

[64] S. A. Mikhailov and V. Volkov, "Inter-edge magnetoplasmons in inhomogeneous two-dimensional electron systems," *J Condens Matter Phys*, vol. 4, no. 31, p. 6523, 1992.

[65] R. Van Der Heijden and P. Sommerfeld, "Collective excitations in high magnetic fields," *Two-Dimensional Electron Systems: on Helium and other Cryogenic Substrates*, pp. 157–174, 1997.

[66] P. Sommerfeld, P. Steijaert, P. Peters, and R. Van der Heijden, "Magnetoplasmons at boundaries between two-dimensional electron systems," *Phys Rev Lett*, vol. 74, no. 13, p. 2559, 1995.

[67] O. Kirichek and I. Berkutov, "Magnetoplasmons in a system of surface electrons in helium at a boundary between regions with different charge densities," *Fizika Nizkikh Temperatur*, vol. 21, no. 4, pp. 394–396, 1995.

[68] A. Valkering, P. Sommerfeld, and R. Van der Heijden, "Effect of the classical electron coulomb crystal on interedge magnetoplasmons," *Phys Rev B*, vol. 58, no. 7, p. 4138, 1998.

[69] T. Brown and C. Grimes, "Observation of cyclotron resonance in surface-bound electrons on liquid helium," *Phys Rev Lett*, vol. 29, no. 18, p. 1233, 1972.

[70] A. Rybalko and Y. Z. Kovdrya, "Mobility of electrons along the liquid helium surface in strong retarding electric fields," *J Low Temp Phys*, vol. 18, no. 3, pp. 219–227, 1975.

[71] F. Bridges and J. McGill, "Mobility of electrons on the surface of liquid helium," *Phys Rev B*, vol. 15, no. 3, p. 1324, 1977.

[72] A. Rybalko, Y. Z. Kovdrya, and B. Esel'Son, "Electron mobility near the surface of liquid helium at temperatures down to 0.5 K," *ZhETF Pisma Redaktsiiu*, vol. 22, p. 569, 1975.

[73] C. Grimes and G. Adams, "Evidence for a liquid-to-crystal phase transition in a classical, two-dimensional sheet of electrons," *Phys Rev Lett*, vol. 42, no. 12, p. 795, 1979.

[74] P. Ye, L. Engel, D. Tsui, J. Simmons, J. Wendt, G. Vawter, and J. Reno, "Giant microwave photoresistance of two-dimensional electron gas," *Appl Phys Lett*, vol. 79, no. 14, pp. 2193–2195, 2001.

[75] R. G. Mani, J. H. Smet, K. von Klitzing, V. Narayanamurti, W. B. Johnson, and V. Umansky, "Zero-resistance states induced by electromagnetic-wave excitation in GaAs/AlGaAsheterostructures," *Nature*, vol. 420, no. 6916, pp. 646–650, 2002.

[76] M. Zudov, R. Du, L. Pfeiffer, and K. West, "Evidence for a new dissipationless effect in 2D electronic transport," *Phys Rev Lett*, vol. 90, no. 4, p. 046807, 2003.

[77] A. Andreev, I. Aleiner, and A. Millis, "Dynamical symmetry breaking as the origin of the zero-dc-resistance state in an ac-driven system," *Phys Rev Lett*, vol. 91, no. 5, p. 056803, 2003.

[78] V. Ryzhii, A. Chaplik, and R. Suris, "Absolute negative conductivity and zero-resistance states in two-dimensional electron systems: A plausible scenario," *J Exp Theor Phys*, vol. 80, no. 5, pp. 363–366, 2004.

[79] A. C. Durst, S. Sachdev, N. Read, and S. Girvin, "Radiation-induced magnetoresistance oscillations in a 2D electron gas," *Physica E Low Dimens Syst Nanostruc*, vol. 20, no. 1-2, pp. 117–122, 2003.

[80] I. Dmitriev, A. Mirlin, and D. Polyakov, "Cyclotron-resonance harmonics in the ac response of a 2D electron gas with smooth disorder," *Phys Rev Lett*, vol. 91, no. 22, p. 226802, 2003.

[81] I. Dmitriev, A. Mirlin, D. Polyakov, and M. Zudov, "Nonequilibrium phenomena in high landau levels," *Rev Mod Phys*, vol. 84, no. 4, p. 1709, 2012.

[82] Y. P. Monarkha, "Coulombic effects on magnetoconductivity oscillations induced by microwave excitation in multisubband two-dimensional electron systems," *Low Temperature Physics*, vol. 38, no. 6, pp. 451–458, 2012.

[83] Y. P. Monarkha, "Microwave-induced magnetooscillations and absolute negative conductivity in a multisubband two-dimensional electron system on liquid helium," *Low Temperature Physics*, vol. 37, no. 1, pp. 90–93, 2011.

[84] Y. F. Suprunenko and A. Stefanovska, "Generalized chronotaxic systems: Time-dependent oscillatory dynamics stable under continuous perturbation," *Phys Rev E*, vol. 90, no. 3, p. 032921, 2014.

[85] E. Y. Andrei, *Two-Dimensional Electron Systems on Helium and Other Cryogenic Substrates*. Kluwer Academics, Dordrecht, 1997.

[86] E. Collin, W. Bailey, P. Fozooni, P. Frayne, P. Glasson, K. Harrabi, and M. Lea, "Temperature-dependent energy levels of electrons on liquid helium," *Phys Rev B*, vol. 96, no. 23, p. 235427, 2017.

[87] A. Badrutdinov, D. Konstantinov, M. Watanabe, and K. Kono, "Experimental study of energy relaxation of hot electrons on liquid helium-4," *Europhys Lett*, vol. 104, no. 4, p. 47007, 2013.

[88] S. Strogatz, M. Friedman, A. J. Mallinckrodt, and S. McKay, "Nonlinear dynamics and chaos: With applications to physics, biology, chemistry, and engineering," *Comput. phys*, vol. 8, no. 5, pp. 532–532, 1994.

[89] A. Goldbeter, *Biochemical oscillations and cellular rhythms: the molecular bases of periodic and chaotic behaviour*. Cambridge university press, 1997.

[90] P. E. Kloeden and C. Pötzsche, "Nonautonomous dynamical systems in the life sciences," in *Nonautonomous Dynamical Systems in the Life Sciences*, pp. 3–39, Springer, 2013.

[91] C. Chatfield, *The Analysis of Time Series: an Introduction*. CRC Press, 2016.

[92] D. Gabor, "Theory of communication. part 1: The analysis of information,"

J Inst Electr Eng Pt III Radio Commun Eng, vol. 93, no. 26, pp. 429–441, 1946.

[93] L. W. Sheppard, A. Stefanovska, and P. V. E. McClintock, "Detecting the harmonics of oscillations with time-variable frequencies," *Phys Rev E*, vol. 83, no. 1, p. 016206, 2011.

[94] A. Bandrivskyy, A. Bernjak, P. V. E. McClintock, and A. Stefanovska, "Wavelet phase coherence analysis: application to skin temperature and blood flow," *Cardiovasc Eng int j*, vol. 4, no. 1, pp. 89–93, 2004.

[95] J. Jamšek, M. Paluš, and A. Stefanovska, "Detecting couplings between interacting oscillators with time-varying basic frequencies: Instantaneous wavelet bispectrum and information theoretic approach," *Phys Rev E*, vol. 81, no. 3, p. 036207, 2010.

[96] A. Duggento, T. Stankovski, P. V. E. McClintock, and A. Stefanovska, "Dynamical Bayesian inference of time-evolving interactions: From a pair of coupled oscillators to networks of oscillators," *Phys Rev E*, vol. 86, no. 6, p. 061126, 2012.

[97] L. M. Ward and P. E. Greenwood, "$1/f$ noise," *Scholarpedia*, vol. 2, no. 12, p. 1537, 2007.

[98] G. Kaiser, *A Friendly Guide to Wavelets*. Boston: Birkhäuser, 1994.

[99] N. Delprat, B. Escudié, P. Guillemain, R. Kronland-Martinet, P. Tchamitchian, and B. Torresani, "Asymptotic wavelet and Gabor analysis: Extraction of instantaneous frequencies," *IEEE Trans Inf Theory*, vol. 38, no. 2, pp. 644–664, 1992.

[100] G. Lancaster, D. Iatsenko, A. Pidde, V. Ticcinelli, and A. Stefanovska, "Surrogate data for hypothesis testing of physical systems," *Phys Rep*, vol. 748, pp. 1–60, 2018.

[101] C. Raeth and R. Monetti, "Surrogates with random Fourier phases," in *Topics on Chaotic Systems: Selected Papers from Chaos 2008 International Conference*, pp. 274–285, World Scientific, 2009.

[102] J.-P. Lachaux, A. Lutz, D. Rudrauf, D. Cosmelli, M. Le Van Quyen, J. Martinerie, and F. Varela, "Estimating the time-course of coherence between single-trial brain signals: an introduction to wavelet coherence," *Neurophysiol. Clin*, vol. 32, no. 3, pp. 157–174, 2002.

[103] M. Le Van Quyen, J. Foucher, J.-P. Lachaux, E. Rodriguez, A. Lutz, J. Martinerie, and F. J. Varela, "Comparison of Hilbert transform and wavelet methods for the analysis of neuronal synchrony," *J Neurosci Methods*, vol. 111, no. 2, pp. 83–98, 2001.

[104] A. Grinsted, J. C. Moore, and S. Jevrejeva, "Application of the cross wavelet transform and wavelet coherence to geophysical time series," *Nonlinear Process. Geophys*, vol. 11, no. 5/6, pp. 561–566, 2004.

[105] D. Kugiumtzis, "Surrogate data test on time series," in *Modelling and Forecasting Financial Data*, pp. 267–282, Springer, 2002.

[106] V. N. Smelyanskiy, D. G. Luchinsky, A. Stefanovska, and P. V. E. McClintock, "Inference of a nonlinear stochastic model of the cardiorespiratory interaction," *Phys Rev Lett*, vol. 94, no. 9, p. 098101, 2005.

[107] T. Stankovski, A. Duggento, P. V. E. McClintock, and A. Stefanovska, "Inference of time-evolving coupled dynamical systems in the presence of noise," *Phys Rev Lett*, vol. 109, no. 2, p. 024101, 2012.

[108] T. Stankovski, A. Duggento, P. V. E. McClintock, and A. Stefanovska, "A tutorial on time-evolving dynamical Bayesian inference," *Eur Phys J Spec Top*, vol. 223, no. 13, pp. 2685–2703, 2014.

[109] J. Newman, G. Lancaster, and A. Stefanovska, "Multiscale oscillatory dynamics analysis (MODA), user manual v1.01," 2018.

[110] S. A. Billings, *Nonlinear system identification: NARMAX methods in the time, frequency, and spatio-temporal domains*. John Wiley & Sons, 2013.

[111] E. Zhang, D. Shan, and Q. Li, "Nonlinear and non-stationary detection for measured dynamic signal from bridge structure based on adaptive decomposition and multiscale recurrence analysis," *Appl Sci*, vol. 9, no. 7, p. 1302, 2019.

[112] M. G. Rosenblum and A. S. Pikovsky, "Detecting direction of coupling in interacting oscillators," *Phys Rev E*, vol. 64, no. 4, p. 045202, 2001.

[113] M. Paluš and A. Stefanovska, "Direction of coupling from phases of interacting oscillators: An information-theoretic approach," *Phys Rev E*, vol. 67, no. 5, p. 055201, 2003.

[114] T. Schreiber and A. Schmitz, "Surrogate time series," *Physica D: Nonlinear Phenomena*, vol. 142, no. 3-4, pp. 346–382, 2000.

[115] A. Andronov, A. Vitt, and S. Khaikin, "Theory of oscillations, Pergamon Press, Oxford," 1966.

[116] Y. F. Suprunenko, P. T. Clemson, and A. Stefanovska, "Chronotaxic systems with separable amplitude and phase dynamics," *Phys Rev E*, vol. 89, no. 1, p. 012922, 2014.

[117] P. T. Clemson, Y. F. Suprunenko, T. Stankovski, and A. Stefanovska, "Inverse approach to chronotaxic systems for single-variable time series," *Phys Rev E*, vol. 89, no. 3, p. 032904, 2014.

[118] K. J. Friston, "Functional and effective connectivity: a review," *Brain Connect*, vol. 1, no. 1, pp. 13–36, 2011.

[119] D. Iatsenko, P. V. E. McClintock, and A. Stefanovska, "Linear and synchrosqueezed time-frequency representations revisited: Overview, standards

of use, resolution, reconstruction, concentration, and algorithms," *Digit Signal Process*, vol. 42, 04 2015.

[120] R. A. Carmona, W.-L. Hwang, and B. Torrésani, "Characterization of signals by the ridges of their wavelet transforms," *IEEE Trans Signal Process*, vol. 45, no. 10, pp. 2586–2590, 1997.

[121] C. Peng, S. V. Buldyrev, S. Havlin, M. Simons, H. E. Stanley, and A. L. Goldberger, "Mosaic organization of DNA nucleotides," *Phys Rev E*, vol. 49, no. 2, p. 1685, 1994.

[122] Y. Shiogai, A. Stefanovska, and P. V. E. McClintock, "Nonlinear dynamics of cardiovascular ageing," *Phys Rep*, vol. 488, no. 2-3, pp. 51–110, 2010.

[123] M. Keshner, "1/f noise," *Proceedings of the IEEE*, vol. 70, no. 3, pp. 212–218, 1982.

[124] S. Yamanaka, T. Arai, A. Sawada, A. Fukuda, and H. Yayama, "Oscillation mode transformation of edge magnetoplasmons in two-dimensional electron system on liquid-helium surface," *Low Temperature Physics*, vol. 39, no. 10, pp. 842–850, 2013.

[125] R. Williams and R. Crandall, "Deformation of the surface of liquid helium by electrons," *Phys Lett A*, vol. 36, no. 1, pp. 35–36, 1971.

[126] L. D. Landau and E. M. Lifshitz, *Course of Theoretical Physics, Vol. 6: Fluid Mechanics*. Oxford: Heinemann, 1987.

[127] V. Ganitkevich, V. Mattea, and K. Benndorf, "Glycolytic oscillations in single ischemic cardiomyocytes at near anoxia," *J Gen Physiol*, vol. 135, no. 4, pp. 307–319, 2010.